University of Zagreb
Faculty of Mechanical Engineering and Naval Architecture

MASTER'S THESIS

Luka Balatinec

Zagreb, 2019

University of Zagreb
Faculty of Mechanical Engineering and Naval Architecture

MASTER'S THESIS

An Overview of Rotor-Stator Interfaces for Computational Fluid Dynamics Simulations in Turbomachinery

Mentor:
prof. dr. sc. Hrvoje Jasak

Student:
Luka Balatinec

Zagreb, 2019

I would like to express my sincere gratitude to professor Jasak for the mentorship he provided, offering invaluable advice and sharing his immense knowledge and expertise.

Furthermore, I would like to wholeheartedly thank Tessa Uroić and Vanja Škurić for the guidance, support and friendship they so kindly offered.

I would also like to thank the rest of the 8^{th} floor CFD "crew" for making the time I spent there both interesting and fun.

Finally, I would like to thank my family, friends and my girlfriend for the support and understanding they provided.

Statement | Izjava

I hereby declare that I have made this thesis independently using the knowledge acquired during my studies and the cited references.

Izjavljujem da sam ovaj rad radio samostalno koristeći znanja stečena tijekom studija i navedenu literaturu.

Zagreb, March 2019 Luka Balatinec

SVEUČILIŠTE U ZAGREBU
FAKULTET STROJARSTVA I BRODOGRADNJE
Središnje povjerenstvo za završne i diplomske ispite
Povjerenstvo za diplomske ispite studija strojarstva za smjerove:
procesno-energetski, konstrukcijski, brodostrojarski i inženjersko modeliranje i računalne simulacije

Sveučilište u Zagrebu Fakultet strojarstva i brodogradnje	
Datum	Prilog
Klasa:	
Ur.broj:	

DIPLOMSKI ZADATAK

Student: **Luka Balatinec** Mat. br.: 0035190195

Naslov rada na hrvatskom jeziku: **Pregled metode povezivanja rotorske i statorske mreže u proračunskoj mehanici fluida za simulacije turbostrojeva**

Naslov rada na engleskom jeziku: **An Overview of Rotor-Stator Interfaces for Computational Fluid Dynamics Simulations in Turbomachinery**

Opis zadatka:

Computational geometry in turbomachinery applications of Computational Fluid Dynamics (CFD) features a number of repeated geometrical features, such as rotor and stator blade passages. Significant cost reduction can be achieved if the computational mesh spans only a section of repeating geometry rather than the complete device. Such an approach requires special forms of rotor stator interfaces, usually referred to as „frozen rotor General Grid Interface (GGI)", „cyclic GGI" with translational or rotational offset, „partial overlap GGI" for non-matching rotor/stator spans and the averaging „mixing plane" rotor-stator interface.

The objective of this study is to describe in detail the GGI, cyclic GGI, partial overlap GGI and mixing plane interface and examine their performance on a counter-rotating propeller case, with different levels of approximation.

The candidate shall perform the following tasks within this project:

- Describe in detail various forms of the rotor-stator interfaces used in turbomachinery CFD, with the assumptions they introduce on the geometry and case setup;
- Identify the experimental data for the counter-rotating propeller study. Prepare the computational mesh with the following levels of approximation:
  - Full geometry of both propellers, with full overlap
  - Single blade passage of the upstream and downstream propeller, with partial overlap and cyclic GGI interfaces
- Perform numerical simulation for the steady-state frozen rotor approach for both geometries. For single blade passage geometry, set up cases with different relative position of propeller blades;
- Perform a transient simulation for both geometries, using the segregated turbulent incompressible flow solver in OpenFOAM. Compare steady and transient results of simulations for consistency and validate against available experimental data;
- Extend the existing implementation of rotor-stator interfaces to the functionality of the block-coupled implicit p-U solver and compare the performance of steady-state simulations against the segregated solver results.

The Thesis shall list the bibliography and any assistance received during this study.

Zadatak zadan:	Rok predaje rada:	Predviđeni datumi obrane:
17. siječnja 2019.	21. ožujka 2019.	27., 28. i 29 ožujka 2019.

Zadatak zadao: Predsjednica Povjerenstva:

Prof. dr. sc. Hrvoje Jasak Prof. dr. sc. Tanja Jurčević Lulić

Contents

List of Figures

List of Tables

Nomenclature

Acronyms

BEP	Best efficiency point . . . 78
CCW	Counter-clockwise . . . 54
CFD	Computational Fluid Dynamics . . . 2
CRP	Contra-Rotating Propellers . . . 44
CV	Control Volume . . . 5
CW	Clockwise . . . 54
DFT	Direct Fourier Transform . . . 50
DNS	Direct Numerical Simulation . . . 21
FVM	Finite Volume Method . . . 4
GGI	General Grid Interface . . . 36
HVAC	Heating, Ventilation and Air Conditioning . . . 2
LES	Large Eddy Simulation . . . 21
MRF	Multiple Reference Frame . . . 27
RANS	Reynolds-Averaged Navier-Stokes Equations . . . 21
rps	Revolutions per second . . . 69
RTT	Reynolds Transport Theorem . . . 5
SRF	Single Reference Frame . . . 27
TKE	Turbulent kinetic energy . . . 74

Greek Symbols

α	[-]	Under-relaxation factor . . . 17
α_P	[-]	Pressure under-relaxation factor . . . 19

α_U	[-]	Velocity under-relaxation factor	19
Δ	[m]	Length-scale	22
ε	[m^2/s^3]	Turbulent dissipation	22
η_a	[-]	Aft propeller efficiency	50
η_f	[-]	Fore propeller efficiency	50
η	[-]	Total set efficiency	50
ϕ	[-]	General scalar property	5
γ	[-]	Diffusivity	7
ν	[m/s^2]	Kinematic viscosity	21
ν_{eff}	[m/s]	Effective kinematic viscosity	8
ν_t	[m/s^2]	Turbulent kinematic viscosity	22
ω	[1/s]	Specific dissipation rate	23
$\boldsymbol{\omega}$	[1/s]	Angular velocity	28
θ	[rad]	Phase angle	50
ρ	[kg/m^3]	Fluid density	8
ρ	[kg/m^3]	Water density	50
$\boldsymbol{\sigma}$	[N/m^2]	Cauchy stress tensor	8
$\overline{\mathbf{S}}$	[-]	second rank symmetric mean velocity gradient	21

Roman Symbols

$\mathbf{a}$	[-]	General vector property	6
$\mathbf{A}$	[-]	Square matrix	16
A	[-]	Dimensionless constant	22
a_N	[-]	Matrix coefficient corresponding to the neighbour N	16
a_P	[-]	Central coefficient	16
D_a	[m]	Aft propeller diameter	50
$\mathbf{d}_f$	[m]	Delta vector	10
D_f	[m]	Fore propeller diameter	50
e	[J/m^3]	Total specific energy	9
F	[-]	Face flux	13
F_b	[-]	Boundary flux	33
F_r	[-]	Relative flux	33
$\mathbf{g}$	[m/s^2]	Gravitational acceleration	8

$\mathbf{H}$	[-]	Transport part of matrix	18
J	[-]	Advance coefficient	50
k	[m^2/s^2]	Turbulent kinetic energy	22
K_{Qa}	[-]	Aft propeller torque coefficient	50
K_{Qf}	[-]	Fore propeller torque coefficient	50
K_{Ta}	[-]	Aft propeller thrust coefficient	50
K_{Tf}	[-]	Fore propeller thrust coefficient	50
$\widetilde{K}_{Qa,N}$	[-]	Aft unsteady torque coefficient	50
$\widetilde{K}_{Qf,N}$	[-]	Fore unsteady torque coefficient	50
$\widetilde{K}_{Q,prop,N}$	[-]	Unsteady torque coefficient of a single propeller	50
$\widetilde{K}_{Q,N}$	[-]	Total unsteady torque coefficient	50
$\widetilde{K}_{Ta,N}$	[-]	Aft unsteady thrust coefficient	50
$\widetilde{K}_{Tf,N}$	[-]	Fore unsteady thrust coefficient	50
$\widetilde{K}_{T,prop,N}$	[-]	Unsteady thrust coefficient of a single propeller	50
$\widetilde{K}_{T,N}$	[-]	Total unsteady thrust coefficient	50
$\mathbf{n}$	[-]	Surface normal vector	5
N	[-]	Nth harmonic	50
n	[s^{-1}]	Rotational speed	50
p	[Pa]	Pressure	16
$\mathbf{q}_s$	[-]	Surface source	6
$\mathbf{q}$	[W/m^2]	Specific heat flux	9
q_v	[-]	Volume source	6
Q	[N/m^3]	Volumetric heat source	9
$\mathbf{R}$	[m^2/s^2]	Reynolds stress tensor	21
$\mathbf{r}$	[-]	Right-hand side vector	17
$\mathbf{r}_P$	[m]	Centroid position vector	10
S	[-]	Complex variable	15
S_f	[m^2]	Face surface area	10
S_m	[m^2]	Surface area of V_m	5
$\mathbf{s}_f$	[m^2]	Surface normal vector	10
S_p	[-]	Constant part of the source term	15
S_u	[-]	Linear part of the source term	15

T_a	[N]	Aft propeller thrust	50
$T_{1,N}$	[N]	Cosine amplitude component of unsteady thrust	50
$T_{2,N}$	[N]	Sine amplitude component of unsteady thrust	50
T_f	[N]	Fore propeller thrust	50
Q_a	[Nm]	Aft propeller torque	50
$Q_{1,N}$	[Nm]	Cosine amplitude component of unsteady torque	50
$Q_{2,N}$	[Nm]	Sine amplitude component of unsteady torque	50
Q_f	[Nm]	Fore propeller torque	50
$\widetilde{Q}$	[Nm]	Unsteady torque	50
$\widetilde{T}$	[N]	Unsteady thrust	50
$\mathbf{u}$	[m/s]	velocity vector	5
$\mathbf{U}$	[m/s]	Velocity scale	22
U	[m/s]	Axial velocity	50
$\mathbf{u}_b$	[m/s]	Velocity of moving the boundary	33
U_i	[m/s]	Inlet velocity	72
$\mathbf{u}_r$	[m/s]	Relative velocity	33
U_x	[m/s]	Axial velocity	72
V	[m^3]	Material volume	6
V_m	[m^3]	Material volume	5
V_P	[m^3]	Volume of the cell	6
$\mathbf{x}$	[m]	Position vector	10

Superscripts

$'$	Fluctuation around the mean value	21
$\overline{}$	Mean value	21
^{n}	Value at new time-step	12
^{o}	Value at old time-step	12
^{oo}	Value at "second old" time-step	14
^{T}	Transpose	21
^{t}	Instance of time	11
**	New value	19
*	Initial value	19

Subscripts

b	Value at the boundary	33
f	Value at cell face	10
I	Inertial frame of reference	28
N	Value for neighbour cell	14
P	Value at cell centroid	10
R	Relative frame of reference	28
r	Value in the relative frame	33

Sažetak

Ubrzan napredak računalne dinamike fluida (RDF) omogućio je nadilaženje jednostavnih zadataka te prelazak na složenije probleme poput turbostrojeva. Zbog složenosti turbostrojeva, često se uvode pojednostavljenja geometrije s ciljem smanjenja vremena trajanja simulacije. Pojednostavljenja je također moguće provesti primjenom adekvatnih stacionarnih simulacija za modeliranje gibanja unutar domene. Kako bi se omogućila komunikacija između dijelova domene s različito definiranom rotacijom, nepovezanih ili djelomično povezanih dijelova domene te kružno ponavljajućih rubnih ploha, primjenjuju se različita sučelja. U sklopu ovog rada, izložena je teorijska pozadina pojedinih sučelja uz primjere primjene istih u računalnim simulacijama trubostrojeva s nestlačivim radnim fluidom. Simulacije su provedene u svrhu validacije različitih pristupa u korištenju sučelja za osnivanje komunikacije između rotora i statora. Izvršen je niz simulacija na primjeru para kontra-rotirajućih brodskih propelera navedenih u nastavku:

- Stacionarne simulacije s cjelovitom domenom propelera uz korištenje `ggi` sučelja.
- Stacionarne simulacije s četvrtinom domene propelera uz korištenje `cyclicGgi` i `overlapGgi` sučelja te istovjetne simulacije s različitim međusobnim položajem propelera.
- Stacionarne simulacije s četvrtinom domene propelera uz korištenje `cyclicGgi` i `mixingPlane` sučelja.
- Tranzijentne simulacije s četvrtinom domene propelera uz korištenje `cyclicGgi` i `overlapGgi` sučelja.

Provedena je analiza rezultata navedenih simulacija na temelju kojih su izračunati koeficijenti hidrodinamičkih performansi seta propelera. Pokazana je dobra usuglašenost rezultata simulacija s cjelovitom domenom te onih iz simulacije s četvrtinom domene. Usporedba rezultata stacionarnih simulacija pokazuje dobru usuglašenost s eksperimentalnim podacima za područja više efikasnosti propelera, dok je za radne točke u područjima niže efikasnosti potrebno provesti tranzijentne simulacije.

Ključne riječi: RDF, rotorska i statorska sučelja, kontra-rotirajući propeleri, `ggi`, `overlapGgi`, `cyclicGgi`, `mixingPlane`, `foam-extend`

Abstract

Rapid progress of Computational Fluid Dynamics (CFD) allowed CFD to move past simple tasks and become a viable tool for the analysis of complex problems, such as turbomachines. Nevertheless, due to the complexity of turbomachinery, some simplifications regarding interface and domain handling are sought in order to allow for reasonable simulation execution times. Most often, only a part of the whole turbomachine geometry is simulated, which decreases computational demands. To enable communication between domain regions wherein different rotation (or other movement) is modelled, between ill-connected or overlapping regions, or between cyclic patches bounding partial geometry domains, various interfaces are used. Moreover, steady-state "frozen rotor" methods are frequently used to approximate transient problems but avoid computationally demanding transient simulations. This Thesis offers an overview of several rotor-stator interfaces available in `foam-extend`, with both theoretical background and numerical simulations. A series of numerical simulations is performed on a Contra-Rotating Propeller set (CRP), investigating different rotor-stator interface handling methods:

- Steady-state simulations using the Multiple Reference Frame (MRF) approach and the whole CRP geometry with General Grid Interface (`ggi`).
- Steady-state MRF simulations of a quarter CRP geometry using `overlapGgi` and `cyclicGgi` interfaces across periodic boundaries. Additional simulations are performed to investigate the effects of initial propeller position.
- Quarter CRP geometry steady-state MRF simulations using `cyclicGgi` and `mixingPlane` interfaces.
- Transient simulation of a quarter CRP geometry with the `cyclicGgi` and `overlapGgi` interfaces.

The results were analysed in terms of hydrodynamic performance coefficients, showing good agreement between quarter and full CRP simulations and validating the interfaces used. Comparison to experimental data revealed good agreement with steady-state results for high-efficiency conditions and good agreement with transient simulations for lower-efficiency conditions.

Keywords: CFD, rotor-stator interfaces, Contra-rotating propellers, `ggi`, `overlapGgi`, `cyclicGgi`, `mixingPlane`, `foam-extend`

Prošireni sažetak

Turbostrojevi predstavljaju skupinu složenih strojeva koje je moguće klasificirati u velik broj različitih kategorija uzimajući u obzir značajke određene njihovom konstrukcijom te strujanjem fluida kroz radni volumen stroja. Primjena računalne dinamike fluida za proučavanje strujanja fluida u radu turbostrojeva otvara nove spoznaje rada, konstrukcije i poboljšanja turbostrojeva. Istovremeno, kompleksna konstrukcija turbostrojeva zahtijeva korištenje određenih pojednostavljenja prilikom postavljanja računalnih simulacija. Ta se pojednostavljenja najčešće svode na različite pristupe modeliranja gibanja (rotacije) u domeni (računalnoj mreži) te povezanosti dijelova domene. U slučaju kada je numerička mreža stacionarna, a samo dio mreže rotira, relativni položaja između stacionarnog i rotirajućeg dijela mreže varira između vremenskih koraka simulacije. Kako bi se proveo RDF proračun, mrežu je potrebno povezati u jednu domenu. S obzirom na to da jedan dio mreže rotira, dok je drugi stacionaran, računalna mreža ne može biti izvedena cjelovito, već se sastoji od dvije povezane domene. Povezanost dijelova domene ostvaruje se korištenjem različitih sučelja koja ostvaruju komunikaciju između mirujućih i rotirajućih dijelova domene.

Kontra-rotirajući propeleri predstavljaju primjer turbostroja bez kućišta, koji zahtijevaju modeliranje dvije rotacijske zone unutar jedne proračunske domene. Upravo su iz tog razloga ovi propeleri izvrstan odabir za pregled metoda povezivanja rotirajućih i stacionarnih dijelova računalne mreže.

Metode povezivanja mreže

Kako bi se ostvarila adekvatna komunikacija između odvojenih dijelova mreže potrebno je korištenje nekog od niza sučelja za povezivanje mreže rotora i statora. Budući da se dijelovi mreže u kojima se modelira rotacija izvode kao zasebne zone odvojene plohama koje pripadaju unutrašnjosti numeričke mreže, komunikacija između takvih domena i ostaka mreže ostvaruje se sučeljima koja omogućuju komunikaciju između rubnih ploha unatoč nepodudaranju mrežnih čvorova na plohama. Također, numerička se mreža može pojednostaviti korištenjem samo jednog dijela domene koji se periodički ponavlja. Na rubnim plohama takve domene koriste moraju se koristiti posebna sučelja kako bi se ostvarila komunikacija.

Osnovna sučelja koja su korištena prilikom izrade ovog rada te se mogu pronaći unutar paketa `foam-extend` nabrojana su u nastavku:

- `ggi` (eng. *General grid interface*) - Osnovno sučelje koje se koristi za povezivanje dijelova domene čije se granice ne poklapaju, a komunikaciju ostvaruje interpoliranjem varijabli između granica domena. Primjena `ggi` sučelja pretpostavlja potpuno preklapanje ploha s obje strane sučelja.

- `overlapGgi`- Izvedenica osnovnog `ggi` sučelja koja se koristi za povezivanje graničnih ploha kod kojih je ostvareno samo djelomično preklapanje.

- `cyclicGgi`- Izvedenica `ggi` sučelja kod koje se poklapanje ploha ostvaruje translacijskom ili rotacijskom transformacijom koordinata, a koristi se na granicama dijela domene koji se periodički ponavlja kako bi se ostvarila komunikacija s drugim, cjelovitim ili djelomičnim, dijelovima domene.

- `mixingPlane`- Sučelje koje omogućava komunikaciju između granica s djelomičnim preklapanjem, slično kao i `overlapGgi`, uz uvođenje dodatnog osrednjavanja vrijednosti koje se prenose između granica.

Primjena navedenih sučelja, kao i njihov utjecaj na konačne rezultate, ispitani su nizom simulacija provedenim unutar ovog rada te opisanim u nastavku.

Kontra-rotirajući propeleri

Ovakav se tip brodskog pogona sastoji od para propelera sa zajedničkom osi vrtnje, koji rotiraju u suprotnim smjerovima te se nalaze na istom ili dva odvojena vratila. Njihovom se primjenom ostvaruju prednosti u odnosu na korištenje samo jednog propelera, kao što su: bolja razdioba opterećenja između propelera, povećanje efikasnosti pogona, smanjenje mogućnosti pojave kavitacije, produžen životni vijek pojedinog propelera, itd. Jedna od osnovnih prednosti kod primjene kontra-rotirajućih propelera je smanjenje momenta koji izaziva zakretanje (izboj) broda. Primjena seta propelera s jednakim i parnim brojem lopatica izaziva pojavu fluktuacije potiska. S druge strane, koristi li se set s neparnim brojem lopatica, fluktuacija potiska će biti manja, ali dolazi do pojave bočnih sila.

Iako je ovaj tip brodskih propelera odavno poznat u brodogradnji, prve su izvedbe ovih propelera koristile jedno vratilo (Slika 1), što je dovodilo do velikih problema s trenjem između unutarnjeg i vanjskog dijela vratila. Upravo je zbog tog razloga daljnji razvoj kontra-rotirajućih propelera zaustavljen. Do ponovnog jačanja interesa za ovakvim propelerima dolazi tek naglim razvojem elektromagnetskih motora te pojave moderne inačice ovog sustava. Kod modernih izvedbi jedan se propeler nalazi na vratilu glavnog pogonskog stroja broda, a drugi je pogonjen elektromotorom u pomičnoj gondoli iz glavnog propelera (Slika 2).

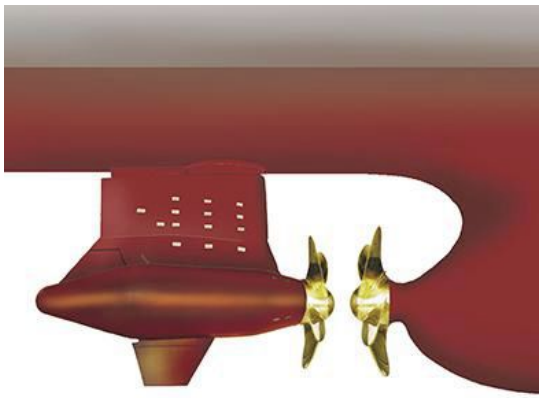

Slika 1: Izvedba s gondolom [1].

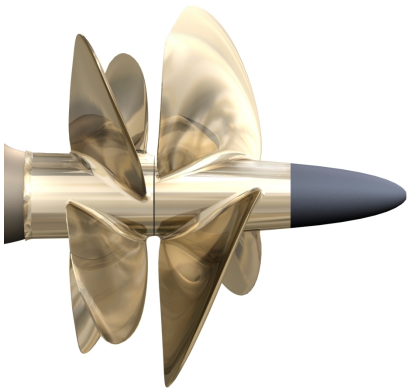

Slika 2: Izvedba s jednim vratilom [2].

Hidrodinamičke karakteristike propelera

Rad propelera može se kvantificirati pomoću hidrodinamičkih karakteristika na temelju kojih se formira dijagram slobodne vožnje brodskih propelera. Dijagram se temelji na koeficijentima poriva i momenta te efikasnosti propelera koji se računaju za radne točke definirane koeficijentom napredovanja J:

$$J = \frac{U}{n\,D_f}.$$

Pomoću vrijednosti J izračunate temeljem promjera prednjeg propelera (D_f), moguće je izračunati vrijednosti koeficijenta poriva, momenta te efikasnosti za prednji i stražnji propeler:

$$K_{Tf} = \frac{T_f}{n^2 D_f^4 \rho}, \qquad K_{Qf} = \frac{Q_f}{n^2 D_f^5 \rho},$$
$$K_{Ta} = \frac{T_a}{n^2 D_a^4 \rho}, \qquad K_{Qa} = \frac{Q_a}{n^2 D_a^5 \rho},$$
$$\eta_f = \frac{K_{Tf}}{K_{Qf}} \frac{J}{2\pi}, \qquad \eta_a = \frac{K_{Ta}}{K_{Qa}} \frac{J}{2\pi}.$$

Ukupne se vrijednosti koeficijenata potiska i momenta dobivaju zbrajanjem vrijednosti za pojedinačne propelere, dok se ukupna efikasnost računa prema izrazu:

$$\eta = \frac{K_T}{K_Q} \frac{J}{2\pi}.$$

Konačne se vrijednosti navedenih koeficijenta i efikasnosti unose u dijagram u ovisnosti o koeficijentu napredovanja, što se naziva dijagramom slobodne vožnje propelera.

Numerička mreža

Numerička mreža izrađena je na temelju modela kontra-rotirajućih propelera koji je opisan u tablici (Tablica 1). Model sa sastoji od dva propelera s jednakim brojem lopatica koji rotiraju sinkronizirano brzinom od 12 okretaja u sekundi oko iste osi rotacije.

Korištene su dvije numeričke mreže, od koji je jedna temeljna na punoj geometriji (Slika 3, lijevo) propelera, dok se druga temelji na četvrtini geometrije (Slika 3, desno). Obje se numeričke mreže sastoje od tri regije (odvojne domene) povezane adekvatnim sučeljima. Uz svaki je propeler definirana zona rotacije, koje su okružene stacionarnom mrežom koja predstavlja područje neporemećenog strujanja fluida.

Tablica 1: Karakteristike propelera.

Propeller type	**3686**	**3687A**
Position in set	FORE	AFT
Blades	4	4
Diameter [m]	0.2991	0.3052
Rotation	CW	CCW
Expanded area ratio	0.303	0.324
Section Meanline	NACA $a = 0.8$	NACA $a = 0.8$
Thickness Distribution	NACA 66	NACA 66

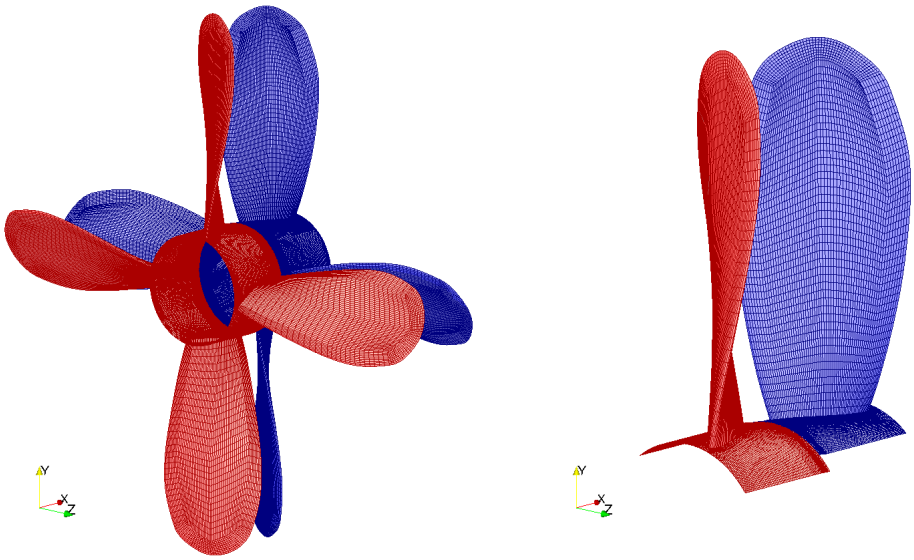

Slika 3: Puna geometrija (lijevo) i četvrtina geometrije propelera (desno).

U numeričkoj mreži cjelovite geometrije, komunikacija između domena propelera i ostatka mreže ostvarena je pomoću `ggi` sučelja. Mreža djelomične geometrije zahtijeva korištenje `cyclicGgi` sučelja za ostvarivanje komunikacije na periodičkim granicama te `overlapGgi` za povezivanje domena četvrtina propelera s ostatkom mreže. Za testiranje `mixingPlane` sučelja, korištena je mreža temeljena na četvrtini propelera s `cyclicGgi` sučeljem te `mixingPlane` sučeljem na granici domena četvrtina propelera i ostatka mreže.

Rezultati simulacija

Za potrebe rada proveden je niz simulacija koristeći prethodno predstavljene numeričke mreže kontra-rotirajućih brodskih propelera:

- Stacionarne simulacije s cjelovitom domenom propelera uz korištenje `ggi` sučelja.
- Stacionarne simulacije s četvrtinom domene propelera uz korištenje `cyclicGgi` i `overlapGgi` sučelja te istovjetne simulacije s različitim međusobnim položajem propelera.
- Stacionarne simulacije s četvrtinom domene propelera uz korištenje `cyclicGgi` i `mixingPlane` sučelja.
- Tranzijentne simulacije s četvrtinom domene propelera uz korištenje `cyclicGgi` i `overlapGgi` sučelja.

Rezultati svake simulacije analizirani su grafičkim prikazom relevantnih polja, te su izračunati koeficijenti hidrodinamičkih značajki svakog od propelera i cijelog seta. Na temelju rezultata formirani su dijagrami slobodne vožnje propelera.

Simulacija pune geometrije

Rezultati izračunati na temelju stacionarne simulacije pune geometrije prikazani su u dijagramu slobodne vožnje na slici (Slika 4). Vrijednosti dobivene u numeričkoj simulaciji uspoređene su s dostupnim eksperimentalnim podacima. Vidljivo je odlično slaganje eksperimentalnih podataka i dobivenih rezultata, za više vrijednosti koeficijenta napredovanja J što odgovara području veće efikasnosti propelera. Za niže vrijednosti J, tj. za područje niže efikasnosti gdje je izražen utjecaj tranzijentnih pojava, mogu se uočiti odstupanja od eksperimentalnih podataka. Ona su objašnjena činjenicom da stacionarna simulacija ne uspijeva uhvatiti nestacionarne pojave čiji je utjecaj vrlo izražen za područja niskog koeficijenta J.

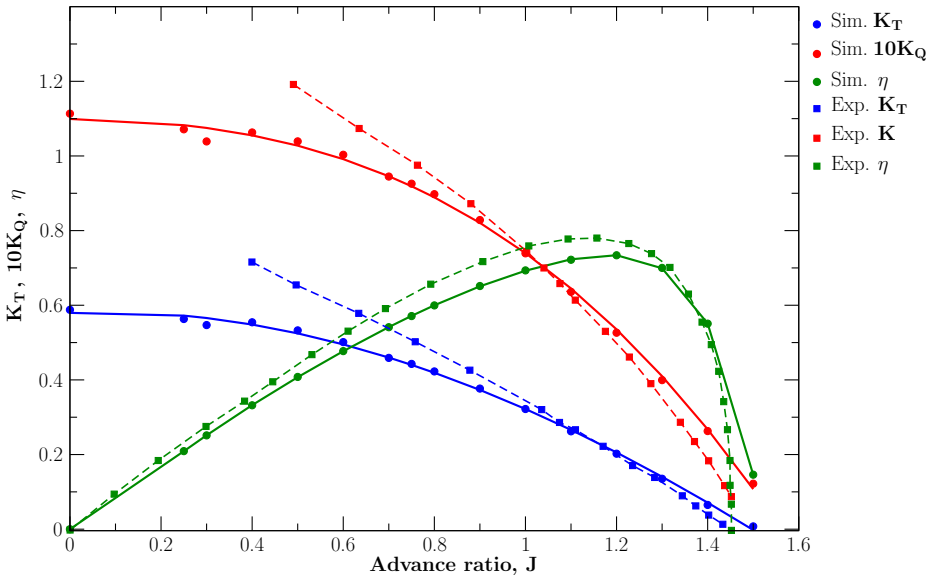

Slika 4: Dijagram slobodne vožnje simulacije čitavog propelera.

Simulacija četvrtine geometrije

Rezultati simulacija provedenih s četvrtinom geometrije uspoređeni su s rezultatima cjelovite geometrije, kako bi se validirala upotreba `cyclicGgi` i `overlapGgi` sučelja. Na slici (Slika 5) vidljivo je vrlo dobro poklapanje rezultata dviju navedenih geometrija, čime je opravdano daljnje korištenje mreže temeljene na četvrtini propelera. Ta mreža sadrži manji broj kontrolnih volumena što smanjuje vrijeme potrebno za postizanje zadane razine konvergencije.

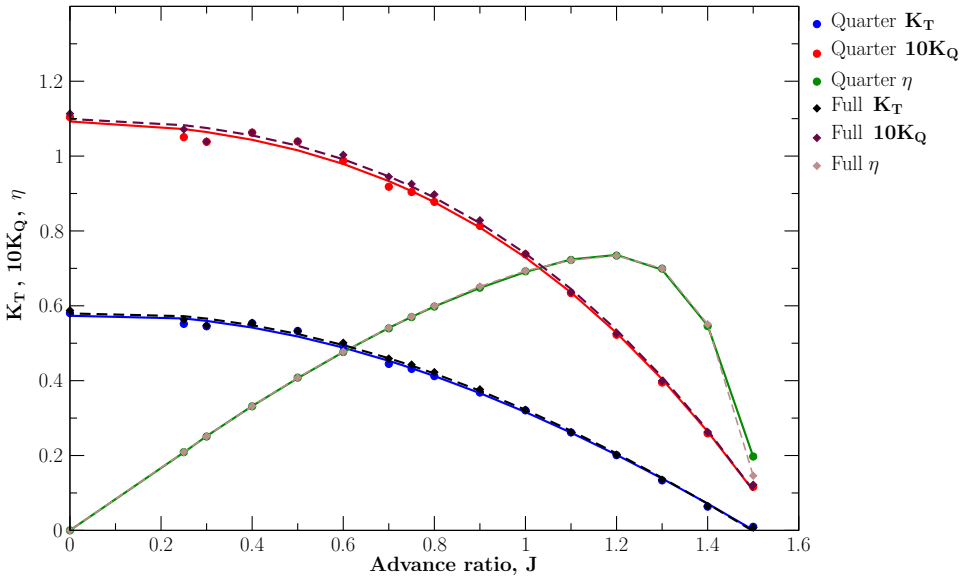

Slika 5: Dijagram slobodne vožnje simulacije četvrtine propelera.

`mixingPlane` simulacija

Primjena `mixingPlane` sučelja ispitana je korištenjem mreže četvrtine geometrije uz primjenu `cyclicGgi` sučelja. Rezultati prikazani na slici (Slika 6) pokazuju bolje podudaranje simulacije s eksperimentalnim podatcima za niža područja koeficijenta J. Također, korištenjem `mixingPlane` sučelja uvedeno je osrednjavanje vrijednosti na granici. Upravo iz toga razloga ovo sučelje nije smisleno primijeniti u tranzijentnim simulacijama.

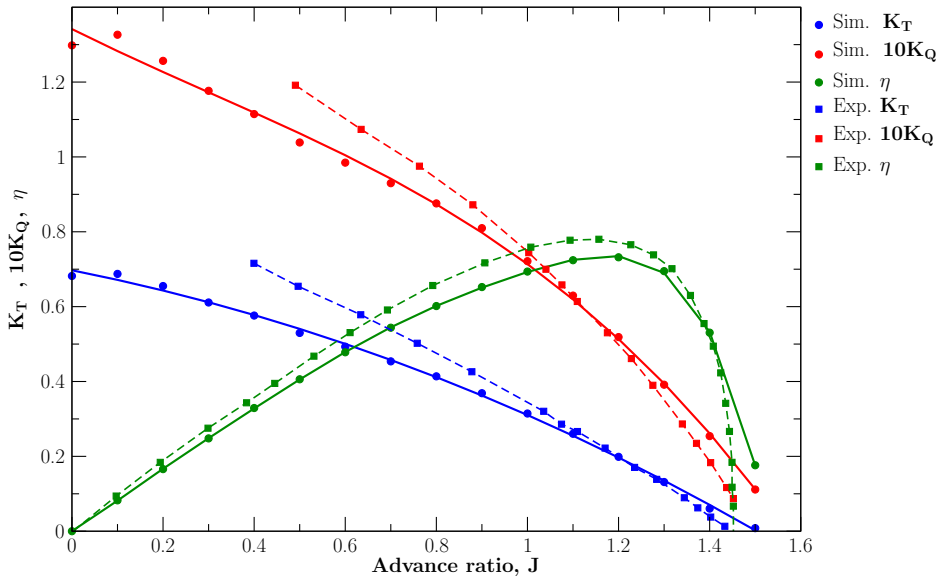

Slika 6: Dijagram slobodne vožnje simulacije uz `mixingPlane sučelje`.

Tranzijentna simulacija

Zbog dugog perioda trajanja simulacija potrebnog za postizanje periodičke stacionarnosti, izvršena je tranzijenta simulacija za samo jednu radnu točku u području nižih vrijednosti koeficijenta J. Cilj je provjeriti može li se tranzijentnom simulacijom postići rezultat koji odgovara eksperimentu, a kojeg nije bilo moguće postići stacionarnom simulacijom. Dobiveni su rezultati pokazali da je moguće postići vrlo dobro poklapanje s eksperimentom, ako je simulacija dostigla stanje periodičke stacionarnosti (Tablica 6.6).

Utjecaj početnog položaja propelera

Posljednji niz simulacija proveden je na četvrtini geometrije te koristeći `cyclicGgi` i `overlapGgi` sučelja. U simulacijama je variran početni položaj prednjeg propelera u odnosu na stražnji, te je promatran utjecaj na rezultate stacionarne simulacije (Tablica 6.4). Utvrđeno je kako različiti kutevi zakrenutosti između propelera znatno utječu na konačan rezultat, što je pripisano prirodnim varijacijama u iznosu sile i momenta tijekom rotacija propelera, vidljivim iz rezultata tranzijentne simulacije.

Zaključak

Na temelju simulacija provedenih prilikom izrade ovog rada, istražena su pojednostavljenja geometrije te pristupi modeliranju rotacije koje je moguće koristiti u računalnim simulacijama turbostrojeva. Većina metoda korištenih za modeliranje rotacije, kao i simuliranje dijela geometrije, zahtjeva korištenje sučelja, a čiji odabir ovisi o promatranim pojavama.

Za računalne simulacije turbostrojeva poput kontra-rotirajućih propelera, moguće je koristiti samo dio geometrije uz periodične rubne uvjete. Korištenjem dijela geometrije nisu uočena značajna odstupanja u odnosu na primjenu čitavog modela. Također, za simulacije radnih točaka blizu projektne radne točke, tj. radne točke u području visoke efikasnosti, stacionarne simulacije daju zadovoljavajuće rezultate. Ako je potrebno simulirati točke za područja niže efikasnosti, potrebno je koristiti tranzijentne simulacije.

1 Introduction

In general, the term *turbomachinery* describes a series of different machines operating on the principle of exchanging energy with a fluid which is continuously flowing around rotating and/or stationary elements of the machine. The presented definition of turbomachinery includes a wide range of machines operating on the same principle, yet involving different functions, operating environments and characteristics. Thus, a general classification of turbomachines is presented.

The simplest categorisation of turbomachines would be according to type of flow through the machine. Turbomachines are grouped into three categories depending on the direction of flow in regards to rotational axis of the machine: radial, axial and mixed flow machines [3]. The fluid flow in radial machines is perpendicular to the rotational axis, while fluids in axial machines flow parallel to the axis of rotation. Machines with mixed flow, represent a category of turbomachinery where the flow does not show dominantly axial or dominantly radial nature, having both radial and axial components of velocity instead. The difference between radial and axial flow machines is made evident by the mechanism of energy transfer between the machine and the fluid, that is, by the change in the velocity entering and exiting the rotor. While radial machines transfer energy by changes in the velocity angle and changes in radius, radial flow machines usually transfer work solely by changes in the velocity angle [4].

Further classification can be performed by examining the streamlines around the rotor. If the rotor of the machine is enclosed in a casing or shrouded in such a way that the streamlines cannot diverge to flow around the side of the rotor, the turbomachine can be considered a closed-type or enclosed machine (e.g. centrifugal pumps, turbopumps,

compressors). If streamlines are allowed to diverge around an unshrouded rotor, i.e. the machine operates without a stationary shroud, it can be considered an open-type or extended turbomachine (e.g. ship propellers or wind turbines) [3].

Closed-type turbomachines are usually sub-categorized depending on the type of fluid used. Hydraulic machines, such as centrifugal pumps or fans, work with fluids which can be considered incompressible for normal operating conditions. On the other hand, in thermal machines, such as steam and gas turbines or jet engines, work with compressible fluids.

If the energy exchange between the turbomachine and the working fluid is considered, turbomachines can be categorised as machines that use energy to increase the pressure of the working fluid (e.g. fans, pumps, compressors) or those that expand the fluid to generate energy (turbines).

The large number of turbomachines covered by the classification above are used for different applications in multiple industries. Turbomachines had an important part in energy generation, transportation and manufacturing since the Industrial revolution and continue to do so today, proving that further study of such devices and connected phenomena continues to have a vital role in modern science.

1.1. CFD in Turbomachinery

With various industries shifting towards greater fuel efficiency, cost reduction and lower emissions, new requirements are imposed on the construction and operation of turbomachinery. Older plants, vehicle and processes using turbomachines are also being retrofitted for greater efficiency and lower emissions. The need for improvement over the existing design and modelling processes calls for a modern approach to the prediction and verification of turbomachinery designs, such as Computational Fluid Dynamics.

Computational Fluid Dynamics (CFD) is a branch of fluid dynamics which uses numerical analysis to investigate fluid flow in various circumstances. The use of CFD for standard external aerodynamics such as heating, ventilation and air conditioning (HVAC) simulations and simple wall-bounded turbulent flows has been standard practice for years [5]. On the other hand, using CFD in turbomachinery brings far greater challenges concerning the geometry used, mesh resolution, simulation of rotating components, etc.

Complex geometry of most turbomachines supersedes simple geometries of most CFD simulations. Large numbers of rotating and stationary parts found in turbomachines further complicate the transient flows which are to be modelled. Interactions between rotating and stationary elements of such machines bring forth the occurrence of complex phenomena not usually found in external flow. Furthermore, turbulent boundary layers and wake-to-rotor interactions become of great importance in the CFD study of turbomachinery which, combined with complex multi-part geometry, demands very fine resolution of the computational mesh. This makes the simulations more demanding in terms of computational effort and CPU time. To deal with rotational effects of flow in single or multi-rotor turbomachines, relative motion needs to be taken into account. This is usually achieved either by introducing non-inertial rotational frames of reference or by topological changes of the computational mesh [5].

Taking into account the complex geometries and consequent phenomena connected with turbomachinery, the difficulties of CFD simulations of turbomachines become apparent. Complex flows, occurrence of transients, geometry optimisation, both design and off-design conditions are to be investigated and taken into account. Furthermore, the simulations need to produce quasi-stationary data applicable for machine design purposes and need to be acceptable in respect to both turnaround time and computational demands.

The need to deal with such high demands brought about the idea of simplifying the computational mesh by using only part of the whole geometry and introducing cyclic boundary conditions. To make such simplification possible, the problem of connecting different regions or geometries (e.g. rotor, stator) of the computational mesh was addressed by introducing various interfaces as means of enabling communication between disjoint or partially connected sections.

A good example of an extended turbomachine with complex rotor interaction is a set of Contra-Rotating Propellers (CRP). A CRP set consists of two unshrouded coaxial rotors, rotating in opposite directions. Having an increasingly important role in maritime propulsion, the CRP set presents an ideal choice of turbomachiery to be used for study of various interfaces in available turbomachinery CFD.

1.2. Scope of Thesis

This Thesis investigates different mesh-to-mesh interfaces used to connect stationary and rotational mesh components in turbomachinery CFD simulations. The theoretical background needed to understand the basic principles of the Finite Volume Method (FVM) and different approaches to domain and interface modelling is covered. Different approaches to turbomachinery simulation are presented on a CRP set, with an analysis of results gathered from both transient and steady-state simulations run in `foam-extend`.

1.3. Thesis Outline

This thesis is organised in seven Chapters, as follows: Chapter 1 offers an overview of turbomachinery and serves as an introduction to the Thesis. Chapter 2 introduces the basic notions of FVM used for CFD simulations. Chapter 3 gives a detailed overview of different approaches to interface and domain handling. Chapter 4 introduces the concept of CRP with details on the characteristics of CRP sets and offering an overview of related studies. Chapter 5 defines the different geometries used, listing the corresponding boundary conditions. Chapter 6 presents the results of CFD simulations both graphically and numerically, offering appropriate comments and explanations where needed. Chapter 7 serves as the Conclusion of the Thesis, followed by an Appendix offering examples of interface-setup in `foam-extend`.

2 Finite Volume Method

2.1. Introduction

The previous chapter served as a short introduction describing the intricacies of turbomachinery and the use of CFD to analyse the characteristics and performance of turbomachines. The following chapter shall introduce the Finite Volume Method and overview some of the theoretical background required to understand the implementation of the method in turbomachinery CFD.

2.2. The Scalar Transport Equation

If the Reynolds Transport Theorem (RTT) is applied to a region of space which is of interest when analysing a certain problem, it can be used to describe the rate of change of a general property ϕ in region (control volume, CV). The CV represents a closed system where the rate of change of the general property ϕ is equal to the sum of the change of property inside of the CV and the net rate of outflow through the surfaces defining the CV. The RTT for a CV like the one shown in Fig. 2.1, can be written as follows [6]:

$$\frac{d}{dt}\int_{V_m} \phi \, dV = \int_{V_m} \frac{\partial \phi}{\partial t} \, dV + \oint_{S_m} \phi(\mathbf{n}\bullet\mathbf{u}) dS \,. \tag{2.1}$$

Next, the general form of the Gauss' Theorem must be introduced to transform the surface integral from Eq. 2.1:

$$\int_{V_P} \nabla \cdot \mathbf{a}\, dV = \oint_{\partial V_P} d\mathbf{s}\bullet\mathbf{a} = \oint_{\partial V_P} d\mathbf{n}\bullet\mathbf{a}\, dS\,. \tag{2.2}$$

By applying Eq. 2.2 to Eq. 2.1, a volume integral form of the RTT is shown:

$$\frac{d}{dt}\int_V \phi\, dV = \int_V \left[\frac{\partial \phi}{\partial t} + \nabla \cdot (\phi \mathbf{u})\right] dV\,, \tag{2.3}$$

which is used to model the convective transport of a general property ϕ facilitated by the convective velocity $\mathbf{u}$. The inflow of the general property ϕ is given by $(\mathbf{u} \cdot \mathbf{n}) < 0$ and the outflow by $(\mathbf{u} \cdot \mathbf{n}) > 0$.

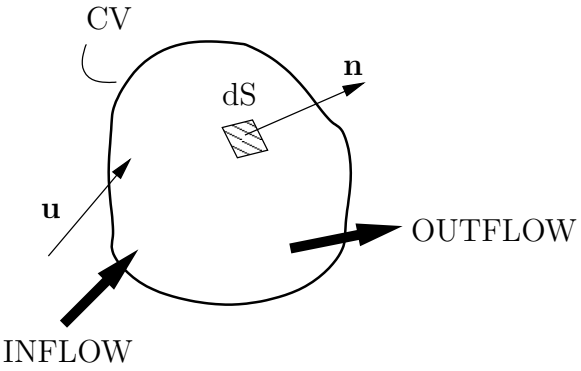

Figure 2.1: Closed system or Control Volume (CV).

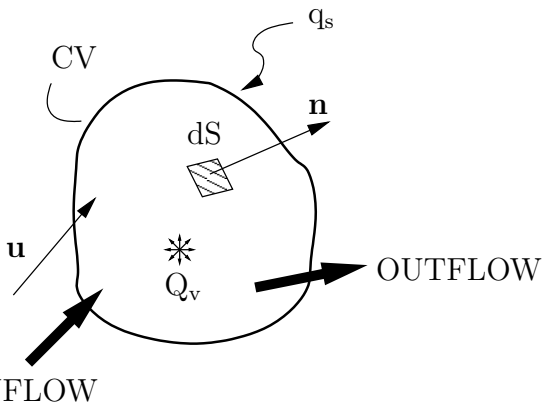

Figure 2.2: Surface and Volume sources of a CV.

As well as the convective transport, surface and volume sources also add to the change of a general property inside the CV. The contribution of surface and volume sources, shown in Fig. 2.2, is represented by:

$$\frac{d}{dt}\int_V \phi\, dV = \int_V q_v\, dV - \oint_S (\mathbf{n}\bullet\mathbf{q}_s) dS\,. \tag{2.4}$$

By applying the Gauss' Theorem to the source term in Eq. 2.4, matching the left-hand side of the resulting equation with Eq. 2.3 and integrating over the volume of the CV ($V = const.$), the following equation is obtained:

$$\frac{\partial \phi}{\partial t} + \nabla \cdot (\phi \mathbf{u}) = q_v - \nabla \cdot \mathbf{q}_s \,. \tag{2.5}$$

The terms representing surface sources, which act on the surface S of the CV, are modelled using Diffusive Transport. In physical terms, a general property ϕ in a closed domain (CV) will be transported from regions of greater concentration to regions of lower concentration until uniformity of concentration is achieved. The diffusion model is based on the fact that $\nabla\phi$ points in the direction of greater concentration of the property ϕ and the fact that the diffusive transport occurs in the opposite direction governed by the diffusivity γ [6]:

$$\mathbf{q}_s = -\gamma \, \nabla \phi \,. \tag{2.6}$$

By inserting Eq. 2.6 into Eq. 2.5 and rearranging, the general form of the Scalar Transport Equation may be presented:

$$\underbrace{\frac{\partial \phi}{\partial t}}_{\text{temporal derivative}} + \underbrace{\nabla \cdot (\phi \mathbf{u})}_{\text{convection term}} - \underbrace{\nabla \cdot (\gamma \nabla \phi)}_{\text{diffusion term}} = \underbrace{q_v}_{\text{source term}} \,. \tag{2.7}$$

The temporal derivative from Eq. 2.7 represents the inertia of the system, i.e. the ability of the system (CV) to accumulate a general property. The convection term represents a coordinate transform of the property, i.e. the amount of property ϕ transported into or out of the system, by the velocity $\mathbf{u}$. The diffusion term represents the gradient transport of property ϕ, defining the amount of ϕ transported by diffusive transport. Finally, source (or sink) terms define local production and/or destruction of the general property ϕ.

2.2.1. Governing Equations

The Scalar Transport Equation 2.7 represents one of the constitutional equations of Continuum Mechanics. It is the core equation describing how a scalar quantity is transported in a defined space. By replacing the general property ϕ with different properties, other governing equations of Continuum Mechanics can be derived:

Conservation of Mass

By substituting the general property ϕ in the Scalar Transport Equation 2.7 with fluid density denoted by ρ and defining a zero value source term, the equation describing the Conservation of Mass is derived:

$$\frac{\partial \rho}{\partial t} + \nabla \cdot (\rho \mathbf{u}) = 0\,. \tag{2.8}$$

For incompressible flow, the density of the fluid can be defined as constant $\rho = const.$, further simplifying Eq. 2.8:

$$\nabla \cdot \mathbf{u} = 0\,. \tag{2.9}$$

The form of the Conservation of Mass equation presented above (Eq. 2.9) is called the continuity Equation.

Conservation of Linear Momentum

The equation describing the Conservation of Linear Momentum can be derived from Eq. 2.7 by replacing the general variable ϕ with the linear momentum vector $\boldsymbol{\rho}\mathbf{u}$:

$$\frac{\partial(\rho \mathbf{u})}{\partial t} + \nabla \cdot (\rho \mathbf{u}\mathbf{u}) = \underbrace{\rho \mathbf{g}}_{\text{gravitational force}} + \underbrace{\nabla \cdot \boldsymbol{\sigma}}_{\text{surface forces}}\,. \tag{2.10}$$

For incompressible flow and usually ignoring gravitational forces for turbomachinery CFD, Eq. 2.10 can be transformed as follows:

$$\underbrace{\frac{\partial \mathbf{u}}{\partial t}}_{\text{local production}} + \underbrace{\nabla \cdot (\mathbf{u}\mathbf{u})}_{\text{convection}} - \underbrace{\nabla \cdot (\nu_{\text{eff}} \nabla \mathbf{u})}_{\text{diffusion}} = - \underbrace{\nabla \frac{p}{\rho}}_{\text{pressure gradinet}}\,, \tag{2.11}$$

where the Cauchy stress tensor is given as the sum of the pressure gradient ∇p and viscous stress tensor represented in the diffusion term. It should be noted that the fluid velocity $\mathbf{u}$ occurs in Eq. 2.11 both as the transporting and the transported variable, making the convection term non-linear [6].

An alternative from of the momentum equation can be defined using the definition of the total (material) derivative $\frac{D\phi}{Dt} = \frac{\partial\phi}{\partial t} + \nabla \cdot \mathbf{u}\,\phi$ with $\mathbf{u}$ as the variable ϕ:

$$\frac{D\mathbf{u}}{Dt} = \nabla \cdot (\nu_{\text{eff}} \nabla \mathbf{u}) - \nabla \frac{p}{\rho}\,. \tag{2.12}$$

The momentum equation presented in Eq. 2.12 is usually coupled with the continuity equation shown in Eq. 2.9 to form the Navier-Stokes set of equations for incompressible fluid flow.

Conservation of Energy

If the general property ϕ in Eq. 2.7 is replaced by specific internal energy ρe and the source/sink terms made equal to the sum of the power of different forces exerted on the CV and the net heat flux defined by specific heat flux $\mathbf{q}$ and volumetric heat source Q, the equation describing the Conservation of energy can be presented:

$$\frac{\partial(\rho e)}{\partial t} + \nabla \cdot (\rho e \mathbf{u}) = \underbrace{\rho \mathbf{g} \bullet \mathbf{u}}_{\text{power of gravity force}} + \underbrace{\nabla \cdot (\boldsymbol{\sigma} \bullet \mathbf{u})}_{\text{power of surface forces}} - \underbrace{\nabla \cdot \mathbf{q} + \rho Q}_{\text{net heat flux}}\,. \tag{2.13}$$

2.3. Discretisation

For the governing equations presented in the previous chapter to be implemented in CFD software such as `foam-extend`, they need to be discretised. The process of discretisation allows for the Scalar Transport Equation and the resulting governing equations to be solved numerically. The discretisation process consists of representing differential equations as algebraic expressions of equivalent properties, usually a matrix [6].

The discretisation of the transport equation in `foam-extend` is performed by implementing the Polyhedral Finite Volume Method in several steps [6]:

- Per-operator discretisation is performed by evaluating each term explicitly following a predetermined strategy and discretisating it.
- Space dicrtisation is performed use of a computational mesh as the spatial domain.

- Time is discretised by a series of time-steps adding up to the observed time interval.
- Spatial and temporal variations of a property ϕ are used to discretely represent field data.
- Integration over a cell (CV) is preformed.
- Spatial and temporal variations are use for discrete interpretation of operator terms.

The basis of the discretisation process is the definition of the space and time domains to be used. The temporal domain is defined by observing the chosen time interval as a series of consecutive time-steps. The spatial domain is represented by a finite number of control volumes (cells). A representation of one CV is given by a convex polyhedron shown in Fig. 2.3.

A polyhedral cell of volume V_P is defined with the cell centroid P and the centroid position vector $\mathbf{r}_P$ in regard to the origin of the global coordinate system. For a selected cell face f a surface normal vector $\mathbf{s}_f$ is defined with a magnitude equal to the area of the selected face S_f. Any neighbouring cell has a centroid N connected to the centroid of the main cell P by the delta vector $\mathbf{d}_f = \overline{PN}$ [6].
The definition of the cell centroid P as the main computational point is given by:

$$\int_{V_P} (\mathbf{x} - \mathbf{x}_P)\, dV = \mathbf{0}\,, \tag{2.14}$$

with the face centre f defined in the same manner:

$$\int_{S_f} (\mathbf{x} - \mathbf{x}_f)\, dS = \mathbf{0}\,. \tag{2.15}$$

In practice, faces of the polyhedral cell are not flat surfaces, meaning that the surface normal vector $\mathbf{s}_f$ must be calculated from the given integral:

$$\mathbf{s}_f = \int_{S_f} \mathbf{n}\, dS\,. \tag{2.16}$$

Solutions to discretised equations are stored in the cell centroid whereas the boundary data is stored in face centres of the boundary faces. Depending on situation and purpose of the data required, it may be necessary to access data stored in face centres of the finite volume cell. To access such data face interpolation schemes are used.

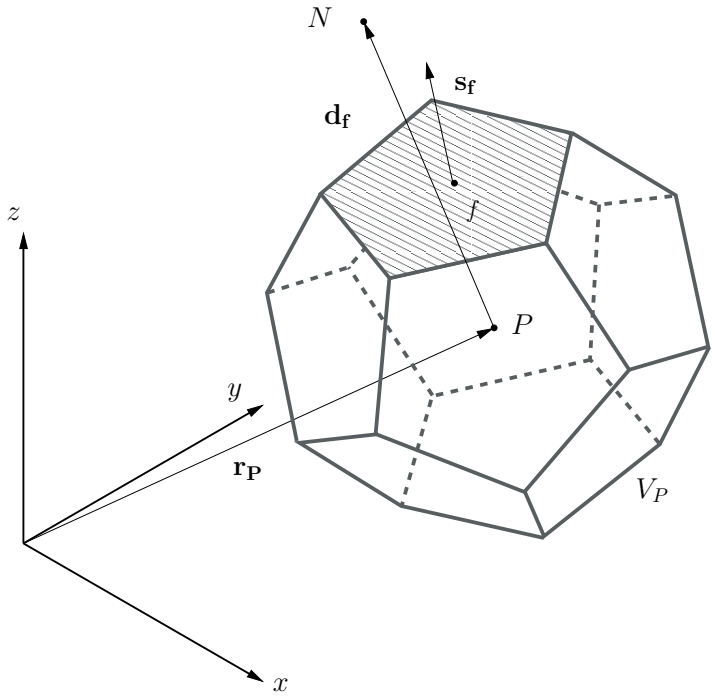

Figure 2.3: Polyhedral finite volume.

The second order discretisation of spatial variation for a general property ϕ is denoted by the following expression:

$$\phi(\mathbf{x}) = \phi_P + (\mathbf{x} - \mathbf{x}_P)\bullet(\nabla\phi)_P\,, \tag{2.17}$$

while second order temporal discretisation is given by:

$$\phi(t + \Delta t) = \phi^t + \Delta t \left(\frac{\partial\phi}{\partial t}\right)^t . \tag{2.18}$$

Where the value of ϕ at the centroid is given by $\phi_P = \phi(\mathbf{x}_P)$ and the value of ϕ at time t by $\phi^t = \phi(t)$.

Using Eq. 2.17 the volume integral can be evaluated as follows:

$$\begin{aligned}\int_V \phi\, dV &= \int_V \left[\phi_P + (\mathbf{x}-\mathbf{x}_P)\bullet(\nabla\phi)_P\right] dV \\ &= \phi_P \int_V dV + (\nabla\phi)_P \bullet \int_V (\mathbf{x}-\mathbf{x}_P) dV \\ &= \phi_P V_P \,,\end{aligned} \tag{2.19}$$

and the surface integral can be evaluated as:

$$\oint_S \mathbf{n}\,\phi\, dS = \sum_f \int_{S_f} \mathbf{n}\phi_f\, dS_f \tag{2.20}$$

$$= \sum_f \int_{S_f} \mathbf{n}[\phi_f + (\mathbf{x}-\mathbf{x}_f)\bullet(\nabla\phi)_f]\, dS_f \tag{2.21}$$

$$= \sum_f \mathbf{s}_f\phi_f \,.$$

The discretisation of the Scalar Transport Equation 2.7 is performed on a term-by-term basis starting from the integral form of the equation:

$$\int_V \frac{\partial\phi}{\partial t}\, dV + \oint_S \phi\,(\mathbf{n}\bullet\mathbf{u})\, dS - \oint_S \gamma\,(\mathbf{n}\bullet\nabla\phi)\, dS = \int_V Q_v\, dV \,, \tag{2.22}$$

resulting in the transfomation of the equation from a differential equation to a set of algebraic equations solved in matrix form.

2.3.1. Temporal Derivative Discretisation

The time derivative in Eq. 2.22 represents the rate of change of the property ϕ and can be disctretised as:

$$\frac{\partial\phi}{\partial t} = \frac{\phi^n - \phi^o}{\Delta t} \,. \tag{2.23}$$

Eq. 2.23 represents the first order approximation of the temporal derivative where:

- The field value of variable ϕ calculated for the new time-step t_{new} is defined as:

$$\phi^n = \phi(t = t_{new})\,. \tag{2.24}$$

- The field value of variable ϕ calculated for the previous time-step t_{old} is defined as follows:

$$\phi^o = \phi(t = t_{old})\,. \tag{2.25}$$

- The time-step size Δt can be expressed as:

$$\Delta t = t_{new} - t_{old}\,. \tag{2.26}$$

Backward differencing can be applied to express the second order approximation of the temporal derivative:

$$\frac{\frac{3}{2}\phi^n - 2\phi^o + \frac{1}{2}\phi^{oo}}{\Delta t}\,, \tag{2.27}$$

where the term ϕ^{oo} is expressed as $\phi^{oo} = \phi(t_{new} - 2\Delta t)$ and the time-step is assumed to remain constant. Integrating Eq. 2.26 and Eq. 2.27 over the volume of the cell produces yields:

$$\int_V \frac{\partial \phi}{\partial t}\, dV = \frac{\phi^n - \phi^o}{\Delta t} V_P\,, \tag{2.28}$$

$$\int_V \frac{\partial \phi}{\partial t}\, dV = \frac{\frac{3}{2}\phi^n - 2\phi^o + \frac{1}{2}\phi^{oo}}{\Delta t} V_P\,. \tag{2.29}$$

2.3.2. Convection Term Discretisation

The dicretisation of the convection term from Eq. 2.22 is accomplished by using the Gauss' Theorem 2.2 to transform the volume integral to a surface integral. The same process is applied for the discretisation of any terms consisting of either the gradient or the divergence operator. The convection term can now be expressed as:

$$\int_V \nabla \cdot (\phi \mathbf{u})\, dV = \oint_S \phi(\mathbf{n}\bullet\mathbf{u}) dS\,. \tag{2.30}$$

The surface integral can now be expressed as a sum of face integrals:

$$\oint_S \phi(\mathbf{n}\bullet\mathbf{u}) dS = \sum_f \phi_f(\mathbf{s}_f\bullet\mathbf{u}_f) = \sum_f F\,\phi_f\,, \tag{2.31}$$

where ϕ_f represents the value of ϕ at the face of the cell face and the flux F can be expressed as a product of the surface normal vector and the convective velocity $\mathbf{u}_f$:

$$F = \mathbf{s}_f\bullet\mathbf{u}_f\,. \tag{2.32}$$

Discretising the convection term as a sum of the products of all face-centred values of the property ϕ_f and the corresponding face flux F. The value of ϕ_f need to be evaluated by using ϕ_P and ϕ_N which can be achieved by using one of many existing interpolation schemes, e.g.:

- Central differencing - second order accuracy, but causing oscillation:

$$\phi_f = f_x\phi_P + (1 - f_x)\phi_N\,, \tag{2.33}$$

  where $f_x = \overline{fN}/\overline{PN}$.

- Upwind differencing - which takes into account the upstream information, producing no oscillations but smearing the solution:

$$\phi_f = max(F, 0)\,\phi_P + max(-F, 0)\,\phi_N\,. \tag{2.34}$$

2.3.3. Diffusion Term Discretisation

The diffusion term from the Scalar Transport Equation 2.22 can be discretizied by implementing the same method as the one used for the discretization of the convection term:

$$\begin{aligned}\int_V \nabla \cdot (\gamma \nabla \phi)\, dV &= \oint_S \gamma(\mathbf{n}\bullet\nabla\phi) dS \\ &= \sum_f \int_{S_f} \gamma(\mathbf{n}\bullet\nabla\phi)\, dS \\ &= \sum_f \gamma_f\, \mathbf{s}_f\bullet(\nabla\phi)_f\,.\end{aligned} \tag{2.35}$$

The term describing the face-normal gradient $\mathbf{s}_f\bullet(\nabla\phi)_f$ can be expressed as the difference of property ϕ across the face:

$$\mathbf{s}_f\bullet(\nabla\phi)_f = |\mathbf{s}_f|\frac{\phi_N - \phi_P}{|\mathbf{d}_f|}\,. \tag{2.36}$$

Eq. 2.36 is valid for orthogonal meshes, while for large non-orthogonality, correction terms must be applied.

2.3.4. Source/Sink Term Discretisation

Sources and sinks describe local effects and may be modelled by a function of space and time or any complex variable S. Thus, the discretisation produces:

$$\int_V S\, dV = SV_P\,, \tag{2.37}$$

where S may be linearised with respect to the general property ϕ as:

$$S(\phi) = S_u - S_p\phi\,. \tag{2.38}$$

2.3.5. Linear System of Equations

A system of linear equations is developed by discretisation of the Scalar Transport Equation 2.7. A linear equation is solved for every computational point (cell centroid P), where the solution of the equation depends on the values of neighbouring cell centroids N. A general form of the linear equation for a cell centroid P is given by:

$$a_P x_P + \sum_N a_N x_N = b\,. \tag{2.39}$$

For every time x_P depends on itself, contribution is added into a_P and for every time x_N depends on itself, contribution is added into a_N. Other contributions are added to b. If equation Eq. 2.39 is developed for each cell of the domain, a system of linear equations is constructed. It is usually written in matrix form:

$$[A][x] = [b]\,. \tag{2.40}$$

The matrix $[A]$ contains the coefficients a_P and a_N, the vector $[x]$ contains values of x_P for all cells in the domain and the vector $[b]$ represents the right-hand side. As the domain contains a large number of cells, each described by a separate linear equation, the matrix $[A]$ has a dimension of $N \times N$ cells, making it a square matrix. This can make the matrix large, however many coefficients are equal to zero and the matrix is sparse with the number of non-zero terms in each row being equal to the number of cell faces.

2.4. Boundary Conditions

As described in [6], boundary conditions are used to isolate the studied system from the rest of the environment and to limit what is to be modelled. The type and position of the boundary conditions to be applied depend on the physics governing the observed phenomena and good engineering practice. Numerical boundary conditions are frequently used in CFD to prescribe boundary behaviour. Most frequently used numerical boundary conditions include:

- The *Dirichlet* boundary condition, which prescribes a fixed value of ϕ at the

boundary:

$$\phi = const. \tag{2.41}$$

- The *Neumann* boundary condition, prescribing a zero gradient or no flux condition:

$$\mathbf{n} \cdot \mathbf{q}_s = 0\,. \tag{2.42}$$

- A *generalised Neumann* boundary condition, which prescribes a fixed gradient or fixed flux at the boundary:

$$\mathbf{n} \cdot \mathbf{q}_s = q_b\,. \tag{2.43}$$

- *Mixed* conditions can be used as a linear combination of *Neumann* and *Dirichlet* conditions:

$$\alpha\,\phi + (1-\alpha)\,\mathbf{n} \cdot \mathbf{q}_s\,. \tag{2.44}$$

- Geometric and Coupled boundary conditions such as symmetry plane, cyclic or periodic boundary conditions.

2.5. Pressure-Velocity Coupling Algorithms

The set of equations shown in Eq. 2.12 and 2.9 represents the Navier-stokes equations for incompressible flow. This set of equations represents one vector field governed by one vector equation and one scalar field governed by a scalar equation. These two equations are linearly coupled as the velocity governed by the momentum equation also appears as a velocity divergence in the continuity equation. As the pressure gradient is also present in the momentum equation, linear coupling between the pressure and the velocity is present.

As the pressure field is a scalar field and velocity represents a vector field, the two cannot be put in direct relation without the derivation of the pressure equation. The pressure equation can be derived by discretisation of the momentum equation as follows:

$$a_P^{\mathbf{u}}\mathbf{u}_P + \sum_N a_N^{\mathbf{u}}\mathbf{u}_N = \mathbf{r} - \nabla p\,. \tag{2.45}$$

All the right-hand-side contributions and the off-diagonal part of the matrix describing the momentum equation are combined in the newly introduced $\mathbf{H}(\mathbf{u})$ operator:

$$\mathbf{H}(\mathbf{u}) = \mathbf{r} - \sum_N a_N^{\mathbf{u}} \mathbf{u}_N \,. \tag{2.46}$$

By using Eq. 2.46, Eq. 2.45 can be transformed:

$$a_P^{\mathbf{u}} \mathbf{u}_P = \mathbf{H}(\mathbf{u}) - \nabla p \,, \tag{2.47}$$

which can be rearranged as:

$$\mathbf{u}_P = (a_P^{\mathbf{u}})^{-1} (\mathbf{H}(\mathbf{u}) - \nabla p) \,. \tag{2.48}$$

The resulting expression for $\mathbf{u}_p$ can now be substituted into the continuity expression for incompressible flow 2.9, producing the expression:

$$\nabla \cdot \left[(a_P^{\mathbf{u}})^{-1} \nabla p \right] = \nabla \cdot ((a_P^{\mathbf{u}})^{-1} \mathbf{H}(\mathbf{u})) \,. \tag{2.49}$$

Eq. 2.49 represents the pressure equation for incompressible flow and can be used to establish a direct coupling between pressure and velocity. To deal with solving the pressure-velocity coupling several coupling methods are used (e.g. SIMPLE, PIMPLE, PISO, block-coupled solvers, etc.). For the purpose of this Thesis, the SIMPLE and PIMPLE algorithms are used. The two algorithms are explained in the following sections with an addition of the PISO algorithm, as it its necessary for understanding the PIMPLE algorithm.

2.5.1. SIMPLE Algorithm

The Semi-Implicit Algorithm for Pressure-Linked Equations (SIMPLE) is the earliest pressure-velocity coupling algorithms used [7].

The SIMPLE algorithm as described in [6] follows the following sequence:

1. Initial guess of the pressure field p^*

2. The Momentum Predictor step: Momentum equation is solved using the guessed pressure.

$$a_P^{\mathbf{u}}\mathbf{u}_P = \mathbf{H}(\mathbf{u}) - \nabla p^* \tag{2.50}$$

3. The Pressure Correction Step: New pressure calculation based on the velocity field.

$$\nabla \cdot \left[(a_P^{\mathbf{u}})^{-1}\nabla p\right] = \nabla \cdot ((a_P^{\mathbf{u}})^{-1}\mathbf{H}(\mathbf{u})) \tag{2.51}$$

4. Conservative face flux F assembly based on the pressure solution.

$$F = \mathbf{s}_f \bullet \mathbf{H}(\mathbf{u}) - a_N^p(p_N - p_P) \tag{2.52}$$

5. Repeat until convergence is reached.

The algorithm presented above will diverge unless under-relaxation is introduced:

$$p^{**} = p^* + \alpha_P(p - p^*)\,, \tag{2.53}$$

$$\mathbf{u}^{**} = \mathbf{u}^* + \alpha_U(\mathbf{u} - \mathbf{u}^*), \tag{2.54}$$

where the following constraints must be met:

$$\begin{aligned} &0 < \alpha_P \leq 1\,, \\ &0 < \alpha_U \leq 1\,, \\ &\alpha_P + \alpha_U \approx 1\,. \end{aligned} \tag{2.55}$$

The terms p and $\mathbf{u}$ in Eq. 2.54 represent the current solution for pressure and velocity, while p^* and $\mathbf{u}^*$ denote the solution of the previous time-step. The terms α_P and α_P are the pressure and velocity under-relaxation factors and they define how much of the current solution and how much of the solution from the previous time-step will be taken into account for the new solution denoted by p^{**} and $\mathbf{u}^{**}$.

2.5.2. PISO Algorithm

The Pressure-Implicit algorithm with Splitting of Operators (PISO) is an extension of the basic SIMPLE algorithm using one predictor and two corrector steps [8].

An overview of the PISO sequence is given below:

1. The pressure field p^* from previous corrector or time-step is used, with the conservative fluxes corresponding to p^* also being available.

2. The momentum equation is discretised using the available flux field.

3. The Momentum Predictor step: Momentum equation is solved using the guessed pressure.
$$a_P^{\mathbf{u}}\mathbf{u}_P = \mathbf{H}(\mathbf{u}) - \nabla p^*$$

4. The Pressure Correction Step: New pressure calculation based on the velocity field.
$$\nabla \cdot \left[(a_P^{\mathbf{u}})^{-1}\nabla p\right] = \nabla \cdot ((a_P^{\mathbf{u}})^{-1}\mathbf{H}(\mathbf{u}))$$

5. Conservative face flux F assembly based on the pressure solution.
$$F = \mathbf{s}_f \bullet \mathbf{H}(\mathbf{u}) - a_N^p(p_N - p_P)$$

6. Cell-centred velocity field is updated explicitly with the assembled momentum coefficients.
$$\mathbf{u}_P = (a_P^{\mathbf{u}})^{-1}(\mathbf{H}(\mathbf{u}) - \nabla p)$$

7. If convergence is not reached, repeat from the pressure correction step.

8. Start from the beginning for new time-steps.

The main use of the PISO algorithm is for cases where the simulation time-step is controlled by physical constraints and where temporal accuracy is of great importance, i.e. Large Eddy Simulation [6].

2.5.3. PIMPLE Algorithm

The PIMPLE algorithm is a combination of the SIMPLE and PISO algorithms. It is frequently used for transient problems as it allows for large Courant numbers, which allows a large increase in time-step size of the simulation.

As explained in [9], the PIMPLE algorithm searches for the correct steady-state solution for each time-step using under-relaxation. The algorithm uses outer corrector loops to ensure convergence inside a time-step loop. When the defined tolerance criterion for the steady-state solution is reached, the outer correction loop is ended and the algorithm moves on to the next time-step.

2.6. Turbulence Modelling

Turbulence plays an important part in CFD simulations of turbomachines as its influence on the operation of turbomachinery can be significant. The stochastic nature of turbulent flows makes the task of modelling turbulence demanding field of study. The task of turbulence modelling is to create models and manipulate equations to be able to simulate turbulence interaction for specific conditions [6].

There exist several different approaches to turbulence modelling such as: Direct Numerical Simulation (DNS), Reynolds-Averaged Navier-Stokes Equations (RANS) and Large Eddy Simulation (LES).

The RANS model is frequently used in most turbomachinery CFD simulations. The basic idea of this model is to describe the variables of interest into fluctuating and mean values reducing the cost of simulation.

Reynolds-Averaged Navier-Stokes may be assembled by decomposing the values of pressure and velocity into a sum of mean ($\overline{\mathbf{u}}$, $\overline{p}$) and fluctuating values ($\mathbf{u}'$, p') as follows:

$$\mathbf{u} = \overline{\mathbf{u}} + \mathbf{u}' \,, \tag{2.56}$$

$$p = \overline{p} + p' \,. \tag{2.57}$$

By inserting Eq. 2.56 and 2.57 into Eq. 2.11 and eliminating products of mean and fluctuating values, the following expression is given:

$$\frac{\partial \overline{\mathbf{u}}}{\partial t} + \nabla \cdot (\overline{\mathbf{u}}\,\overline{\mathbf{u}}) - \nabla \cdot \left(\nu \nabla \overline{\mathbf{u}}\right) = -\nabla \overline{p} + \nabla \cdot (\overline{\mathbf{u}'\mathbf{u}'}) \,, \tag{2.58}$$

$$\nabla \cdot \overline{\mathbf{u}} = 0 \,,$$

where the term $\overline{\mathbf{u}'\mathbf{u}'}$ is a second rank symmetric tensor called the Reynolds stress tensor $\mathbf{R}$:

$$\mathbf{R} = \overline{\mathbf{u}'\mathbf{u}'} \,. \tag{2.59}$$

The Reynolds Stress tensor can be assembled by using the second rank symmetric mean velocity gradient $\overline{\mathbf{S}}$ and turbulent viscosity ν_t:

$$\mathbf{R} = \underbrace{\nu_t}_{\text{turbulent viscosity}} \underbrace{\frac{1}{2}\left[\nabla\overline{\mathbf{u}} + (\nabla\overline{\mathbf{u}})^T\right]}_{\text{tensor } \overline{\mathbf{S}}}, \tag{2.60}$$

where the turbulent viscosity ν_t is modelled using the velocity scale $\mathbf{U}$, the length-scale Δ and a dimensionless constant A, which allows the model to be tuned to actual physical phenomena:

$$\nu_t = A\,\mathbf{U}\Delta\,. \tag{2.61}$$

The velocity scale can be approximated using turbulent kinetic energy $U \approx |\mathbf{u}'|$, where the turbulent kinetic energy is given by:

$$k = \frac{3}{2}\mathbf{u}'^2\,. \tag{2.62}$$

Two frequently used two-equation models were used for turbulence modelling in the scope of this Thesis. The first was the $k-\varepsilon$ model and the second was the modified version of the $k-\omega$ model, the $k-\omega$ SST model.

2.6.1. The $k-\varepsilon$ Model

This model is a popular, yet simple, two-equation model consisting of two partial differential equations used to describe turbulence. The first of the two equations describes the turbulence kinetic energy k:

$$\frac{\partial k}{\partial t} + \nabla\cdot(\overline{\mathbf{u}}k) - \nabla\cdot[(\nu_{eff})\nabla k] = G - \varepsilon\,. \tag{2.63}$$

The second equation of the $k-\varepsilon$ model is the equation for the turbulent dissipation ε, i.e. the dissipation of the turbulent kinetic energy:

$$\frac{\partial \varepsilon}{\partial t} + \nabla \cdot (\overline{\mathbf{u}}\varepsilon) - \nabla \cdot [(\nu_{eff})\nabla \varepsilon] = C_1 \, G \frac{\varepsilon}{k} - C_2 \frac{\varepsilon^2}{k} \, . \tag{2.64}$$

Where the terms for G used in Eq. 2.63 and 2.64 and for ν_t are given by:

$$G = \nu_t \left[\frac{1}{2} (\nabla \overline{\mathbf{u}} + \nabla \overline{\mathbf{u}}^T) \right]^2 \, , \tag{2.65}$$

$$\nu_t = C_\mu \frac{k^2}{\varepsilon} \, . \tag{2.66}$$

A detailed overview of the model, its implementation and the various constants used, is given by Launder et al. in [10, 11].

2.6.2. The $k - \omega$ SST Model

The $k-\omega$ SST model is the result of combining the $k-\varepsilon$ model with the $k-\omega$ model developed by Wilcox [12]. The adaptation of the $k - \varepsilon$ model is used in the free-stream where the $k-\omega$ model shows sensitivity. For the inner boundary layer close to the wall, the $k - \omega$ model is used. The fundamental two-equation model is described by:

$$\frac{\partial k}{\partial t} + \nabla \cdot (\overline{\mathbf{u}} k) - \nabla \cdot [(\nu_{eff})\nabla k] = min \left(G, C_1, \beta^* k\omega \right) - \beta^* k\omega \, , \tag{2.67}$$

describing the turbulent kinetic energy k, and the following equation describing the specific dissipation rate ω:

$$\begin{aligned} \frac{\partial \omega}{\partial t} + \nabla \cdot (\overline{\mathbf{u}}\omega) - \omega \nabla \cdot \overline{\mathbf{u}} - \nabla \cdot [\nu_{eff} \nabla \omega] = \gamma \, min \left[S_2, \frac{c_1}{a_1} \beta^* \omega \, max \left(a_1 \omega, b_1 F_{23} \sqrt{S_2} \right) \right] \\ - \beta \omega^2 + (1 - F_1) C D_{k\omega} \, . \end{aligned} \tag{2.68}$$

Where the terms for G used in Eq. 2.67 are given by:

$$G = \nu_t S_2 \,, \tag{2.69}$$

$$S_2 = 2\left[\frac{1}{2}(\nabla\overline{\mathbf{u}} + \nabla\overline{\mathbf{u}}^T)\right]^2 \,, \tag{2.70}$$

and the turbulent viscosity ν_t is described by:

$$\nu_t = \frac{a_1 k}{max\,\left[a_1\omega, b_1 F_{23}\sqrt{2}\left|\frac{1}{2}(\nabla\overline{\mathbf{u}} + \nabla\overline{\mathbf{u}}^T)\right|\right]} \,. \tag{2.71}$$

Eq. 2.67 and 2.68 describe the $k-\omega$ SST model according to Menter and Esch [13] with updated coefficients from [14]. The consistent production term from [13] and [14] were updated according to [15], while the optional F_3 term was added according to [16].

2.7. Closure

In this chapter an overview of the Finite Volume Method was given, as well as the fundamental equations of fluid flow and their discretisation, so that they may be used for CFD simulations. A basic overview of the pressure-velocity coupling algorithms and turbulence models used in the scope of this thesis was also presented.

The next chapter deals with the theoretical background needed to develop a mathematical model used for turbomachinery CFD. In this chapter, various methods of domain and interface handling are presented and discussed.

3 Extensions of the Flow Model for Turbomachinery Applications

3.1. Introduction

The previous chapter gave a brief overview of the Finite Volume Method, which is an important basis for any CFD simulation. The present chapter deals with the theoretical background needed to extend the flow model for use in various approaches to CFD simulations of turbomachines. It also offers an overview of different interfaces that are at disposal for turbomachinery CFD. Methods used for domain and interface handling are presented. Domain handling deals with the way the rotation of moving components is handled in the computational domain, i.e. the computational mesh. Interface handling manages the way mesh regions are interconnected.

3.2. Domain Handling

The decision on how to approach domain handling in turbomachinery CFD depends on the way the domain is modelled. This, on the other hand, depends on whether the considered problem and connected phenomena need to be simulated using a steady-state or a transient approach.

The steady-state approach in turbomachinery CFD is also known as the "frozen rotor" approach. This is due to the fact that no actual movement of the mesh occurs and that movement is modelled by inclusion of additional terms into the equations of motion for the rotating region [17]. The "frozen rotor" approach is used when transient

phenomena are not dominant in the flow or are of no major significance to the analysis of the observed problem. The absence of actual mesh movement makes the frozen rotor model very robust and computationally less demanding, which makes it suitable for steady-state analysis of geometries with rotating and/or stationary parts.

If transient phenomena are to be modelled, the frozen rotor approach must be abandoned and the transient Moving (Dynamic) Mesh Model must be used instead. The use of a Moving Mesh Model makes the simulation require more computational resources, mainly because of the requirements of the transient simulation used with this model. The fact that any rotation of the mesh needs to be resolved by additional sets of equations compensating for topological changes of the computational domain, increases the computational effort only slightly. The actual cost of a dynamic mesh transient CFD simulation, when compared to a static mesh transient simulation, is lower than 5% of the computational effort per time-step [6]. Furthermore, interfaces are required to enable communication between the stationary and moving (rotating) portion of the mesh.

3.2.1. Moving Reference Frame

The use of Moving Reference Frame modelling in turbomachinery CFD simulations constitutes a way of representing the flow around moving parts of turbomachines as a steady-state problem. This is achieved by imposing a moving frame of reference created by selecting cells of the computational mesh (cell zones) with added inertia. The set of equations used to describe the motion of the mesh is modified by addition of acceleration terms occurring due to the transformation from the stationary reference frame to the moving reference frame [17].

If the entire domain (computational mesh) rotates as a single rotating frame, i.e. the whole domain can be modelled as a single moving zone, the Single Reference Frame (SRF) approach is used. An example of a geometry that is modelled as a single rotating zone is shown in Figure 3.1. As most turbomachines contain not only rotating, but also stationary parts, a single rotating zone cannot encompass the whole domain. In such cases the Multiple Reference Frame (MRF) approach is applied. The computational mesh is divided into different zones depending on the motion of the geometry, which are assigned either to the rotating or stationary frames of reference. Usually a part of the computational mesh close to the rotating part of the machine is selected as a zone in

the rotating frame of reference. Figure 3.2 shows a geometry consisting of a rotor and a stator (outer rim) with the rotating zone coloured red and the stationary part of the computational mesh shown in grey.

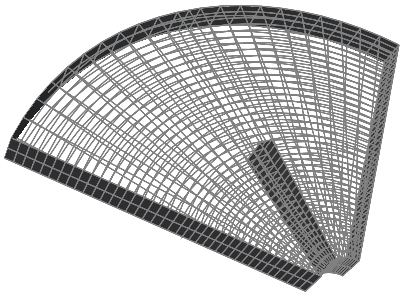

Figure 3.1: Example of a SRF model.

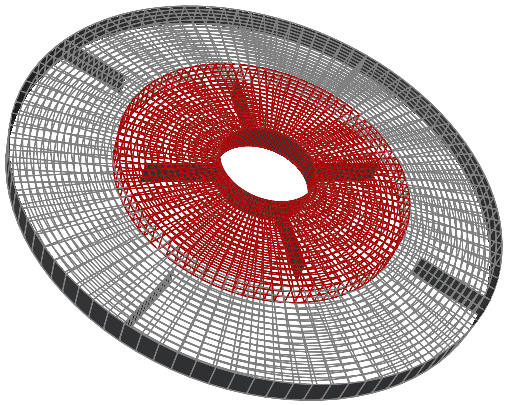

Figure 3.2: Example of a MRF model.

SRF Model

As previously described, the use of the SRF model is limited to simulations where the computed fluid flow adheres to the rotating turbomachinery, i.e. the entire computational domain moves with non-stationary geometry. The equations of motion are modified for the Moving Reference Frame and solved for the whole computational domain.

As presented in [18], when a general vector $\mathbf{a}$ is observed in an inertial frame of reference a term for the angular velocity $\boldsymbol{\omega}$ is added:

$$\left[\frac{\mathrm{d}\,\mathbf{a}}{\mathrm{d}t}\right]_I = \left[\frac{\mathrm{d}\,\mathbf{a}}{\mathrm{d}t}\right]_R + \boldsymbol{\omega} \times \mathbf{a}\,. \tag{3.1}$$

If the general vector $\mathbf{a}$ is substituted with the position vector $\mathbf{r}$, the following expression is presented:

$$\left[\frac{\mathrm{d}\,\mathbf{r}}{\mathrm{d}t}\right]_I = \left[\frac{\mathrm{d}\,\mathbf{r}}{\mathrm{d}t}\right]_R + \boldsymbol{\omega} \times \mathbf{r}\,. \tag{3.2}$$

By definition, the temporal derivation of the position vector $\mathbf{r}$ corresponds to velocity vector in either the inertial or relative frame of reference:

$$\mathbf{u}_I = \mathbf{u}_R + \boldsymbol{\omega} \times \mathbf{r}\,. \tag{3.3}$$

The term $\mathbf{u}_I$ in Eq. 3.3 represents the absolute velocity, i.e. the velocity as viewed from the stationary (inertial) frame of reference. On the other hand the term $\mathbf{u}_R$ represents the relative velocity as viewed from the rotating frame of reference. By substitution of the general vector $\mathbf{r}$ in Eq. 3.1 further derivation of Eq. 3.3 is performed:

$$\left[\frac{\mathrm{d}\,\mathbf{u}_I}{\mathrm{d}t}\right]_I = \left[\frac{\mathrm{d}\,\mathbf{u}_I}{\mathrm{d}t}\right]_R + \boldsymbol{\omega} \times \mathbf{u}_I\,. \tag{3.4}$$

The term $\mathbf{u}_I$ on the right-hand side of Eq. 3.4 may be replaced by Eq. 3.3 forming:

$$\left[\frac{\mathrm{d}\,\mathbf{u}_I}{\mathrm{d}t}\right]_I = \left[\frac{\mathrm{d}\,[\mathbf{u}_R + \boldsymbol{\omega} \times \mathbf{r}]}{\mathrm{d}t}\right]_R + \boldsymbol{\omega} \times [\mathbf{u}_R + \boldsymbol{\omega} \times \mathbf{r}]\,, \tag{3.5}$$

after sorting, the standard form for the acceleration in the inertial frame of reference becomes:

$$\left[\frac{\mathrm{d}\,\mathbf{u}_I}{\mathrm{d}t}\right]_I = \left[\frac{\mathrm{d}\,\mathbf{u}_R}{\mathrm{d}t}\right]_R + \underbrace{\frac{\mathrm{d}\,\boldsymbol{\omega}}{\mathrm{d}t} \times \mathbf{r}}_{\text{Tangential acceleration}} + \underbrace{2\boldsymbol{\omega} \times \mathbf{u}_R}_{\text{Coriolis acceleration}} + \underbrace{\boldsymbol{\omega} \times \boldsymbol{\omega} \times \mathbf{r}}_{\text{Centrifugal acceleration}}\,. \tag{3.6}$$

Equations 2.9 and 2.10 can be easily observed in the inertial frame forming the incompressible Navier-Stokes equations for the inertial frame of reference:

$$\begin{cases} \dfrac{D\mathbf{u}_I}{Dt} = \nabla \cdot\, (\nu_{\text{eff}} \nabla \mathbf{u}_I) - \nabla \dfrac{p}{\rho}\,, \\ \nabla \cdot \mathbf{u}_I = 0\,. \end{cases} \tag{3.7}$$

The Material Derivative in Eq. 3.7 can be expressed as a sum of local and convective rates of change:

$$\frac{D\phi}{Dt} = \frac{\partial \phi}{\partial t} + \nabla \cdot \mathbf{v}\,\phi \quad \longrightarrow \quad \frac{D\mathbf{u}_I}{Dt} = \frac{\partial \mathbf{u}_I}{\partial t} + \nabla \cdot\, (\mathbf{u}_I \mathbf{u}_I)\,. \tag{3.8}$$

Using Eq. 3.8 and the continuity equation $\nabla \cdot \mathbf{u}_I = 0$ the incompressible Navier-Stokes equation for the inertial frame becomes:

$$\begin{cases} \dfrac{\partial \mathbf{u}_I}{\partial t} + \nabla \cdot (\mathbf{u}_I \mathbf{u}_I) - \nabla \cdot\, (\nu_{\text{eff}} \nabla \mathbf{u}_I) = -\nabla \dfrac{p}{\rho}\,, \\ \nabla \cdot \mathbf{u}_I = 0\,. \end{cases} \tag{3.9}$$

The left-hand side of the momentum equation from Eq. 3.7 can be expanded by using the expression presented in Eq. 3.6:

$$\frac{D\mathbf{u}_I}{Dt} = \frac{D\mathbf{u}_R}{Dt} + \frac{\mathrm{d}\,\boldsymbol{\omega}}{\mathrm{d}t} \times \mathbf{r} + 2\boldsymbol{\omega} \times \mathbf{u}_R + \boldsymbol{\omega} \times \boldsymbol{\omega} \times \mathbf{r}\,. \tag{3.10}$$

Taking note of the fact that the continuity equation must be satisfied, i.e. $\nabla \cdot \mathbf{u}_R = \nabla \cdot \mathbf{u}_I = 0$ the following can be derived:

$$\begin{aligned} \nabla \cdot \mathbf{u}_R &= \nabla \cdot \mathbf{u}_I = 0 \\ &= \underbrace{\nabla \cdot \mathbf{u}_R}_{=0} + \underbrace{\nabla \cdot \left[\boldsymbol{\omega} \times \mathbf{r}\right]}_{=0} = 0\,, \end{aligned} \tag{3.11}$$

resulting in the equivalence: $\nabla \cdot \left[\boldsymbol{\omega} \times \mathbf{r}\right] = 0$. This can be used to transform the diffusion term Eq. 3.9 to a form suitable for the rotating frame of reference by taking notice of the relation shown in Eq. 3.3:

$$\begin{aligned} \nabla \cdot \nabla(\mathbf{u}_I) &= \nabla \cdot \nabla \left[\mathbf{u}_R + \boldsymbol{\omega} \times \mathbf{r}\right] = 0 \\ &= \nabla \cdot \nabla(\mathbf{u}_R) + \nabla \cdot \underbrace{\nabla(\boldsymbol{\omega} \times \mathbf{r})}_{=0}\,. \end{aligned} \tag{3.12}$$

By replacing the term $\frac{D\mathbf{u}_I}{Dt}$ in Eq. 3.7 with the expression shown in Eq. 3.10 and taking notice of Eq. 3.12, the following equation can be constructed:

$$\begin{cases} \dfrac{\partial \mathbf{u}_R}{\partial t} + \dfrac{\mathrm{d}\boldsymbol{\omega}}{\mathrm{d}t} \times \mathbf{r} + 2\boldsymbol{\omega} \times \mathbf{u}_R + \boldsymbol{\omega} \times \boldsymbol{\omega} \times \mathbf{r} + \nabla \cdot (\mathbf{u}_R \mathbf{u}_R) = \nabla \cdot \left(\nu_{\text{eff}} \nabla \mathbf{u}_R\right) - \nabla \dfrac{p}{\rho}\,, \\ \nabla \cdot \mathbf{u}_R = 0\,. \end{cases} \tag{3.13}$$

For steady-state simulations, usually used with Moving Reference Frame methods, the temporal derivatives are disregarded and the expression can be written as follows:

$$\begin{cases} \nabla \cdot (\mathbf{u}_R \mathbf{u}_R) + \underbrace{2\boldsymbol{\omega} \times \mathbf{u}_R}_{\text{Coriolis force}} + \underbrace{\boldsymbol{\omega} \times \boldsymbol{\omega} \times \mathbf{r}}_{\text{Centrifugal force}} = \nabla \cdot \left(\nu_{\text{eff}} \nabla \mathbf{u}_R\right) - \nabla \dfrac{p}{\rho}\,, \\ \nabla \cdot \mathbf{u}_R = 0\,. \end{cases} \tag{3.14}$$

The Equations 3.14 constitute the steady-state incompressible Navier-Stokes equations in the rotating frame of reference. This equation is the governing equation used

to solve steady fluid flow in the SRF method. As stated in [17], feasible steady-state solutions using this method are possible, provided the correct boundary conditions are applied and that the following requirements are met:

- Walls defining the boundary can assume any shape as long as they move with the rotating reference frame.
- Walls can be defined as stationary with respect to the inertial reference frame only if they correspond to surfaces of revolution about the axis of rotation.
- In case of the wall rotating with the frame of reference, a no slip boundary condition must be applied in the rotating frame, making the relative velocity of the walls zero. In case of the walls defined as stationary with respect to the inertial frame, the no slip boundary condition in the inertial frame of reference is applied making the absolute velocity zero on the stationary walls.
- The use of cyclic boundaries is possible as long as the surface defining the boundary is rotationally periodic about the axis of rotation.
- 3D geometries are defined taking notice of the origin and axis of rotation for the rotating frame (cell zone). Using the origin of the global coordinate system as the reference frame origin and either the x, y or z axis as the axis of rotation is recommended.

Due to a high degree of coupling between the momentum equations when solving for fluid flow in the moving reference frame, instabilities may arise. Large rotational terms lead to a large radial pressure gradient, inducing flow in both the axial and radial direction. Some techniques are offered [17] to help reach convergence if such instabilities arise: gradually increasing the rotational speed starting from lower values, fine mesh resolution allowing for resolution of large pressure gradients, lowering the under-relaxation factors for the velocity, etc.

Geometry found in most turbomachinery rarely meets the previously stated prerequisites without considerable simplification. If stationary parts of the geometry do not correspond to surfaces of rotation, the model needs to be broken up into rotating and stationary zones. In such cases use of the MRF model is required.

MRF Model

The basis of the Multiple Reference Frame (MRF) model is the idea that the computational domain can be broken up into zones, each assigned with different motion. The flow for each zone is solved using equations of motion modified for the moving reference frame and with terms describing different rotation or translation [17].

The MRF approach models fluid flow using both the stationary and the rotating frames of reference. The rotating part of the domain (rotating zone) is solved using equations of motion in the rotating (relative) frame, while the stationary part (zone) is solved in the stationary frame. For stationary zones the equations of motion are reduced to their stationary forms. In both the rotating and stationary zones, vectors are defined for the global Cartesian coordinate system. The equations can also be solved for the locally defined velocity in the relative frame of reference, but this would require the use of jump conditions for the velocity at the rotor-stator interface.

The governing equations of the MRF method can be derived using the equations presented in the previous section. The term representing the convected velocity in Eq. 3.14 may be further developed [18]:

$$\begin{aligned}\nabla\cdot(\mathbf{u}_R\mathbf{u}_R) &= \nabla\cdot(\mathbf{u}_R\left[\mathbf{u}_I-\boldsymbol{\omega}\times\mathbf{r}\right)]\\ &= \nabla\cdot(\mathbf{u}_R\mathbf{u}_I)-\underbrace{\nabla\cdot\mathbf{u}_R}_{=0}(\boldsymbol{\omega}\times\mathbf{r})-\underbrace{\mathbf{u}_R\cdot\nabla(\boldsymbol{\omega}\times\mathbf{r})}_{\boldsymbol{\omega}\times\mathbf{u}_R}\\ &= \nabla\cdot(\mathbf{u}_R\mathbf{u}_I)-\boldsymbol{\omega}\times\mathbf{u}_R\,.\end{aligned} \tag{3.15}$$

The final form of Eq. 3.15 can be inserted into the left-hand side of the momentum equation from Eq. 3.14 transforming the left-hand side as follows:

$$\begin{aligned}\nabla\cdot(\mathbf{u}_R\mathbf{u}_R)+2\boldsymbol{\omega}\times\mathbf{u}_R+\boldsymbol{\omega}\times\boldsymbol{\omega}\times\mathbf{r} &= \nabla\cdot(\mathbf{u}_R\mathbf{u}_I)-\boldsymbol{\omega}\times\mathbf{u}_R+2\boldsymbol{\omega}\times\mathbf{u}_R+\boldsymbol{\omega}\times\boldsymbol{\omega}\times\mathbf{r}\\ &= \nabla\cdot(\mathbf{u}_R\mathbf{u}_I)+\boldsymbol{\omega}\times\mathbf{u}_R+\boldsymbol{\omega}\times\boldsymbol{\omega}\times\mathbf{r}\\ &= \nabla\cdot(\mathbf{u}_R\mathbf{u}_I)+\boldsymbol{\omega}\times\underbrace{(\mathbf{u}_R+\boldsymbol{\omega}\times\mathbf{r})}_{=\mathbf{u}_I}\\ &= \nabla\cdot(\mathbf{u}_R\mathbf{u}_I)+\boldsymbol{\omega}\times\mathbf{u}_I\,.\end{aligned} \tag{3.16}$$

With the final form of Eq. 3.16 replacing the left-hand side of the momentum equation Eq. 3.14 and by taking notice of Eq. 3.12, the governing equation used in the MRF

method may be presented:

$$\begin{cases} \nabla \cdot (\mathbf{u}_R \mathbf{u}_I) + \boldsymbol{\omega} \times \mathbf{u}_R = \nabla \cdot (\nu_{\text{eff}} \nabla \mathbf{u}_I) - \nabla \dfrac{p}{\rho}\,, \\ \nabla \cdot \mathbf{u}_R = 0\,. \end{cases} \tag{3.17}$$

The equations presented above form the steady-state incompressible Navier-Stokes equation for the rotating frame of reference with absolute convected velocity. To resolve fluid flow of rotating zones in the MRF model, Eq. 3.17 is used. To resolve fluid flow in stationary zones, the steady-state equation in the inertial (stationary) frame is used, which follows from Eq 3.9:

$$\begin{cases} \nabla \cdot (\mathbf{u}_I \mathbf{u}_I) - \nabla \cdot (\nu_{\text{eff}} \nabla \mathbf{u}_I) = -\nabla \dfrac{p}{\rho}\,, \\ \nabla \cdot \mathbf{u}_I = 0\,. \end{cases} \tag{3.18}$$

The MRF approach combines the use of stationary and rotating zones. The interaction of neighbouring cell zones is performed by transformation in a local reference frame allowing flow variables in one zone to be used to calculate fluxes at the boundary of the adjacent zone [17]. Same as with SRF, several limitations are imposed on the use the MRF model [17]:

- The interface separating a moving frame must be oriented in a way that the rotational velocity normal to the interface is zero. This means that interfaces should be parallel to the translational velocity for a translational frame or, in case of a rotating frame, should be surfaces of revolution around a rotational axis.
- The MRF method is not suitable for accurate modelling of axisymmetric swirl.
- Translational and rotational velocities are assumed to be constant through time.
- MRF is applicable only for steady-state flow.

The MRF model is a good option when modelling turbomachinery with one or more rotating parts. This method produces good results when modelling cases without strong influence of transients or for when transient phenomena are not the object of study. The results of MRF simulations may be used to initialize transient simulations when transient flow at the beginning of the simulation is of no interest. When a case with strong influence of transients is studied, the Moving Mesh model should be used.

3.2.2. Moving Mesh

When simulating time-varying geometry without the use of Moving Reference Frame methods, the computational domain is modelled in such a way that it changes during the simulation. Such motion can either be prescribed as a pre-defined sequence or can be solution-dependent. Solution-dependent mesh motion means that solution parameters influence the shape of the computational mesh [19]. As most turbomachines operate in such a way that a control volume with fixed boundaries can be determined, solution-dependent mesh motion is not common practice in tubomachinery CFD. When simulating turbomachines, non-deforming meshes with a fixed topology and prescribed mesh motion are generally used.

For simulation of mesh movement using the FVM, the governing conservation laws need to be rewritten as to take into account the movement of the computational mesh. The General Transport Equation 2.7 for a static mesh is used assuming $V = const.$ and as such is used in its differential form. For a moving mesh the integral form of the General Transport Equation is used:

$$\int_V \frac{\partial \phi}{\partial t}\, dV + \oint_S \phi \left[\mathbf{n} \cdot (\mathbf{u} - \mathbf{u}_b)\right]\, dS - \oint_S \gamma (\mathbf{n} \cdot \nabla \phi)\, dS = \int_V q_v\, dV\,. \tag{3.19}$$

Further modification of Eq. 3.19 is needed[20]. The term describing the rate of change should be changed to account for the changing volume:

$$\int_V \frac{\partial \phi}{\partial t}\, dV \approx \frac{\phi^n V^n - \phi^o V^o}{\Delta t}\,, \tag{3.20}$$

and the convection term should incorporate the relative velocity $\mathbf{u}_r = \mathbf{u} - \mathbf{u}_b$ resulting from the movement of the mesh:

$$\oint_S \phi \left[\mathbf{n} \cdot (\mathbf{u} - \mathbf{u}_b)\right]\, dS = \sum_f \int_S \phi_f \left[\mathbf{n} \cdot (\mathbf{u} - \mathbf{u}_b)\right]\, dS_f = \sum_f \phi_f F_r\,. \tag{3.21}$$

The term F_r from Eq. 3.21 denotes the relative flux and is expressed as:

$$\begin{aligned} F_r &= \mathbf{s}_f \cdot (\mathbf{u} - \mathbf{u}_b) = F - F_b\,, \\ F_b &= \mathbf{s}_f \cdot \mathbf{u}_b\,. \end{aligned} \tag{3.22}$$

As stated in [20], an auxiliary law is derived to aid in resolving problems concerning mesh motion. Describing the Conservation of Space, it checks for numerical consistency

during the discretisation of a moving mesh:

$$\int_V \frac{\partial V}{\partial t} - \oint_S (\mathbf{n} \cdot \mathbf{u}_b)\, dS = 0\,. \tag{3.23}$$

The flux through the moving boundary surface F_b from Eq. 3.22 cannot be calculated using the velocity of the moving boundary $\mathbf{u}_b$, as it would not satisfy the Space Conservation Equation 3.23. Instead, the discrete form of the Space Conservation Law is used:

$$\frac{V^n - V^o}{\Delta t} - \sum_f F_b = 0\,. \tag{3.24}$$

Knowing old and new point positions in a moving mesh enables direct calculation of volumes for new (V^n) and old (V^o) point positions for a certain time-step. The resulting volume swept by a face in motion V^f can be used to determine the flux F_b:

$$F_b = V_f/\Delta t\,. \tag{3.25}$$

Boundary conditions used in static mesh simulations are defined using absolute velocity. This means that all velocity boundary condition used in moving mesh models need to be modified to account for velocity of the moving walls. To resolve this, a Moving Wall Velocity boundary condition is introduced [20]. This special boundary condition is used on moving walls to specify a boundary velocity in a local (moving) coordinate system and adjusting the normal component of velocity by using the calculated mesh motion flux.

For transient simulation of turbomachines, motion (rotation) is added to certain parts of the computational mesh. The definition and details of the desired motion are defined using Dynamic Mesh Motion, found in `foam-extend`. Dynamic Mesh Motion combines topology modifiers with user-prescribed definitions of moving surfaces, based on turbomachine geometry, to actuate motion in pre-defined regions (zones) of the computational domain. The coupling between the mesh regions with defined mesh motion and the rest of the computational mesh is handled by interfaces facilitating communication.

3.3. Interface Handling

Depending on the choice of domain handling, i.e. choice of the type of simulation used for turbomachinery CFD, the computational domain may consist of several regions. Multi-region domains are necessary when simulating motion in the domain, both using steady-state (MRF) and transient (Dynamic Mesh) approaches. To facilitate communication between disconnected domains consisting of several regions, interfaces connecting the domains are introduced.

A discontiguous computational mesh may also be a product of combining different domains in order to create a single mesh for later use in the simulation. The process of merging meshes that do not connect ideally requires the use of interfaces to enable adequate communication between connected domains.

Furthermore, special interfaces are also used when only part of a circumferentially periodic geometry is simulated. In such cases, only that part of the domain which encapsulates the repetitive portion of geometry is chosen. A great example would be using only a quarter of the domain when simulating flow around a four-bladed propeller.

A number of interfaces are available for establishing communication between mesh regions depending on domain-handling, expected results, phenomena under investigation, geometry used and temporal discretisation. The following interfaces, which are available in `foam-extend`, are of interest to the subject of this Thesis and shall be described in detail: General Grid Interface (`ggi`), `overlapGgi`, `cyclicGgi` and the mixing plane interface (`mixingPlane`).

3.3.1. General Grid Interface

Typical operation of turbomachines involves a number of components in relative motion which needs to be taken into account when performing CFD simulations. Typical methods of handling relative motion (rotation) in CFD involve the creation of different zones inside the computational domain, making the domain discontiguous. To join multiple regions of a computational domain (mesh) into a single contiguous mesh, coupling interfaces are introduced.

Implicit coupling interfaces, such as the `cyclic` or `processor` found in `foam-extend`, are used for establishing communication between conformal mesh regions. A mesh region is described as conformal when patch nodes on each side of a connecting interface

correspond one-to-one [21]. When dealing with turbomachinery CFD, conformal mesh regions are rarely found, prompting the use of the General Grid Interface (GGI). The GGI is a coupling interface designed to connect mesh regions with non-matching patch nodes on different sides of the interface, i.e. non-conformal meshes.

The use of GGI resolves a number of problems in both steady-state and transient CFD simulations of turbomachines. It provides communication between non-conformal mesh regions with different levels of discretisation. Different levels of discretisation are used for complex geometries as a way of ensuring numerical stability without compromising the geometry [21]. Furthermore, GGI can be used to establish communication between mesh zones with assigned relative rotation making them non-conformal, and the rest of the domain, Fig. 3.3.

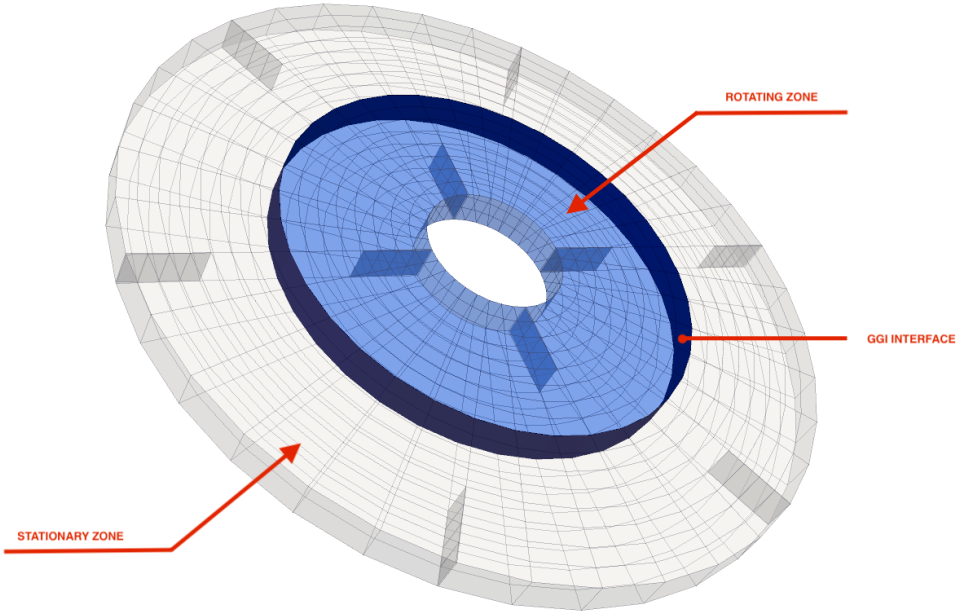

Figure 3.3: Exmaple of usage of GGI.

The idea behind GGI is to enable coupling between non-conformal mesh regions at the level of discretisation, without the need to use topological changes and re-meshing of cells next to the interface, as is the case when using Sliding Interface models [22].

Governing Equations

As presented in [21] the governing equations of GGI are based on weighted interpolation as a way of evaluating and transmitting variables (flow values) across a pair of patches, either conformal or non-conformal in nature. The objective of the GGI algorithm is to establish coupling at the matrix level, which directly corresponds to the discretised form of the interface equations where a topological change with face cutting would occur. As `foam-extend` offers support for arbitrary polyhedral cells at matrix level, both the Sliding Interface approach and GGI can be applied. To achieve this, a special from of interface discretisation, which relies on GGI interpolation, is used. A master patch and a slave patch are defined on a pair of coupled patches with the flow values between the two patches controlled by equations derived from FVM discretisation:

$$\Phi_{S_i} = \sum_n W_{M_n\_to\_S_i} \, \Phi_{M_n} \, , \tag{3.26}$$

$$\Phi_{M_j} = \sum_m W_{S_m\_to\_M_j} \, \Phi_{S_m} \, . \tag{3.27}$$

Equation 3.26 controls the variables from the master patch to the slave patch by using a master facet to shadow facet weighting factor $W_{M_n\_to\_S_i}$. On the other hand, Eq. 3.27 controls the variables from the slave patch to the master patch using a shadow to master facet weighting factor $W_{S_m\_to\_M_j}$.

For the FVM reasoning to be valid and the interface discretisation to remain conservative, constraints must be applied to the weighting factors:

$$\sum_n W_{M_n\_to\_S_i} = 1 \, , \tag{3.28}$$

$$\sum_m W_{S_m\_to\_M_j} = 1 \, . \tag{3.29}$$

Additionally the product of the facet surface area and the corresponding weighting factor for shadow and master facets must be equal to the surface area of the intersection between master and shadow facets:

$$W_{M_n\_to\_S_i} \, |S_{M_n}| = W_{S_m\_to\_M_j} \, |S_{S_m}| = |S_{\cap M\_to\_S}| \, . \tag{3.30}$$

Furthermore, symmetry constraints need to be applied:

$$\begin{aligned} if \quad W_{M_n\_to\_S_i} > 0 \quad &\Rightarrow \quad W_{S_m\_to\_M_j} > 0\,, \\ & W_{M_n\_to\_S_i} \neq W_{S_m\_to\_M_j}\,. \end{aligned} \tag{3.31}$$

The presented constraints help in assuring the computation of correct weighting factors and, as such, assure correct distribution of flow values across the interface. Their importance is made clear by the fact that even minimal errors in weighting factors lead to significant errors in the discretisation process.
Eq. 3.30 can be used to determine the values of necessary weighting factors:

- Master to shadow patch weighting factor:

$$W_{S_m\_to\_M_j} = \frac{|S_{\cap M\_to\_S}|}{|S_{M_n}|}, \quad W_{S_m\_to\_M_j} \in [\,0, 1\,]\,. \tag{3.32}$$

- Master to shadow patch weighting factor:

$$W_{M_n\_to\_S_i} = \frac{|S_{\cap M\_to\_S}|}{|S_{S_m}|}, \quad W_{M_n\_to\_S_i} \in [\,0, 1\,]\,. \tag{3.33}$$

Other Considerations

The GGI weighting factors calculated from Eq. 3.32 and 3.33 represent percentages of surface interaction between a pair of overlapping faces. By using the aforementioned equations, weighting factor values are produced solely by using values of facet area and polygonal intersection [21]. As shown by Eq. 3.31 the weighting factors must be greater than zero, which is made obvious by the fact that a zero value weighting factor would mean that the two faces in a patch pair do not intersect. The surface area of the master/shadow patch intersection used in Eq. 3.32 and 3.33 is determined by the Sutherland-Hodgman algorithm [23]. The algorithm is designed as a simple and fast algorithm, robust enough to handle convex n-sided polygon.

The occurrence of non-overlapped facets produces weighting factors with zero value and is specially handled by the GGI interface. Non-overlapped faces are treated as an error in the geometry and are reassigned to a symmetry plane boundary condition. On the other hand, the GGI interface can also be used when the weighting factor equals 1,

i.e. for conformal coupled patches. Such use of GGI is required when creating meshes from multiple parts which results in leftover internal faces.

3.3.2. `overlapGgi`

The basic GGI interface operates on coupled patches by interpolating between the master and shadow patches and updating the flow values accordingly. The basic algorithm was modified to work with cases where full coverage of interfaces is not possible [17], an example of which can be seen in Fig. 3.4. Such cases cases are standard when working with turbomachines where the rotor and stator have different pitch (Fig. 3.5).

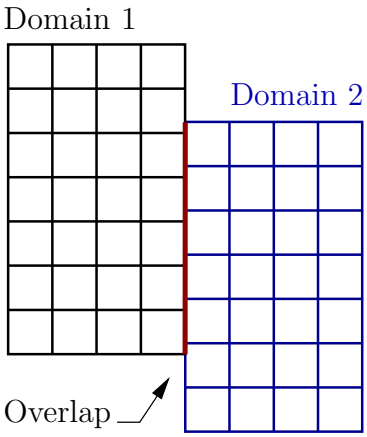

Figure 3.4: Example of partially overlapping meshes.

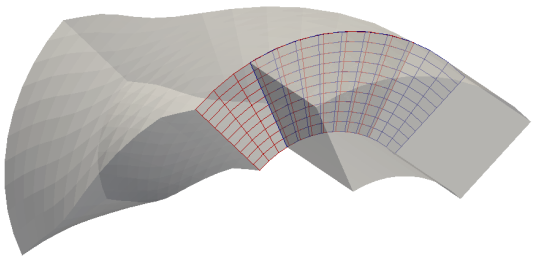

Figure 3.5: Rotor-stator interaction with overlap.

The `overlapGgi` algorithm builds on the basic GGI to achieve full overlap for partially overlapping faces. Transformed surfaces of the shadow patch are created by copying the patch geometry multiple times. The geometry is copied as many times as necessary to achieve full overlap of the master and shadow patch. Transformation of the data (scalar, vector or tensor) is performed and the data is expanded over the copied patch. Then, after the data has been populated for the full 360 degrees, standard GGI interpolation is used [24].

3.3.3. `cyclicGgi`

Another variant of the GGI widely used in turbomachinery CFD is the `cyclicGgi`. An important prerequisite for `cyclicGgi` to be applicable is that the geometry used and the phenomena simulated are periodically repetitive. If such requirements are met, general periodic boundary condition, such as the `cyclic` boundary condition, may be used. If the periodic planes of the cyclic computational domain do not have identical (conformal) meshes, the ordinary `cyclic` interface cannot be applied. For this reason the GGI algorithm was modified to work with cyclically periodic boundaries, resulting in the `cyclicGgi` interface.

Several improvements of the `cyclicGgi` over the `cyclic` interface are presented in [17]:

- Cyclic boundary conditions require both boundaries of the periodic geometry to be defined as one patch with the first half of the patch faces representing one side of the cyclic boundary and the second half of the faces representing the other side. The use of the `cyclicGgi` nullifies this requirements, allowing for separate patches to be defined as periodic boundaries.
- Use of the `cyclicGgi` interface does not require the interface to be flat, as is the case with cyclic boundary conditions, but requires constant rotational pitch for the whole interface.
- Whereas the cyclic boundary conditions only allow for completely matching meshes of the periodic boundary, `cyclicGgi` allows for non-conformal boundary meshes.
- `cyclicGgi` does not require boundary patches defining the periodic domain to be planar, which is a necessary requirement of the cyclic boundary condition.

Figures 3.6 and 3.7 show potential uses of the `cyclicGgi` interface. While Fig. 3.6 shows a simple depiction of rotor stator interaction with both the `cyclicGgi` and `overlpaGgi`, Fig. 3.7 shows a more complex use of `cyclicGgi` in an axial turbine. A periodic part of a single passage through a rotor of an axial turbine is shown, expanding the use of `cyclicGgi` for non-planar and non-conformal periodic patches.

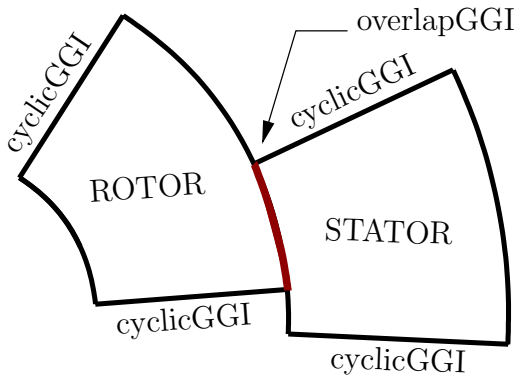

Figure 3.6: Rotor-stator interaction with cyclicGGI.

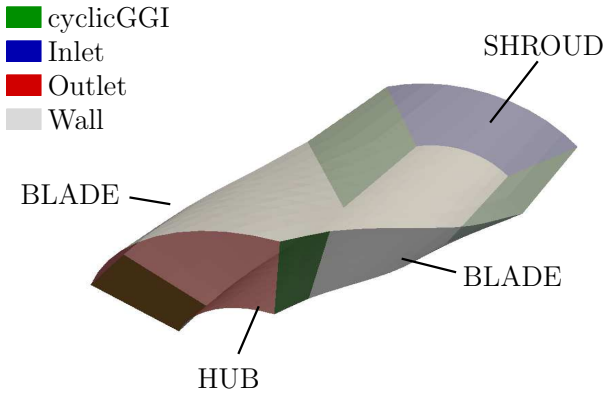

Figure 3.7: Axial turbine stage with cyclicGGI.

The `cyclicGgi` uses the same basic algorithm as GGI with the addition of an internal transform to the shadow patch. The transformation is achieved by superposing shadow patch data over master patch data to help determine the neighbours of the `cyclicGgi` patch faces, compute weighting factors and transform shadow patch vector fields before computation of the GGI weighted interpolation [21].

3.3.4. Mixing Plane Interface

The Mixing Plane Interface (`mixingPlane`) is an alternative to the GGI interface based on circumferential averaging or "mixing". Similarly to GGI, the `mixingPlane` model facilitates non-conformal interpolation between coupled patches.

One of the requirements of the MRF model stated in [17] is that the flow at the interface between neighbouring moving and stationary zones must be as closely uniform as possible. Non-uniform flow at the interface produces solution that are not physically meaningful. In realistic turbomachinery each row of blades leaves significant flow features that interact with the next blade row (e.g. shear layers, fluctuating turbulence, turbulent wakes). This makes it impossible to define a steady-state for simulations using approaches such as the "frozen rotor" approach because, in reality, the point where the flow impacts on the blade in the following row changes with rotation. This is solved by stating that the downstream rotor blade row will see the mean flow conditions of the

upstream flow. To achieve this, it is necessary to perform averaging in the sweeping direction. The `mixingPlane` model, which uses averaging to "mix out" the flow, makes the flow uniform. Furthermore, the `mixingPlane` model provides a great alternative when simulating simplified turbomachinery components that connect to full-geometry components. This is because for complex geometries, such as multi-stage turbomachinery with varying number of blades in each row, which require large meshes consisting of several blade passages to maintain circumferential periodicity, the use of unsteady models is highly impractical [17]. Using the `mixingPlane` model for such cases produces steady-state results reducing the computational time required and boosting cost-effectiveness, while providing averaged data.

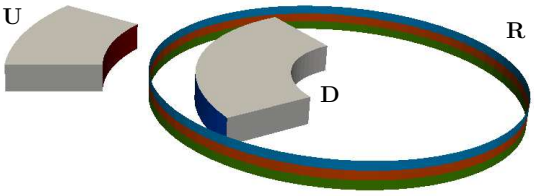

Figure 3.8: Upstream (U) and downstream (D) domains with ribbon patchs (R).

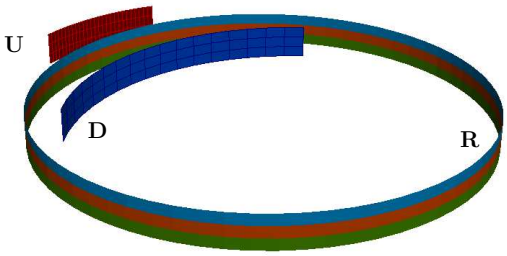

Figure 3.9: Upstream (U), downstream (U) and ribbon (R) patches.

The `mixingPlane` interface builds upon the GGI algorithm by using an intermediate patch surface to handle interpolation between two modified GGI interfaces. The intermediate patch surface is cylindrical or radial and consists of a stack of 360° ribbons shared by the GGI interfaces on both sides. The 2D profiles of the upstream and downstream GGI interfaces are used as basis for discretisation generating the intermediate ribbon patch. The `mixingPlane` averaging factors are computed based on the GGI weighting factors and the shape of the intermediate patch ribbons [25]. The aforementioned upstream (U) and downstream (D) interfaces and the `mixingPlane` ribbon patch (R) can be seen in Figures 3.8 and 3.9.

The `mixingPlane` model deals with each fluid zone (region of the computational domain) as a separate steady-state problem. Communication between adjacent zones is established by passing flow-field data as partially averaged boundary conditions through the `mixingPlane` interface. The data is averaged at prescribed iteration intervals by

either area-weighted averaging, mass averaging or mixed-out averaging, as a combination of the previous two averaging methods. Circumferential averaging along the ribbons of the intermediate patch is used to compute flow values which are then used to update boundary condition along the interface. The use of such averaging removes potential unsteadiness due to variations in passage-to-passage flow fields, producing a steady-state result that provides a good approximation of the time-averaged flow field [17].

3.4. Closure

This chapter presented the theoretical background needed for understanding the various approaches to domain handling and interface handling used in turbomachinery CFD. The basis of the Moving Reference Frame steady-state models (SRF and MRF) was presented alongside the Moving Mesh transient model. The available interpolation interfaces used for coupling of non-conformal meshes, such as the GGI (`ggi`) and Mixing Plane (`mixingPlane`) interfaces, were presented. Finally, variants of the GGI model used with partially overlapping patches (`overlapGgi`) and cyclically periodic domains (`cyclicGgi`) were discussed.

The next chapter introduces the Contra-Rotating Propeller set as a good example of an unshrouded turbomachine, which can be simulated by using various domain and interface handling techniques described above. Benefits of contra-rotating propellers and their implementation are discussed, with an overview of previous and connected research also presented.

4 Contra-Rotating Propellers

4.1. Introduction

The previous chapter gives an overview of various methods of domain and interface handling and their implementation in turbomachinery CFD.

The following chapter includes a description of the Contra-Rotating Propellers set (CRP), its operation, benefits and implementation. An overview of previous studies regarding CRP sets is made, focusing on the experimental studies used, which are later used for comparison with data produced by numerical simulations in this thesis. Furthermore, an overview of CRP characteristics is given in form of hydrodynamic coefficients and the Q-criterion, as a mean of visualising vorticity.

4.2. Design, Development and Benefits

Conventional single-blade propellers have been used as predominant means of propulsion for ships and submarines since the late 19^{th} century. With an increasing complexity of maritime propulsion and a continued need to design faster, more reliable and quieter means of propulsion with greater manoeuvrability, the focus shifted towards Contra-Rotating Propellers [26].

The Contra-Rotating Propeller set (CRP) usually consists of two propellers with collinear axes rotating in opposite directions. The main reason for employing such a design is the idea that positioning a secondary propeller behind the main propeller and having it rotate in the opposite direction positively affects the performance of the propulsion system and removes the bulk of the torque transferred from the propeller to

the vessel. This is due to the fact that the secondary propeller harvests the additional energy otherwise lost in the rotating flow.

Classic CRP design recognises two approaches to CRP installation with regard to shaft design [27]: coaxially mounted and single shaft CRP. Coaxially mounted CRP set consists of two propellers fitted on two separate shafts with coaxial axes of rotation. The main (fore) propeller is fitted on the main shaft, with the secondary (aft) propeller mounted on a shaft positioned behind the main propeller. Single shaft CRP design features both the fore and the aft propeller on a single shaft (Fig. 4.2). Such design is historically older than the dual-shaft design and was abandoned because of problems with inner shaft lubrication, which lead to the stagnation of further CRP research in general [28].

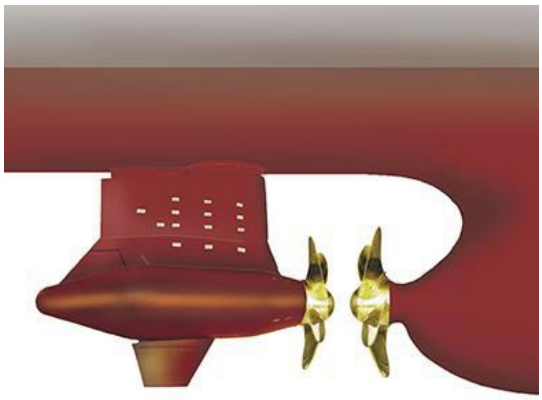

Figure 4.1: Podded CRP design [1].

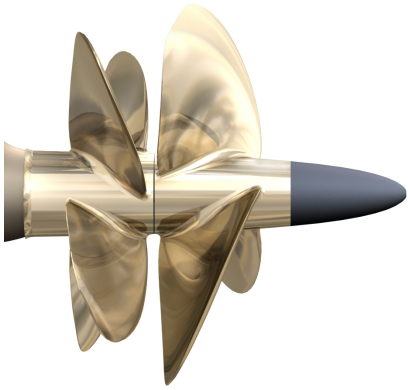

Figure 4.2: Single shaft CRP design [2].

Application of CRP is usually limited to torpedoes and high-speed outboard units of smaller sizes [29]. After an increased interest in CRP sets and their application during the late 1980s, examples of CRP can be seen fitted to a bulk carrier in 1988 and a very large crude carrier in 1993 [28].

Implementing CRP in ship design, introducing the secondary propeller, helps in reducing the load which would normally be exerted on the main propeller. The same amount of power needed to generate sufficient thrust and to propel the vessel is shared between the two propellers of the CRP set. Furthermore, part of the rotational energy, which would otherwise be transferred to the surrounding fluid, is now recovered by the aft propeller. As the propellers share the load exerted on them, the risk of cavitation along the blades of the propellers is also greatly reduced. The reduced risk of cavitation

results in longer service intervals and an overall increase in the life-cycle of the propellers. An important benefit of CRP sets, discussed in [30], is better uniformity of flow in downstream wake of the propeller set, resulting in lower noise signatures. Furthermore, if sets with equal and even number of blades are used, fluctuating thrust will be present. If the number of blades is odd, the fluctuation is smaller, but a sideways force will be present. Finally, the primary reason for the use of CRP is to remove torque from the system.

With recent developments in electromagnetic motors and electric propulsion systems, a renewed interest in CRP design and development has emerged. Design based on the classic coaxial dual-shaft design was developed, introducing the concept of podded CRP sets (Fig. 4.1). In this concept, the secondary (aft) propeller is fitted to a pod-mounted shaft. The main (fore) propeller is connected to a ships engine via a shaft, while the secondary propeller is mounted to an electric motor inside the pod. The pod carrying the secondary propeller may be fixed or can rotate repositioning the secondary propeller to help increase manoeuvrability [28].

Because of the rapid development of electric and hybrid propulsion systems, which was brought on by an increased need for the reduction in fuel consumption and emissions produced by large transport vessels, the concept of podded CRP becomes of great interest. Newer designs, which feature a podded CRP set, have the secondary propeller connected to an electromagnetic motor powered by electricity produced by the excess heat from the main engine [28]. Benefits of using two coaxial contra-rotating propellers with a podded aft propeller include reduction in torque exerted on the vehicle by the CRP set and an increase in efficiency resulting in a decrease in fuel consumption. When the design includes a rotatable pod the aft propeller may be used to aid in executing various manoeuvres and may even be used as a secondary electric propulsion system in case of main engine failure [28].

4.3. Previous Studies

Single propellers were used on most maritime vessels as the main system of propulsion for a long time and, as such, were the focus of a large number of studies focusing on different aspects of propeller design. Advancements in numerical simulations and CFD simulations allowed for a series of studies focusing on propeller characteristics and ship

manoeuvring simulations [31, 32, 33].

With the rising interest in CRP and their use for ship propulsion, a growing number of numerical and experimental studies focusing on CRP sets can be found. Some of the first experiments were performed using a scaled CRP model and focused on defining the open-water characteristics [34] and the effects of axial displacements of such sets [35]. More recent studies were performed by Miller in 1976 [36] and again in 1981 [37]. These experiments were aimed at determining the unsteady forces on a CRP set in uniform flow and are of great interest to the subject of this Thesis, as they were used for comparison with the data produced by CFD simulations run for the purpose of this thesis.

A number of numerical simulations dealing with CRP was performed by numerous authors, which will be outlined briefly. Hoshino [38] expanded experimental research on CRP model and used the experimental data to validate numerical simulations performed using Lifting Surface Theory. The same theory was used by Tsakonas et al. [39] and Yang et al. [40] to calculate the hydrodynamic coefficients of CRP. On the other hand, Ghassemi and Taherinasab [30] implemented the Boundary Element Method to model steady hydrodynamic performance of CRP, while Gu and Kinnas used a combination of FVM and the Vortex-Lattice Method. Use of CFD for investigation of CRP blade interaction and performance surfaced only recently with Wang and Xiong [41] using RANS modelling to determine the effects time-step size and turbulence on CRP performance and with Nouri et al. [42] using CFD for CRP optimisation.

4.4. Characteristics of CRP

This section is dedicated to describing how the performance of CRP is to be evaluated. Besides examining the pressure and velocity fields of propellers, it is common to define propeller open-water characteristics. Open-water characteristics of CRP sets are defined by calculating hydrodynamic performance coefficients for each propeller separately and for the whole set.

Another interesting phenomena examined as part of this thesis, are vortices. The Q-criterion is used as a method of vortex identification. It is used to define structures of different vorticity and examine the influence of propeller interaction in CRP sets on interacting vortices.

4.4.1. Hydrodynamic Coefficients

Hydrodynamic coefficients are calculated to determine the open-water characteristics of the CRP set. The calculated coefficients include the thrust coefficient K_T, the torque coefficient K_Q and propeller efficiency η. The aforementioned coefficients are calculated for each propeller and for the whole CRP set. If values for each of these coefficients are given in relation to the advance coefficient J, determined for different operating points, a diagram showing the open-water characteristics of the CRP set can be drawn.

Depending on the type of simulation used, two different types of hydrodynamic coefficients may be determined: steady coefficients may be expressed from data collected from both steady state and transient simulations, while the unsteady coefficients may be determined from transient data only.

It should be noted that the procedure for determining steady and unsteady CRP hydrodynamic coefficients was defined as to adhere to the procedure used by Miller [36, 37] in his experimental studies. This was done to allow for comparison between the experimental data acquired by Miller and the numerical data simulated for the purpose of this thesis.

Steady Coefficients

The propeller advance ratio J is a non-dimensional coefficient which defines the ratio of the free-stream fluid velocity compared to propeller rotation speed. It can be calculated by using the following expression:

$$J = \frac{U}{n\,D_f}\,, \tag{4.1}$$

where U defines the free-stream velocity of the fluid, n defines the rotational speed of the propeller and D_f is the propeller diameter. The advance ratio J for both propellers and the whole CRP set is calculated using the diameter of the fore (forward) propeller, D_f. By using the corresponding values of thrust for each propeller, thrust coefficients may be calculated using the following expressions:

$$K_{Tf} = \frac{T_f}{n^2 D_f^4 \rho}\,, \tag{4.2}$$

$$K_{Ta} = \frac{T_a}{n^2 D_a^4 \rho}\,. \tag{4.3}$$

Eq. 4.2 nad 4.3 produce values of aft/fore thrust coefficients for given values of thrust T, rotational speed n, water density ρ and the corresponding propeller diameter D_f, D_a. The same value of the propeller rotation speed n is used for both propellers as their movement is synchronised in both the experiments and simulations used in the thesis. By using the same assumptions as above and the corresponding values of torque, the propeller torque coefficients can be determined using:

$$K_{Qf} = \frac{Q_f}{n^2 D_f^5 \rho}\,, \tag{4.4}$$

$$K_{Qa} = \frac{Q_a}{n^2 D_a^5 \rho}\,. \tag{4.5}$$

The values of the torque and thrust coefficients are used to calculate propeller efficiency for the corresponding advance ratio J:

$$\eta_f = \frac{K_{Tf}}{K_{Qf}} \frac{J}{2\pi}\,, \tag{4.6}$$

$$\eta_a = \frac{K_{Ta}}{K_{Qa}} \frac{J}{2\pi}\,. \tag{4.7}$$

Once the steady thrust and torque coefficients are calculated for each of the two propellers forming the CRP set, the total hydrodynamic coefficients of the CRP set may be determined using:

$$K_T = K_{Tf} + K_{Ta}\,, \tag{4.8}$$

$$K_Q = K_{Qf} + K_{Qa}\,, \tag{4.9}$$

with the total set efficiency determined by the following expression:

$$\eta = \frac{K_T}{K_Q}\frac{J}{2\pi}\,. \tag{4.10}$$

Unsteady Coefficients

Time-varying data gathered from transient simulations is analysed as a part of this thesis. The values of unsteady thrust and torque are calculated in a way that makes them comparable to corresponding experimental values from studies performed by Miller [36, 37]. The Direct Fourier Transform (DFT) was used to transform the transient data and analyse the resulting amplitudes as functions of frequency. The amplitudes of unsteady torque and thrust at certain frequencies (or harmonics) were used to determine unsteady thrust and torque coefficients.
Values of unsteady thrust and torque may be presented as a sum of sine and cosine amplitudes for any harmonic N:

$$\widetilde{T}_N = T_{1,N}\cos(N\theta) + T_{2,N}\sin(N\theta)\,, \tag{4.11}$$

$$\widetilde{Q}_N = Q_{1,N}\cos(N\theta) + Q_{2,N}\sin(N\theta)\,. \tag{4.12}$$

Eq. 4.11 and 4.12 allow the unsteady coefficients for each propeller to be defined for a certain harmonic N as:

$$\widetilde{K}_{T,prop,N} = \frac{(T_{1,N}^2 + T_{2,N}^2)^{\frac{1}{2}}}{n^2 D^4 \rho}\,, \tag{4.13}$$

$$\widetilde{K}_{Q,prop,N} = \frac{(Q_{1,N}^2 + Q_{2,N}^2)^{\frac{1}{2}}}{n^2 D^5 \rho}\,. \tag{4.14}$$

The total coefficients of unsteady thrust and torque for the complete CRP set may be calculated from the following equations:

$$\widetilde{K}_{T,N} = \widetilde{K}_{Tf,N} + \widetilde{K}_{Ta,N}\,, \tag{4.15}$$

$$\widetilde{K}_{Q,N} = \widetilde{K}_{Qf,N} + \widetilde{K}_{Qa,N}\,. \tag{4.16}$$

4.4.2. Q-Criterion

An interesting aspect of turbomachinery CFD is the possibility of investigating vorticity of the flow. This becomes of special interest when dealing with multi-blade multi-rotor machines, such as the CRP set. Rotor interactions of the two propellers result in interesting vortex interaction.

The vortices in the flow-field around and after the propeller set shall be defined using the Q-criterion. Historically, one of the first three-dimensional vortex criteria, the Q-criterion was developed by Hunt, Wray and Moin in 1988 [43].
As shown in [44] the velocity gradient $\nabla\mathbf{u}$ of a three-dimensional velocity field $\mathbf{u}$ may be decomposed as follows:

$$\nabla\mathbf{u} = \underbrace{\mathbf{S}}_{\substack{\text{rate-of-strain}\\ \text{tensor}}} + \underbrace{\mathbf{\Omega}}_{\substack{\text{vortricity}\\ \text{tensor}}} . \tag{4.17}$$

Eq. 4.17 represents the decomposition of the velocity gradient into the rate-of-strain tensor $\mathbf{S}$ and the vorticity tensor $\mathbf{\Omega}$, both given below:

$$\mathbf{S} = \frac{1}{2}\left[\nabla\mathbf{u} + (\nabla\mathbf{u})^T\right] , \tag{4.18}$$

$$\mathbf{\Omega} = \frac{1}{2}\left[\nabla\mathbf{u} - (\nabla\mathbf{u})^T\right] . \tag{4.19}$$

The Q-criterion defines a vortex as a region in space where by the Euclidean norm of the vorticity tensor dominates over the Euclidean norm of the rate-of-strain tensor. Thus described as:

$$Q = \frac{1}{2}\left[\,|\mathbf{\Omega}|^2 - |\mathbf{S}|^2\,\right] > 0\,. \tag{4.20}$$

4.5. Closure

The concluded chapter gave an examination of the design of CRP, its implementation and development. The most important benefits of CRP implementation were discussed, as well as some of the disadvantages of older designs. Moreover, an overview

of experimental and numerical studies was given. The basic equations used to describe the characteristics of CRP in terms of open-water characteristics and vorticity were also presented.

The next chapter deals with geometries used for CFD simulations of CRP and the resulting computational domains. An overview of patches, regions, domain interfaces and the necessary boundary conditions is given as an introduction to the numerical simulations made using the CRP computational model.

5 Geometry and Computational Domain

5.1. Introduction

The previous chapter dealt with CRP sets in general, their design, application and improvements over single-propeller designs. Moreover, an overview of previous experimental and numerical studies was given.

The forthcoming chapter deals with the CRP geometry and the resulting computational domain. An overview of domain characteristics of both the whole geometry and quarter geometry meshes is presented. An description of domain boundary patches and interfaces is given with an overview of boundary conditions imposed on the patches.

5.2. Model Geometry

The geometry used as a starting point for creating a computational domain (mesh) is the model used in experimental studies performed by Miller [36, 37]. The propeller set geometry closely mimics the CRP set described by Miller, which is a necessary condition for the numerical results to be comparable to experimental data.

The CRP set consists of two four-bladed propellers mounted on hubs with co-linear rotational axes. The two propellers are mounted as to face one another and to rotate in opposite directions at identical rotational speed. The specifications defining the individual propellers are given in Table 5.1.

Table 5.1: Propeller geometry specification.

Propeller type	**3686**	**3687A**
Position in set	FORE	AFT
Blades	4	4
Diameter [m]	0.2991	0.3052
Rotation	CW	CCW
Expanded area ratio	0.303	0.324
Section Meanline	NACA $a = 0.8$	NACA $a = 0.8$
Thickness Distribution	NACA 66	NACA 66

The model is defined in such a way that the x-axis of the global coordinate system corresponds to the axial direction of water flow. Thus, defining the rotation of the front (fore) propeller (type 3686) as clockwise (CW) in regard to the x-axis of the coordinate system. On the other hand, the back (aft) propeller (type 3687A) rotates in the counter-clockwise direction (CCW).

Based on propeller specifications from Table 5.1, two geometries are derived for use in CFD simulations: a full geometry and a quarter geometry. The full geometry model uses the whole propeller hub with all four blades for each of the two propellers in the CRP set (Fig. 5.1-left). On the other hand, the quarter geometry model is created by using only a quarter of the propeller hub and only one of the four blades of each propeller with appropriate use of cyclic conditions (Fig. 5.1-right).

Creating a computational domain based on a quarter geometry instead of using a domain based on the whole propeller geometry results in minimised computational costs. This becomes of great importance when running transient simulations as it reduces the total computation time needed for the simulation to converge. A comparison between the two geometries is shown in Fig. 5.2 by an overlay of the quarter CRP geometry on top of the full geometry. Use of the quarter CRP geometry requires the assumption of periodicity of the whole geometry and the connected phenomena.

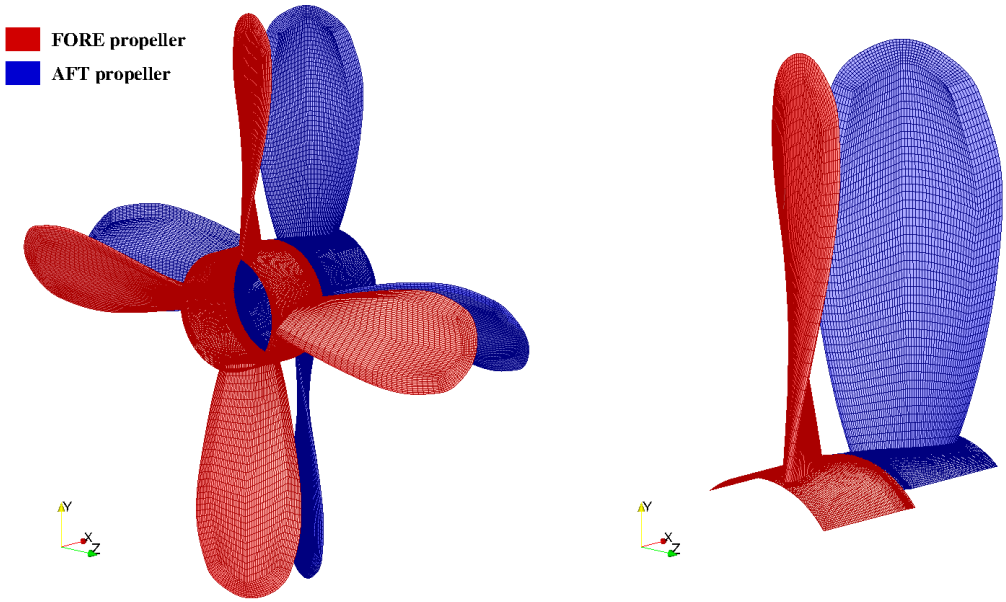

Figure 5.1: Whole (left) and quarter (right) propeller geometry.

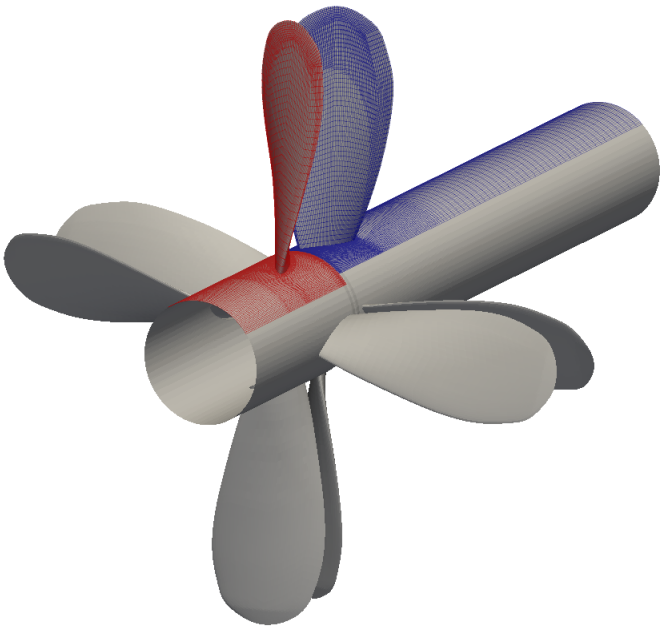

Figure 5.2: Overlay of the quarter over the whole geometry.

5.3. Computational Domain

Two geometries of the CRP set were used to create two domains, a quarter and a full geometry domain, that are used in CFD simulations of the CRP using `foam-extend`. The different nature of the domains in question requires different interface and boundary conditions to be applied.

The use of domain interfaces is necessary as the computational domain is constructed from three separate domains, thus resulting in the computational mesh having three mesh regions. The regions in question are: the region around the front propeller (FORE propeller), the region around the back propeller (AFT propeller) and the region representing the far field (FarField) which surrounds the two propeller regions. The main reason for dividing the computational mesh into the aforementioned mesh regions is the ability to define different zones, connected by appropriate interfaces, for each region. Different zones and interfaces can then be used for defining MRF and `dynamicMesh` zones used for resolving movement in the simulations.

5.3.1. Full Propeller Domain

The full propeller computational domain (mesh) is created using the full CRP geometry shown in Fig. 5.1. The mesh is divided into three mesh regions separated by appropriate internal and boundary patches. An overview of different mesh region and their specifics in given in Table 5.2.

Table 5.2: Overview of full geometry mesh regions.

Mesh Region	**Number of Cells**	**Type**	**NOTE**
FarField	1117248	hexahedra	No moving cell zones.
FORE propeller	1316400	hexahedra	MRF/DynamicMesh zone: Prop1
AFT propeller	2778144	hexahedra	MRF/DynamicMesh zone: Prop2
Total	**5211792**	hexahedra	

The largest mesh region is the one defining the far field surrounding the CRP set (designated as *FarField*). This region is bounded by the *inlet*, *outlet* and *outerWall* boundary patches (Fig. 5.3). Non-rotating hubs suspending the propellers in water are denoted by the *hubMain* patch name. Furthermore, the boundaries between this region and the two propeller regions are defined by internal patches. Such patches exist inside

the computational domain separating different regions, unlike boundary patches that separate the domain from the "outside world".

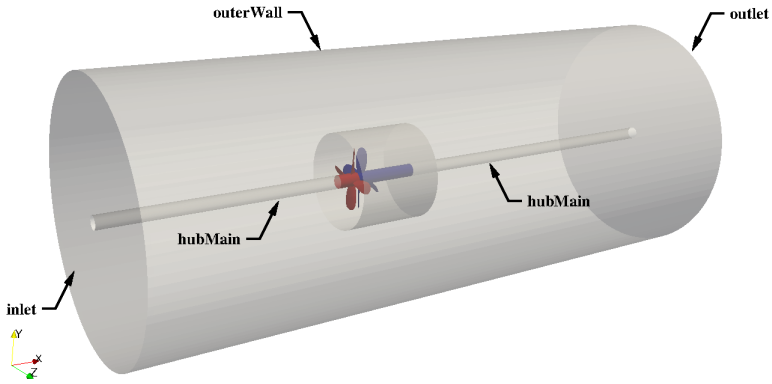

Figure 5.3: Whole geometry: FarField patch identification.

Internal patches of the *FarField* mesh region are shown in Figure 5.4 and are used as interfaces enabling communication between propeller mesh regions.

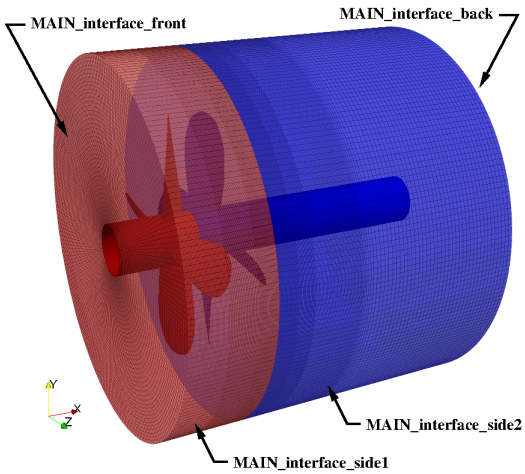

Figure 5.4: Whole geometry: FarField interfaces near propeller region.

All interfaces belonging to the *FarField* region are denoted by including the prefix *"MAIN"* in their name. Similarly, all patches (interfaces) belonging to the *FORE pro-*

peller region have the prefix *"FORE"* and the ones belonging to the *AFT propeller* region have the prefix *"AFT"* in their names.

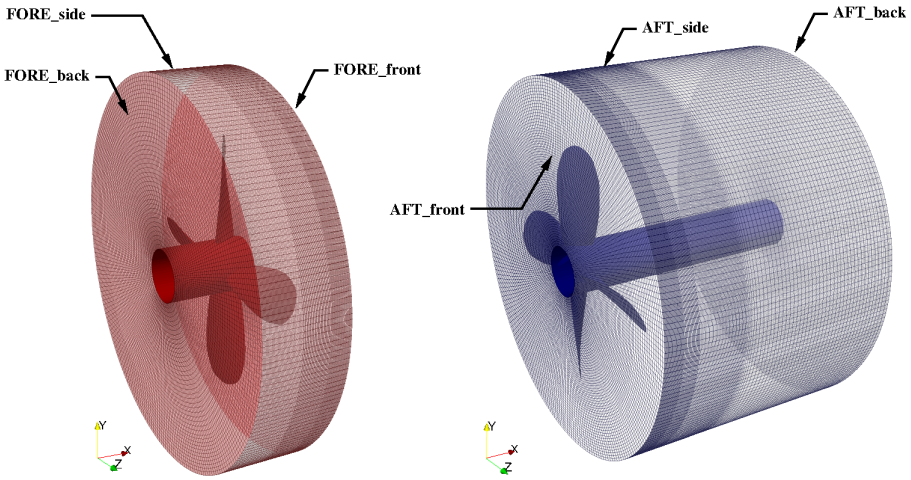

Figure 5.5: Whole geometry: Propeller region interfaces.

Figure 5.5 examines the two propeller regions and the accompanying patches. Each of the cylindrical propeller regions consists of a front, back and a side patch. To establish the communication using one of the interfaces described in Ch. 3., patch pairs are established as follows: side patches of the propeller regions are paired with matching side patches of the far field region, front patches of the two propellers are matched as a pair, the back patch of the FORE propeller is matched with the front patch of the far field region and the back patch of the AFT propeller is matched with the back patch of the far field region.

5.3.2. Quarter Propeller Domain

The quarter propeller domain is created from the quarter CRP geometry. The same as with full domain, the quarter domain is divided into three regions following the same terminology (*FarField, FORE propeller and AFT propeller*). An overview of full geometry mesh regions is given in Table 5.3.

Comparing mesh region data for the quarter geometry domain shown in Tbl. 5.3 to same data for the whole geometry in Tbl. 5.2, a considerable decrease in cell count can be seen for the *FORE* and *AFT* regions of the quarter mesh, resulting in a smaller number

of cells for the total computational domain. This was achieved by reducing propeller regions to a quarter of the original, which was possible by using only one propeller blade and quarter of the hub geometry. On the other hand, the cell count for the *FarField* is the same as for the whole domain, as this region is used in its entirety for both the quarter and the whole propeller domains.

Table 5.3: Overview of quarter geometry mesh regions.

Mesh Region	**Number of Cells**	**Type**	**NOTE**
FarField	1117248	hexahedra	No moving cell zones.
FORE propeller	329100	hexahedra	MRF/DynamicMesh zone: Prop1
AFT propeller	694536	hexahedra	MRF/DynamicMesh zone: Prop2
Total	**5211792**	hexahedra	

Figure 5.6 shows how the quarter propeller regions connect to the *FarField* region. As this mesh region is the same as the one used for the whole propeller domain, the boundary patches (*inlet, outlet, outerWall, hubMain*) and internal patches defining the region have not changed.

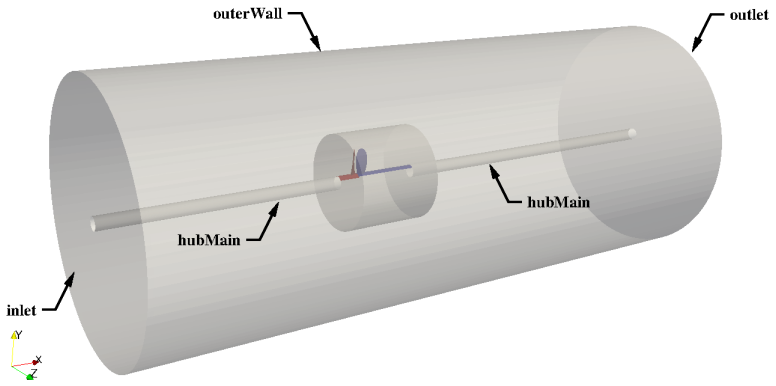

Figure 5.6: Quarter geometry: FarField patch identification.

The geometric definition of internal patches belonging to the *FarField* region shown in Fig. 5.7 have not changed when compared to the whole geometry mesh. Nevertheless, they are paired with patches bounding the quarter propeller regions, which is why they require different patch (interface) definition and a different set of boundary conditions.

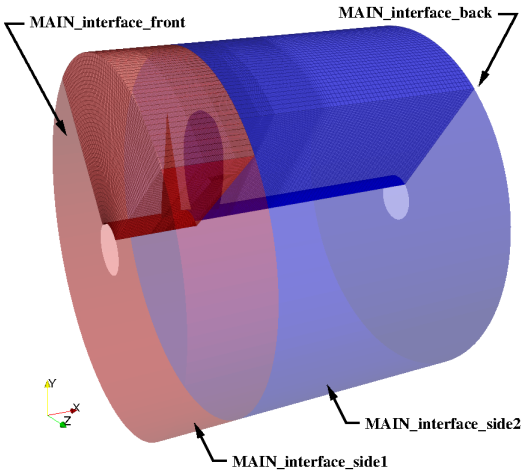

Figure 5.7: Quarter geometry: FarField interfaces near propeller region.

Figure 5.8 shows the quarter propeller mesh regions with corresponding boundary patches. The positions of the front, back and side patches is analogous to those of their whole geometry counterparts, but they are reduced to a quarter of their original geometry. New patches defining the boundaries where the quarter regions would expand into the full geometry region are present (*cyclic* and *cyclic_shadow*). These patches bound the cyclically periodic boundary of the propeller regions and are defined as `cyclicGgi` interfaces.

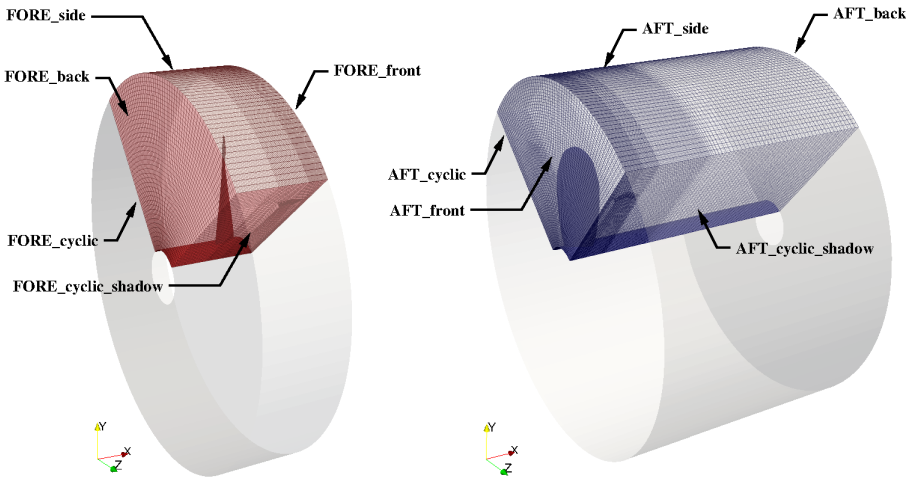

Figure 5.8: Quarter geometry: Propeller region interfaces.

5.4. Boundary Definition

All of the patches described in previous sections need to be defined in the `boundary` file used by `foam-extend` to define boundary patch types. By defining the patches inside the aforementioned file, they are given a certain type dictating how they are identified when running the simulation. This is especially important when dealing with internal patches which are defined as interfaces.

Varying combinations of interfaces were used depending on mesh and geometry (quarter or whole) and whether the simulation was setup as steady-state or transient. A generic patch type was applied to the *inlet* and *outlet* patches, whereas the `wall` type was applied to all propeller and hub parts. For quarter geometry cases, the interface used for the internal patches is switched from `ggi` to `overlapGgi` to enable communication between the full domain of the far field and the quarter domains of the propellers. Additionally, quarter cases use the `cyclicGgi` interface for cyclically periodic boundary patches. A series of steady-state simulations was carried out using the `mixingPlane` interface, replacing the `ggi` interfaces. This was done for steady-state cases only, as the averaging performed by the `mixingPlane` interfaces should not be applied to transient data. An overview of patches with matching patch types and corresponding pairs is given tabularly. Three tables are presented (Tbl. 5.4, 5.5 and 5.6) systematising patches according to mesh region allocation.

Table 5.4: Farfield boundary patches.

FarField				
No.	**Patch Name**	**Patch Type**		**Pair No.**
		steady-state	**transient**	
01	inlet	`patch`	`patch`	n/a
02	outlet	`patch`	`patch`	n/a
03	outerWall	`wall`	`wall`	n/a
04	hubMain	`wall`	`wall`	n/a
05	MAIN_interface_front	`ggi / overlapGgi* / mixingPlane°`	`ggi / overlapGgi*`	**13**
06	MAIN_interface_side1	`ggi / overlapGgi* / mixingPlane°`	`ggi / overlapGgi*`	**12**
07	MAIN_interface_side2	`ggi / overlapGgi* / mixingPlane°`	`ggi / overlapGgi*`	**19**
08	MAIN_interface_back	`ggi / overlapGgi* / mixingPlane°`	`ggi / overlapGgi*`	**20**
* quarter-case only, ° used for mixingPlane test cases				

Table 5.5: FORE propeller boundary patches.

FORE propeller				
No.	**Patch Name**	**Patch Type**		**Pair No.**
		steady-state	**transient**	
09	FORE_prop	`wall`	`wall`	n/a
10	FORE_hub	`wall`	`wall`	n/a
11	FORE_interface_front	`ggi / overlapGgi* / mixingPlane°`	`ggi / overlapGgi*`	**18**
12	FORE_interface_side	`ggi / overlapGgi* / mixingPlane°`	`ggi / overlapGgi*`	**06**
13	FORE_interface_back	`ggi / overlapGgi* / mixingPlane°`	`ggi / overlapGgi*`	**05**
14	FORE_cyclic*	`cyclicGgi`	`cyclicGgi`	**15**
15	FORE_cyclic_shadow*	`cyclicGgi`	`cyclicGgi`	**14**
* quarter-case only, ° used for mixingPlane test cases				

Table 5.6: AFT propeller boundary patches.

AFT propeller				
No.	**Patch Name**	**Patch Type**		**Pair No.**
		steady-state	**transient**	
16	AFT_prop	`wall`	`wall`	n/a
17	AFT_hub	`wall`	`wall`	n/a
18	AFT_interface_front	`ggi / overlapGgi* / mixingPlane°`	`ggi / overlapGgi*`	**11**
19	AFT_interface_side	`ggi / overlapGgi* / mixingPlane°`	`ggi / overlapGgi*`	**07**
20	AFT_interface_back	`ggi / overlapGgi* / mixingPlane°`	`ggi / overlapGgi*`	**08**
21	AFT_cyclic*	`cyclicGgi`	`cyclicGgi`	**22**
22	AFT_cyclic_shadow*	`cyclicGgi`	`cyclicGgi`	**21**
* quarter-case only, ° used for mixingPlane test cases				

While the quarter cases require the use of both `cyclicGgi` and `overlapGgi` interfaces to resolve cyclically periodic and non-overlapping patch communication brought on by the use of a quarter domain, the whole cases allowed for the use of the basic `ggi`

interface. As all of the aforementioned interfaces require specific entries in the `boundary` file, examples on how each interface type is set-up are offered in Appendix A.

5.5. Boundary Conditions

Boundary conditions (b.c.) must be applied to various patches of the computational domain to define conditions which make the system of equations numerically well posed and solvable.

The *Dirichlet* (`fixedValue`) b.c. is applied to the *inlet* patch for velocity $\mathbf{u}$ with a reference value U_x. This value is equivalent to different axial velocities of flow for each simulated operating point. The same b.c. is applied for k and ω, but with different reference values. The pressure p at the *inlet* patch is defined by the *Neumann* boundary condition (`zeroGradient`). The values of $\mathbf{u}, k$ and ω at the *outlet* patch are all defined using the `inletOutlet` b.c. derived from a combination of the *Dirichlet* and *Neumann* boundary conditions. The *Dirichlet* b.c. with $p_{ref} = 0$ is applied to the pressure p at the *outlet* patch for steady-state and transient simulations.

All patches defined by the `wall` patch type (*outerWall, hubMain, FORE_prop, FORE_hub, AFT_prop, AFT_hub*) are defined by the *Dirichlet* b.c. for $\mathbf{u}$ with $\mathbf{u}_{ref} = 0$ and with the *Neumann* b.c. for p. Values for k and ω at the wall are defined by using the appropriate wall functions, i.e. the `omegaWallFunction` for ω and the `kqRWallFunction` for k.

The remaining patches are defined as interfaces and were set-up in the `boundary` file. The boundary conditions for these patches correspond to the interface type used. The choice of interface type depends on the type of simulation and geometry used.

An overview of all boundary patches and the given boundary conditions is given in the following three tables, grouped by affiliation to mesh regions:

Table 5.7: Overview of Farfield propeller boundary conditions.

FARFIELD Boundary Conditions (B.C)									
No.	**Patch Name**	**Steady-state B.C.**				**Transient B.C.**			
		U [m/s]	**p** [m^2/s^2]	**k** [m^2/s^2]	ω [1/s]	**U** [m/s]	**p** [m^2/s^2]	**k** [m^2/s^2]	ω [1/s]
01	inlet	fixedValue; uniform (U_x 0 0);	zeroGradient;	fixedValue; uniform k_{ref};	fixedValue; uniform ω_{ref};	fixedValue; uniform (U_x 0 0);	zeroGradient;	fixedValue; uniform k_{ref};	fixedValue; uniform ω_{ref};
02	outlet	inletOutlet; uniform (0 0 0); uniform (U_x 0 0);	fixedValue; uniform 0;	inletOutlet; uniform k_x; uniform k_x;	inletOutlet; uniformω_{ref}; uniform ω_{ref};	inletOutlet; uniform (0 0 0); uniform (U_x 0 0);	fixedValue; uniform 0;	inletOutlet; uniform k_x; uniform k_x;	inletOutlet; uniformω_{ref}; uniform ω_{ref};
03	outerWall	fixedValue; uniform (0 0 0);	zeroGradient;	kqRWallFunction;	omegaWallFunction;	fixedValue; uniform (0 0 0);	zeroGradient;	kqRWallFunction;	omegaWallFunction;
04	hubMain	fixedValue; uniform (0 0 0);	zeroGradient;	kqRWallFunction;	omegaWallFunction;	fixedValue; uniform (0 0 0);	zeroGradient;	kqRWallFunction;	omegaWallFunction;
05	MAIN_interface_front	ggi / overlapGgi*;	ggi / overlapGgi*;	ggi / overlapGgi*;	ggi / overlapGgi*;	ggi / overlapGgi*;	ggi / overlapGgi*;	ggi / overlapGgi*;	ggi / overlapGgi*;
06	MAIN_interface_side1	ggi / overlapGgi*;	ggi / overlapGgi*;	ggi / overlapGgi*;	ggi / overlapGgi*;	ggi / overlapGgi*;	ggi / overlapGgi*;	ggi / overlapGgi*;	ggi / overlapGgi*;
07	MAIN_interface_side2	ggi / overlapGgi*;	ggi / overlapGgi*;	ggi / overlapGgi*;	ggi / overlapGgi*;	ggi / overlapGgi*;	ggi / overlapGgi*;	ggi / overlapGgi*;	ggi / overlapGgi*;
08	MAIN_interface_back	ggi / overlapGgi*;	ggi / overlapGgi*;	ggi / overlapGgi*;	ggi / overlapGgi*;	ggi / overlapGgi*;	ggi / overlapGgi*;	ggi / overlapGgi*;	ggi / overlapGgi*;

* quarter-case only

NOTE: Ggi and overlapGgi replaced by mixingPlane for mixingPlane validation cases.

Table 5.8: Overview of FORE propeller boundary conditions.

FORE propeller Boundary Conditions (B.C.)									
No.	**Patch Name**	**Steady-state B.C.**				**Transient B.C.**			
		U [m/s]	**p** [m^2/s^2]	**k** [m^2/s^2]	ω [1/s]	**U** [m/s]	**p** [m^2/s^2]	**k** [m^2/s^2]	ω [1/s]
09	FORE_prop	`fixedValue; uniform (0 0 0);`	`zeroGradient;`	`kqRWallFunction;`	`omegaWallFunction;`	`movingWallVelocity; uniform (0 0 0);`	`zeroGradient;`	`kqRWallFunction;`	`omegaWallFunction;`
10	FORE_hub	`fixedValue; uniform (0 0 0);`	`zeroGradient;`	`kqRWallFunction;`	`omegaWallFunction;`	`fixedValue; uniform (0 0 0);`	`zeroGradient;`	`kqRWallFunction;`	`omegaWallFunction;`
11	FORE_interface_front	`ggi / overlapGgi*;`	`ggi / overlapGgi*;`	`ggi / overlapGgi*;`	`ggi / overlapGgi*;`	`ggi / overlapGgi*;`	`ggi / overlapGgi*;`	`ggi / overlapGgi*;`	`ggi / overlapGgi*;`
12	FORE_interface_side	`ggi / overlapGgi*;`	`ggi / overlapGgi*;`	`ggi / overlapGgi*;`	`ggi / overlapGgi*;`	`ggi / overlapGgi*;`	`ggi / overlapGgi*;`	`ggi / overlapGgi*;`	`ggi / overlapGgi*;`
13	FORE_interface_back	`ggi / overlapGgi*;`	`ggi / overlapGgi*;`	`ggi / overlapGgi*;`	`ggi / overlapGgi*;`	`ggi / overlapGgi*;`	`ggi / overlapGgi*;`	`ggi / overlapGgi*;`	`ggi / overlapGgi*;`
14	FORE_cyclic*	`cyclicGgi;`	`cyclicGgi;`	`cyclicGgi;`	`cyclicGgi;`	`cyclicGgi;`	`cyclicGgi;`	`cyclicGgi;`	`cyclicGgi;`
15	FORE_cyclic_shadow*	`cyclicGgi;`	`cyclicGgi;`	`cyclicGgi;`	`cyclicGgi;`	`cyclicGgi;`	`cyclicGgi;`	`cyclicGgi;`	`cyclicGgi;`

* quarter-case only

NOTE: Ggi and overlapGgi replaced by mixingPlane for mixingPlane validation cases.

Table 5.9: Overview of AFT propeller boundary conditions.

AFT propeller Boundary Conditions (B.C.)									
No.	**Patch Name**	**Stead-state B.C.**				**Transient B.C.**			
		U [m/s]	**p**	**k**	**Ω**	**U**	**p**	**k**	**Ω**
16	AFT_prop	`fixedValue; uniform (0 0 0);`	`zeroGradient;`	`kqRWallFunction;`	`omegaWallFunction;`	`movingWallVelocity; uniform (0 0 0);`	`zeroGradient;`	`kqRWallFunction;`	`omegaWallFunction;`
17	AFT_hub	`fixedValue; uniform (0 0 0);`	`zeroGradient;`	`kqRWallFunction;`	`omegaWallFunction;`	`fixedValue; uniform (0 0 0);`	`zeroGradient;`	`kqRWallFunction;`	`omegaWallFunction;`
18	AFT_interface_front	`ggi / overlapGgi*;`	`ggi / overlapGgi*;`	`ggi / overlapGgi*;`	`ggi / overlapGgi*;`	`ggi / overlapGgi*;`	`ggi / overlapGgi*;`	`ggi / overlapGgi*;`	`ggi / overlapGgi*;`
19	AFT_interface_side	`ggi / overlapGgi*;`	`ggi / overlapGgi*;`	`ggi / overlapGgi*;`	`ggi / overlapGgi*;`	`ggi / overlapGgi*;`	`ggi / overlapGgi*;`	`ggi / overlapGgi*;`	`ggi / overlapGgi*;`
20	AFT_interface_back	`ggi / overlapGgi*;`	`ggi / overlapGgi*;`	`ggi / overlapGgi*;`	`ggi / overlapGgi*;`	`ggi / overlapGgi*;`	`ggi / overlapGgi*;`	`ggi / overlapGgi*;`	`ggi / overlapGgi*;`
21	AFT_cyclic*	`cyclicGgi;`	`cyclicGgi;`	`cyclicGgi;`	`cyclicGgi;`	`cyclicGgi;`	`cyclicGgi;`	`cyclicGgi;`	`cyclicGgi;`
22	AFT_cyclic_shadow*	`cyclicGgi;`	`cyclicGgi;`	`cyclicGgi;`	`cyclicGgi;`	`cyclicGgi;`	`cyclicGgi;`	`cyclicGgi;`	`cyclicGgi;`

* quarter-case only

NOTE: Ggi and overlapGgi replaced by mixingPlane for mixingPlane validation cases.

5.6. Closure

This chapter introduced the two geometries used as basis for CRP simulations: the quarter and the whole (full) geometry. The resulting computational domains were discussed and the regions which form the domains analysed. An overview of boundary patches and interface was given. The boundary conditions necessary for running the CFD simulations of CRP were defined and discussed.

The next chapter presents the results of various numerical simulations of the CRP set made using `foam-extend`. A comparison of quarter and whole computational domains is presented as verification of the quarter domain. The data acquired from transient and steady-state simulations is assessed and compared to available experimental data.

6 Results

6.1. Introduction

The previous chapter described the full propeller and quarter propeller geometries, which were the basis for the two CRP computational domains used in numerical simulations. An overview of various mesh regions forming the computational domains was given with a detailed overview of interface and patch types used. Boundary conditions applied to patches for simulations using different approaches to interface and domain handling were given tabularly.

This chapter presents the data acquired from a series of numerical simulations conducted on both the quarter and full CRP domains. Both steady-state and transient simulation results are offered, taking notice of how the use of different interfaces effects the resulting data.

The results are presented in form of graphical representations of pressure, velocity and other significant flow fields, with an analysis of open-water characteristics using hydrodynamic coefficients.

6.2. Full CRP Geometry

Results presented in this section are of simulations performed using the full CRP geometry and the resulting domain. Rotating motion of the propellers was handled by employing the MRF method with two rotational zones, one for each propeller of the CRP set.

The use of MRF for modelling of rotational zones resulted demanded separate mesh regions in the domain, thus requiring `ggi` interfaces to enable patch communication. The interface were set-up as presented in Chapter 5.

The rotational speed for both propellers was set as at a constant value of 12 rps with the propeller rotation modelled as synchronous to match the conditions of the experiments used as reference [36, 37].

6.2.1. Steady-State Simulation, J = 0.5

A series of full CRP geometry steady-state simulations using the MRF method was performed for different operating points defined by the propeller advance coefficient J. The results presented in continuation are those of an arbitrary CRP operating point denoted by advance coefficient $J = 0.5$.

Pressure Field

The graphical representation of the pressure field is given by values of kinematic pressure, i.e. the value of pressure divided by fluid density ρ. Figure 6.1 shows the pressure field around the propeller set in the $z = const.$ plane and direction of fluid flow corresponding to the x+ axis. The occurrence of low-pressure and high-pressure areas along the propeller blades, attributed to propeller rotation, can be seen clearly. (The pressure field for the quarter CRP simulation is given in Fig. 6.13.)

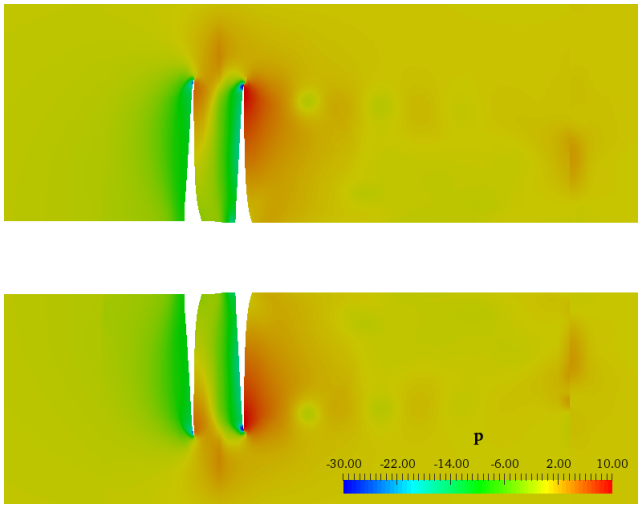

Figure 6.1: Full CRP: Pressure field in $z = const.$ plane.

The low and high-pressure areas can further examined in Fig. 6.2, which show mid-propeller slices for the FORE (Fig. 6.2-left) and AFT (Fig. 6.2-right) propeller. The slightly larger high and low-pressure regions near the AFT propeller seen in the $z = const.$ plane (Fig. 6.1) become more apparent in mid-propeller slices. Higher values of pressure are concentrated near the blade tips of the FORE propeller, with the lower pressure regions spread along the suction side of the blades.

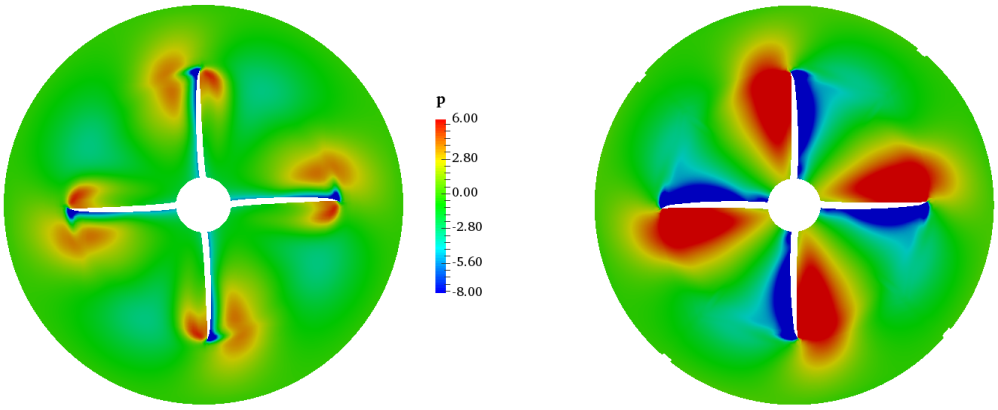

Figure 6.2: Full CRP: Mid-propeller slice.

Focusing on the AFT propeller shown in Fig. 6.2-right, larger areas of high and low pressure may be noticed. Such an occurrence may be attributed to propeller interaction, i.e. the effects of the FORE propeller wake on the AFT propeller.

Figures 6.3 and 6.4 show the pressure distribution along the propeller blades. The values of pressure along the front (pressure) side of the FORE propeller (Fig. 6.3-left) show the high pressure areas concentrated along the leading edge of each blade. The low-pressure areas seen on the suction side (Fig. 6.3-right) of the FORE propeller following the same leading edge. Pressure distribution on the pressure side (Fig. 6.4-left) of the AFT propeller is similar to that of the FORE propeller, yet reaching slightly higher values from blade tip to root. On the other hand, the suction side (Fig. 6.4-right) of the AFT propeller differs to that of the FORE propeller due to propeller interaction. As a result, low-pressure areas occur near the tip and root, with another low pressure area in the middle of the blade face.

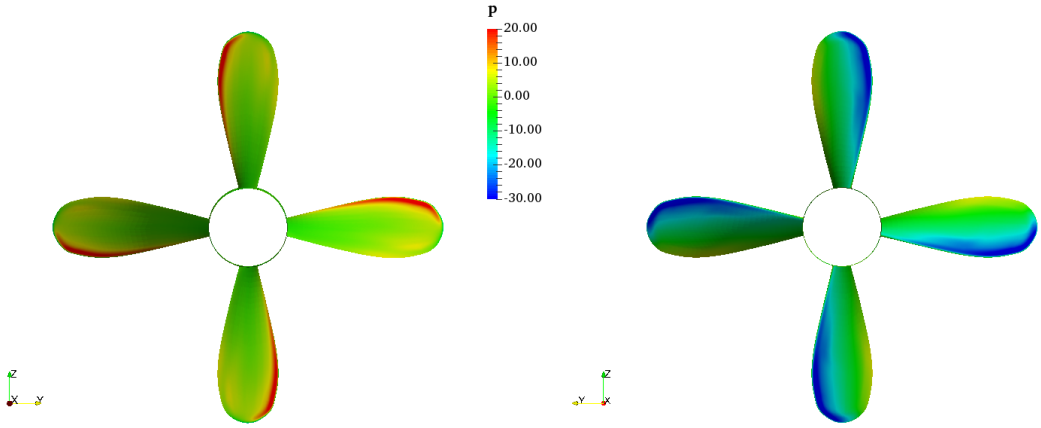

Figure 6.3: Full CRP: Pressure (left) and suction (right) side of FORE propeller.

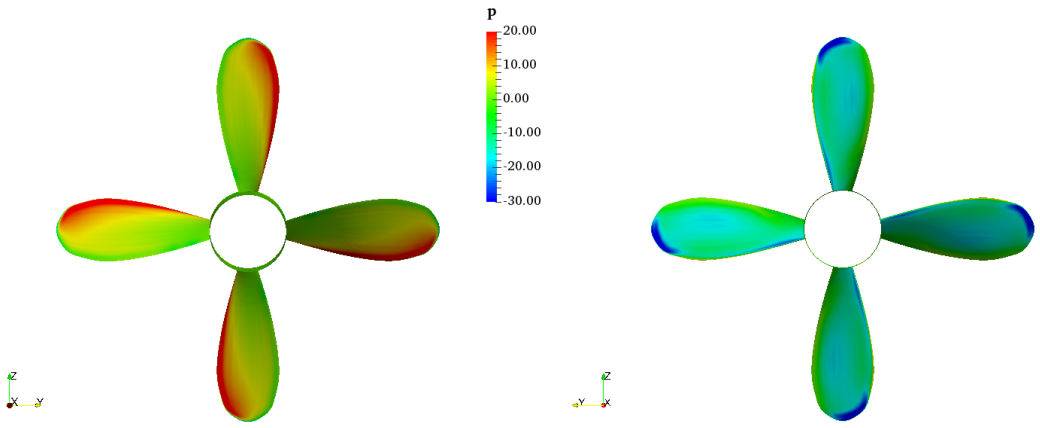

Figure 6.4: Full CRP: Pressure (left) and suction (right) side of AFT propeller.

Velocity Field

A graphical representation of the velocity field around the propeller set is shown below. Figure 6.5 depicts the axial velocity field in the $z = const.$ plane. The velocity field is presented as a ratio of the axial velocity U_x and the inlet velocity U_i, which depends on the operating point. For $J = 0.5$ the corresponding inlet velocity equals $U_i = 1.8312\,\mathrm{m/s}$. The highest values of axial velocity may be seen along the blades of the AFT propeller and wake of the CRP set. (Equivalent quarter CRP simulation data is given in Fig. 6.16.)

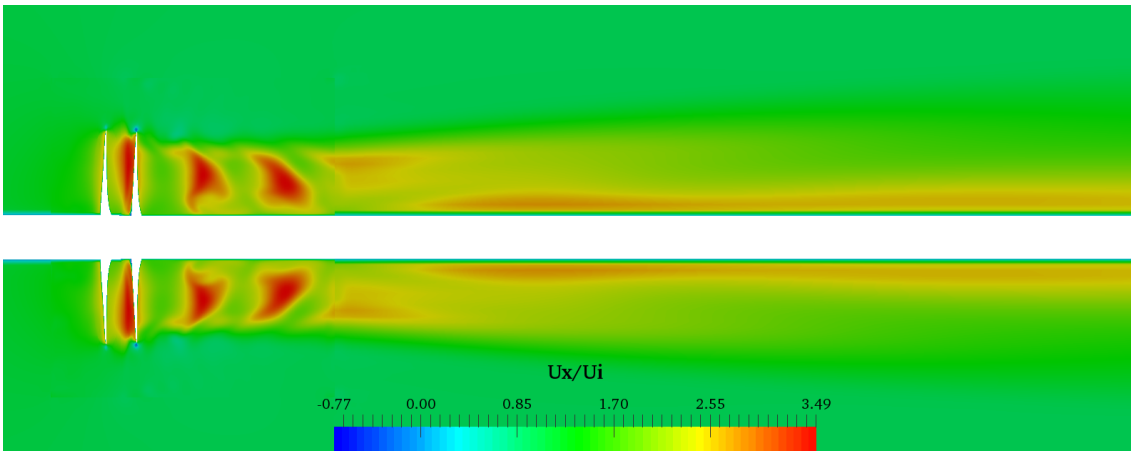

Figure 6.5: Full CRP: Velocity field in $z = const.$ plane.

Propeller interaction can be studied further by assessing the axial velocity in $x = const.$ planes positioned behind each of the propellers. Both cutting-planes are positioned at the same distance behind the corresponding propeller. The velocity field behind the FORE propeller (Fig. 6.5-left) peaks at U_x/U_i values of around 3 m/s, while the same values at an axial slice behind the AFT propeller rise to about 4 m/s.

Higher values of the axial velocity after the second propeller may be attributed to the contra-rotating motion of the AFT propeller. The second propeller of the CRP set "rectifies" the flow, reducing the tangential component of the velocity and increasing axial velocity. (Equivalent quarter CRP simulation data is given in Fig. 6.17.)

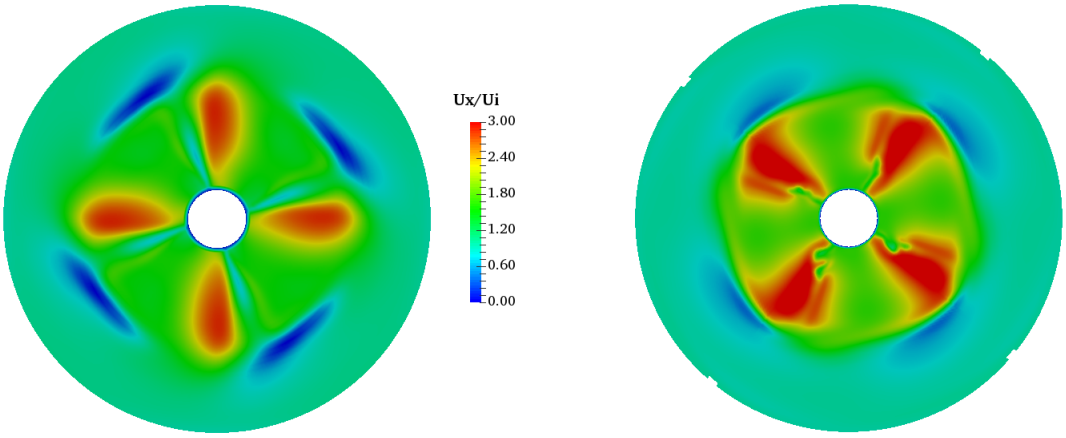

Figure 6.6: Full CRP: Velocity field at $x/R = 0$ and $x/R = 0.334$.

Turbulence and Vorticity

Turbulent kinetic energy k (TKE) was chosen as a value indicative of the occurrence of turbulence in the flow field. The values of TKE in the $z = const.$ plane are presented in Fig. 6.7, showing higher values of TKE near the blades of the AFT propeller. (Equivalent quarter CRP simulation data is given in Fig. 6.18.)

A closer examination of TKE distribution is given in Fig. 6.8. The high values of TKE are concentrated in near-tip regions on the suction side of the AFT propeller. The highest TKE values originate at the leading edge of the AFT propeller, where the high pressure of the pressure side abruptly changes to the low pressure of the suction side.

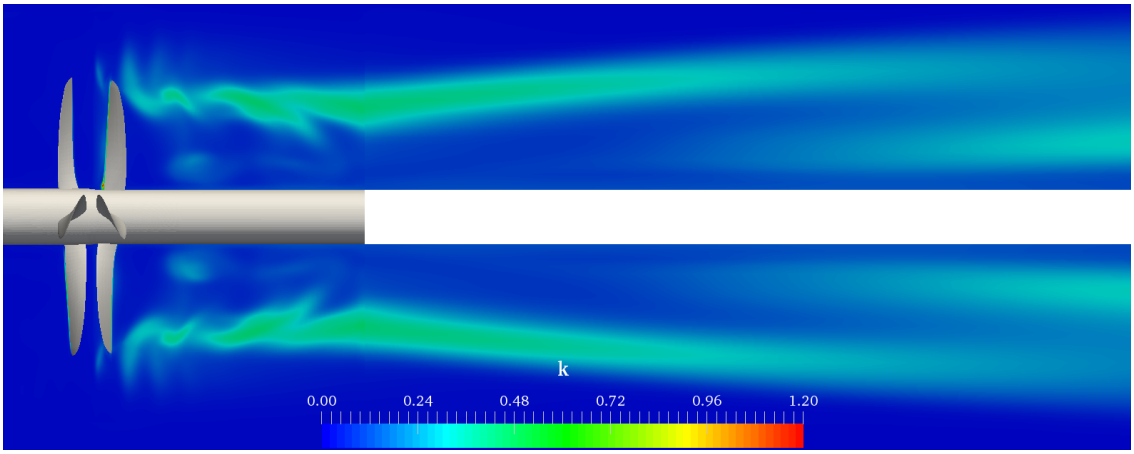

Figure 6.7: Full CRP: TKE in $z = const.$ plane.

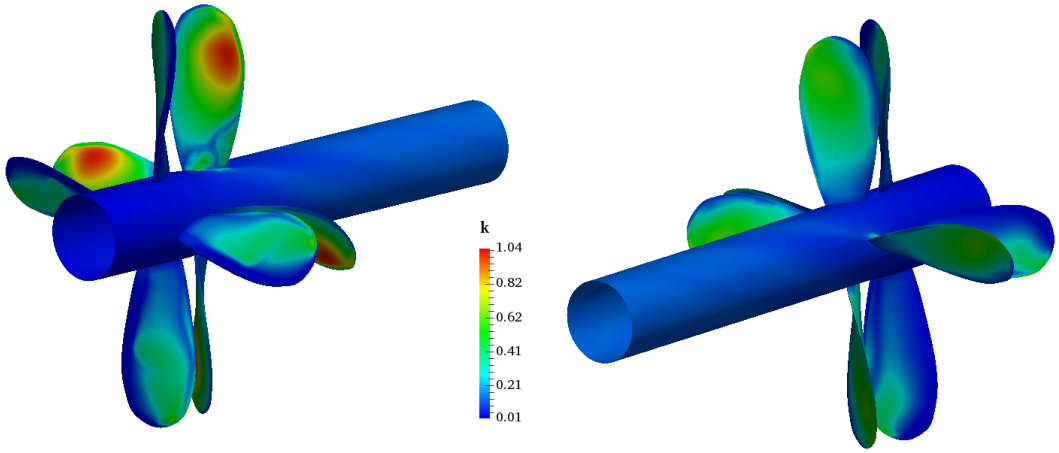

Figure 6.8: Full CRP: Distribution of TKE on propeller blades.

The Q-criterion was used as a measure of vorticity. Q was described in subsection 4.4.2. An arbitrary value of Q defines areas where vortices with an energy rate higher than the value set by Q can form. Q-contours depicting vortices with $Q > 3 \cdot 10^3$ and coloured by values of the velocity magnitude are shown in Fig. 6.9. Tip vortices are clearly seen and captured by the simulation, they disappear further downstream as they enter the far field mesh, which does not have sufficient resolution to preserve them. (Equivalent quarter CRP simulation data is given in Fig. 6.20.)

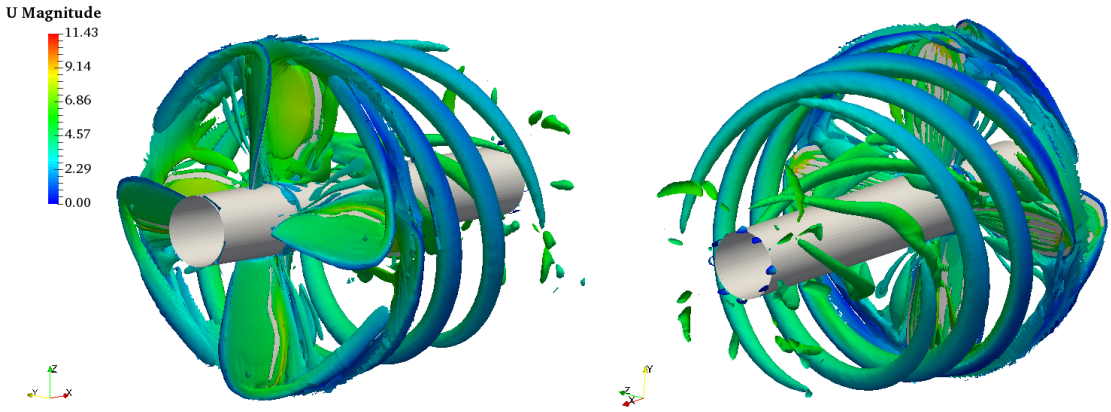

Figure 6.9: Full CRP: Vortices matching Q-criterion $Q > 3 \cdot 10^3$

6.2.2. Hydrodynamic Performance

Open-water characteristics are offered as a way of determining propeller performance throughout various operating points. A steady-state simulation using the MRF approach was carried out for each operating point determined by a different value of the advance coefficient J.

For each of the simulations, representing a single operating point of the CRP set, the resulting values of propeller thrust T and torque Q were used to determine the appropriate hydrodynamic performance coefficients. The equations and the supporting theory used to determine the hydrodynamic coefficients were introduced in subsection 4.4.1. Values of the coefficients describing the hydrodynamic performance were calculated separately for each propeller and summed to produce the total values of the set. The coefficients given tabularly:

Table 6.1: Full CRP: Hydrodynamic performance coefficients.

	FORE			**AFT**			**TOTAL**		
J	K_T	K_Q	η	K_T	K_Q	η	K_T	K_Q	η
1.5	0.0022	0.0062	8.40	0.0053	0.0059	21.13	0.0075	0.0122	14.61
1.4	0.0281	0.0117	53.58	0.0369	0.0146	56.26	0.0650	0.0263	55.07
1.3	0.0565	0.0167	69.85	0.0786	0.0232	70.11	0.1351	0.0399	70.01
1.2	0.0838	0.0215	74.51	0.1184	0.0311	72.61	0.2023	0.0526	73.39
1.1	0.1102	0.0259	74.48	0.1520	0.0377	70.61	0.2622	0.0636	72.19
1	0.1351	0.0297	72.35	0.1869	0.0442	67.31	0.3220	0.0739	69.34
0.9	0.1585	0.0330	68.78	0.2182	0.0498	62.74	0.3768	0.0828	65.15
0.8	0.1789	0.0355	64.09	0.2437	0.0542	57.24	0.4227	0.0898	59.96
0.75	0.1864	0.0362	61.52	0.2564	0.0564	54.27	0.4428	0.0926	57.10
0.7	0.1903	0.0361	58.79	0.2687	0.0584	51.23	0.4589	0.0945	54.12
0.6	0.2066	0.0377	52.36	0.2947	0.0626	44.92	0.5013	0.1003	47.71
0.5	0.2158	0.0379	45.26	0.3168	0.0660	38.22	0.5326	0.1039	40.79
0.4	0.2258	0.0388	37.00	0.3286	0.0674	31.02	0.5543	0.1063	33.20
0.3	0.2267	0.0382	28.37	0.3202	0.0657	23.25	0.5469	0.1039	25.13
0.25	0.2308	0.0388	23.69	0.3324	0.0684	19.34	0.5632	0.1071	20.91
0	0.2422	0.0407	0.00	0.3456	0.0707	0.00	0.5878	0.1113	0.00

The data shown in Table 6.1 presents the thrust coefficient K_T, torque coefficient K_Q and propeller efficiency for the FORE and AFT propellers separately and the CRP set as a whole. The same data is offered graphically with addition of comparable experimental

data from Miller [36, 37] in Figures 6.10, 6.11 and 6.12:

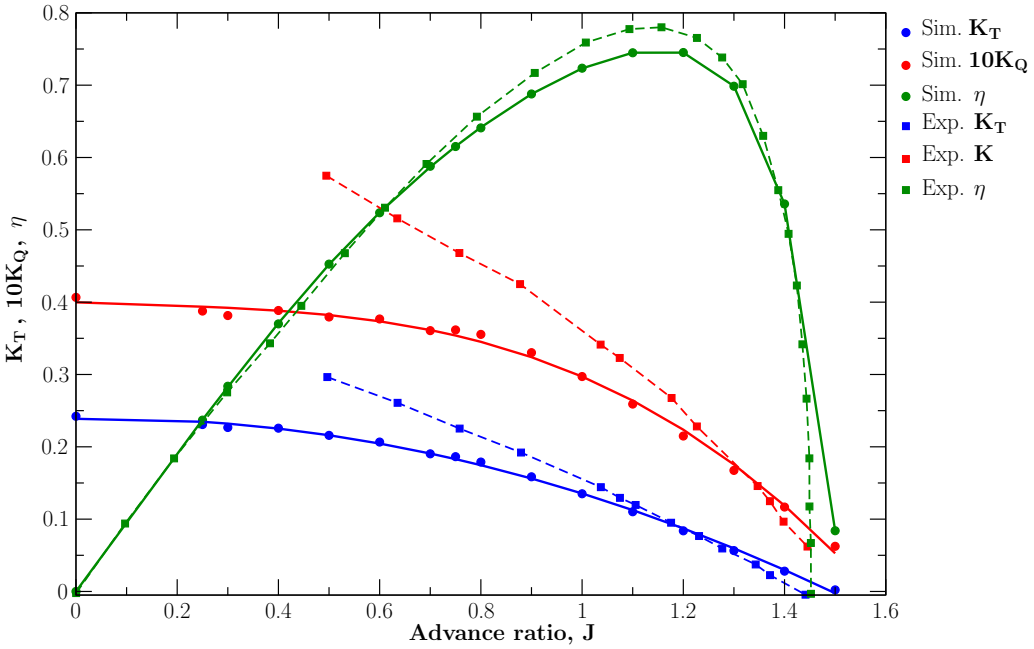

Figure 6.10: Full CRP: Fore propeller steady hydrodynamic coefficients.

Figure 6.10 shows the open-water characteristic of the FORE propeller based on data from full CRP numerical simulations and experimental data. The data based on simulation results shows good agreement with experimental data in higher efficiency, i.e. higher J, regions. The data deviates as the values of J decrease and the operating points move to regions of lower efficiency. This is explained by the fact that as the advance coefficient J decreases so does the axial velocity, thus moving into region with increasingly transient flow that cannot be accurately represented by the MRF method.

Open-water characteristics of the AFT propeller are presented in Fig. 6.11. As with the FORE propeller, the results of the AFT simulations show good agreement with experimental data for higher values of J with some deviation as the values of J decrease. Furthermore, the values of K_T follow the experimental data curve well, whereas the values of K_Q follow the trend of the experimental data but appear to be of equally lower value for each data point.

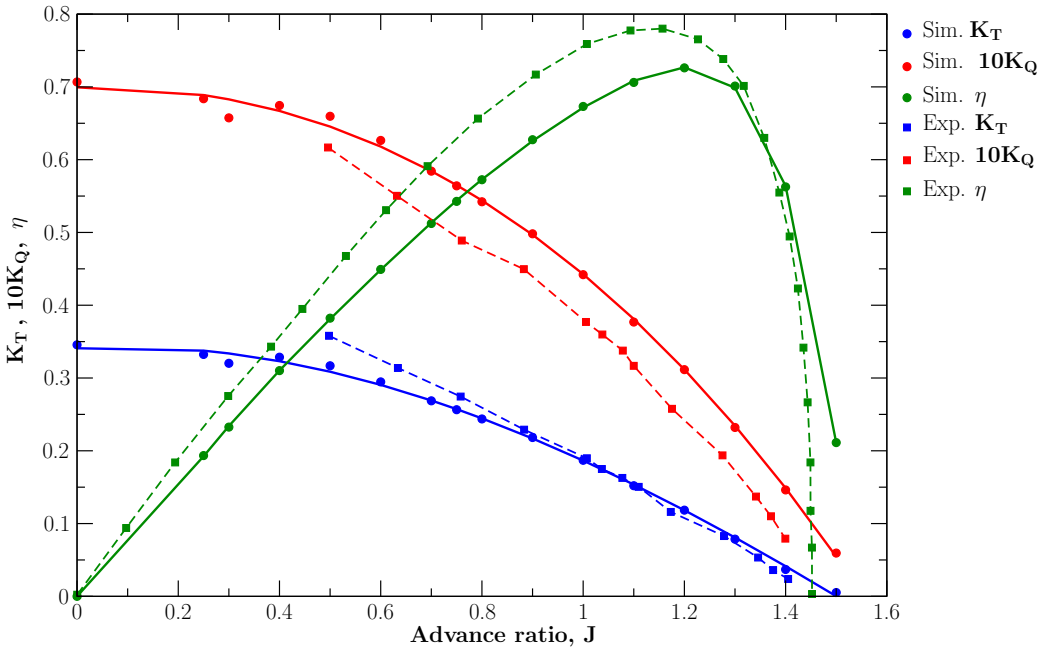

Figure 6.11: Full CRP: Aft propeller steady hydrodynamic coefficients.

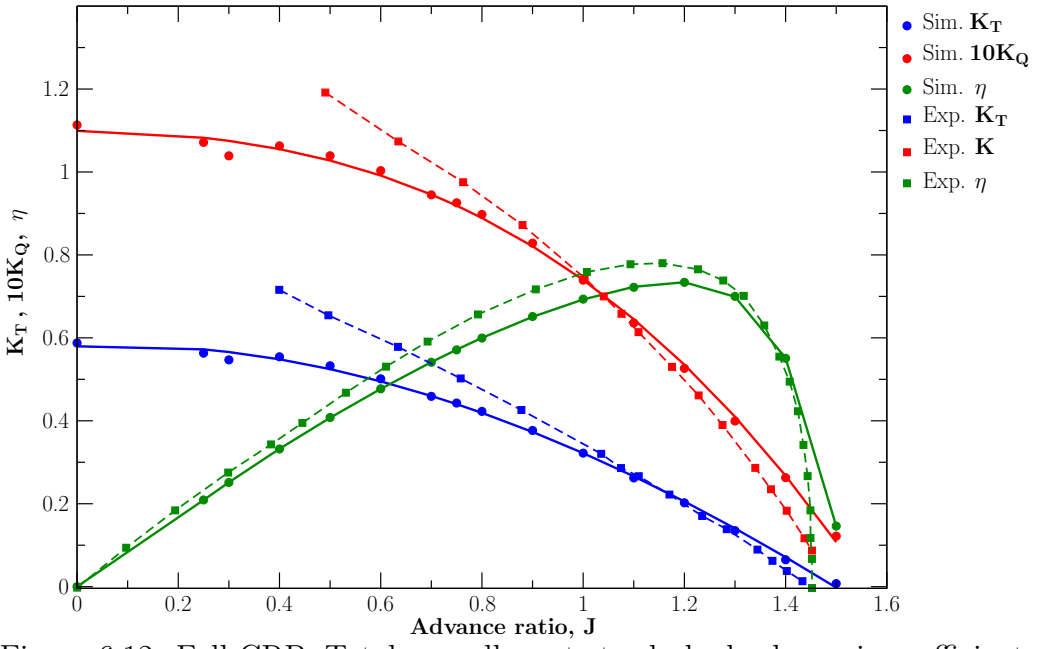

Figure 6.12: Full CRP: Total propeller set steady hydrodynamic coefficients.

By comparing the results for the FORE (Fig. 6.10) and the AFT (Fig. 6.11) propeller, it can be noted that the AFT propeller has generally higher values of thrust and torque coefficients throughout the simulated span of advance coefficients. This would mean that the secondary propeller of the set bears higher loads, which can be attributed to the wake of the first propeller affecting the secondary propeller.

The total open-water characteristics of the full propeller set is shown in Figure 6.12. The numerical data shows good agreement with the experimental values for regions of higher axial velocity, i.e. higher J, as the transient phenomena have little effect on the flow in such regions. As the the transient effects increase and the values of J decrease, the results deviate from the experimental curve. The deviation from experimental data is attributed to the inability of the steady-state MRF approach to capture transient phenomena.

The steady-state approach may not be accurate for operating points in the lower regions of the advance coefficient J, yet it provide satisfactory data for regions of near the best efficiency point (BEP) of the propeller. As most propellers are designed to work at BEP, data from steady-state MRF simulations becomes of great interest for propeller design.

6.3. Quarter CRP Geometry

In the previous section, an overview of data and flow fields from full domain simulations of the CRP set was given. The simulations served as an analysis of the fundamental behaviour of the CRP set, thus becoming a reference for further simulations where variants of the basic `ggi` interface will be used.

In this section, a quarter-geometry based computational domain is used for the simulation of a CRP set. This requires the use of the `cyclicGgi` and `overlapGgi` interfaces available in `foam-extend`, which are validated by comparison of quarter and full CRP simulation data. Both propellers are given a constant rotation of 12 rps and varying values of the advance coefficient J, depending on the simulated operating point.

By using the quarter-geometry domain, the simulation time needed to reach satisfying convergence may be greatly reduced as the quarter CRP simulation is less resource-intensive.

6.3.1. Steady-State Simulation, J = 0.5

For the full CRP simulation and the quarter CRP simulation to be comparable, using the `cyclicGgi` and the `overlpaGgi` interfaces, the same operating point $J = 0.5$ was chosen for both simulations. Moreover, the steady-state MRF method was used to handle modelling of the propeller rotation. Again, a rotational MRF zone was set-up around each propeller with the designated rotational speed.

The details of the geometry, boundary conditions and interfaces used are given in 5. Detailed examples on how the `overlapGgi` and `cyclicGgi` need to be set-up are given in Appendix A.

It should be noted that the post-processing software used for creation of graphical representation of numerical data, allows for transformation of the domain. The quarter domain is copied until the full domain is assembled, thus making the visualised data seem as if it were created from a complete domain.

Pressure Field

The kinematic pressure field from the quarter CRP simulation is given in Fig 6.13. The same as with the full CRP simulation (Fig. 6.1), the pressure field in the $z = const.$ plane shows higher and lower pressure areas near the propeller blades. These areas correspond to the suction and pressure sides of the propeller blades, depicted in detail in Fig. 6.14 and Fig. 6.14.

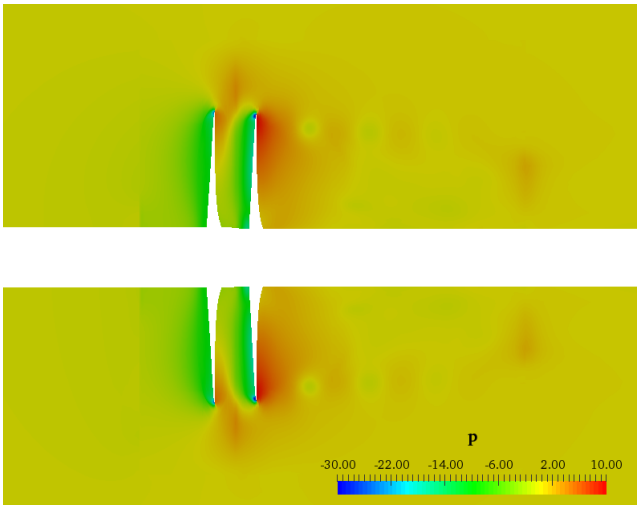

Figure 6.13: Quarter CRP: Pressure field in $z = const.$ plane.

Closer examination of the pressure distribution over the blade surfaces of the FORE and AFT propellers, reveals nearly identical distribution on both the pressure and suction sides of the blades as seen for the full CRP geometry. This would point to the fact that the use of `cyclicGgi` and `overlapGgi` interfaces has no apparent effect on pressure distribution over propeller surfaces.

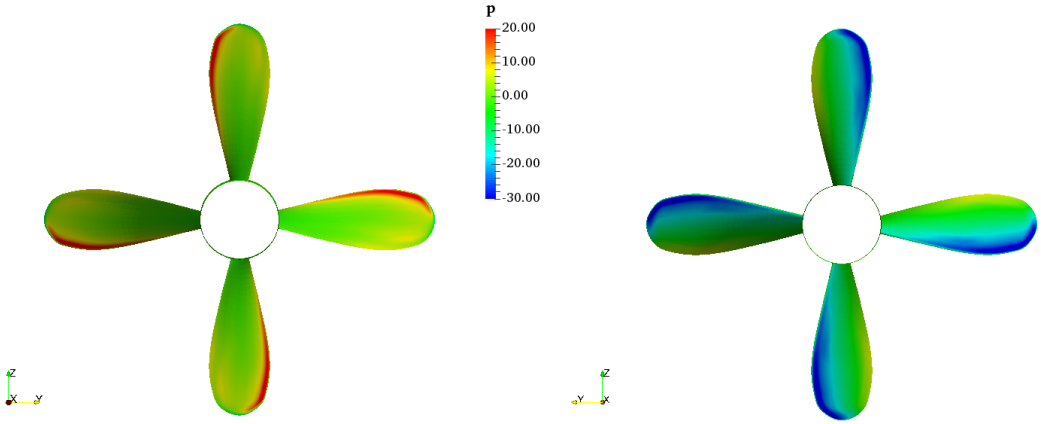

Figure 6.14: Quarter CRP: Pressure (left) and suction (right) side of FORE propeller.

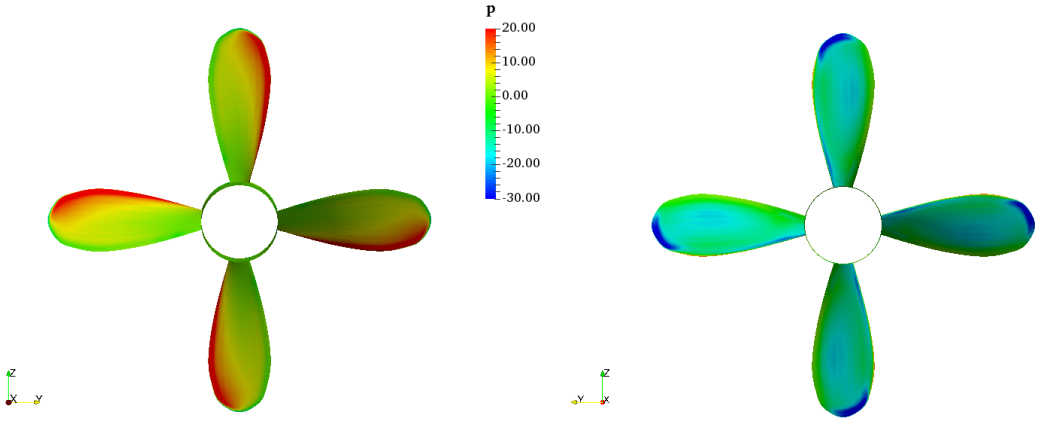

Figure 6.15: Quarter CRP: Pressure (left) and suction (right) side of AFT propeller.

Velocity Field

The velocity field in the $z = const.$ plane represented by values of the ratio of axial and inlet velocities U_x/U_i is given in Fig. 6.16. The same values are seen as for the full CRP simulations (Fig. 6.5), showing no effect potentially caused by the difference in interface handling).

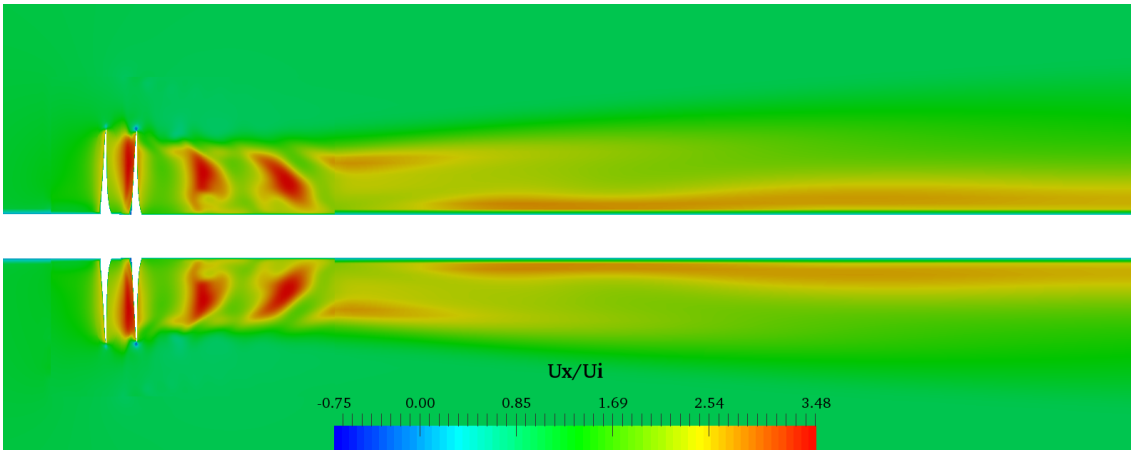

Figure 6.16: Quarter CRP: Velocity field in $z = const.$ plane.

Figure 6.17 shows the propeller wake field downstream of the two propellers. Looking at the same scale for values of U_x/U_i, the velocity field at $x/R = 0$ and $x/R = 0.334$ closely resembles the one seen for the full CRP geometry at same locations (Fig. 6.6). The higher values of the axial velocity in the wake of the second propeller are attributed to the reduction in tangential velocity caused by the addition of the AFT propeller.

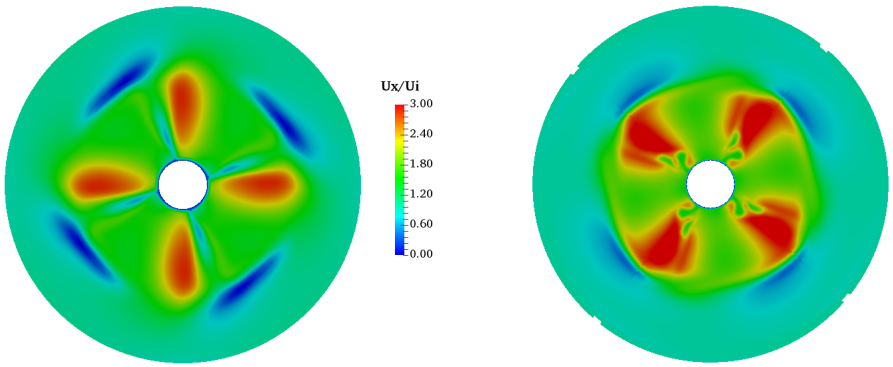

Figure 6.17: Quarter CRP: Velocity field at $x/R = 0$ and $x/R = 0.334$.

Turbulence and Vorticity

The turbulence in the CRP flow field is presented by values of TKE. The distribution of TKE in the $z = const.$ plane presented in Fig. 6.18 shows very good agreement with results of the full CRP simulation (Fig. 6.7).

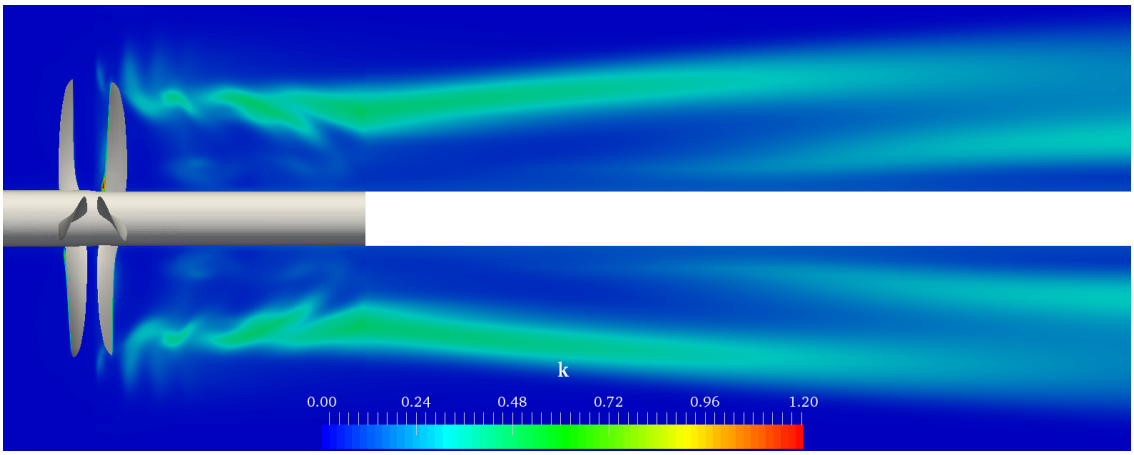

Figure 6.18: QuarterCRP: TKE in $z = const.$ plane.

As expected, close examination of the distribution of TKE over CRP blade surfaces reveals the highest values to be concentrated at the leading edge and blade tips. The surface distribution of TKE for both propellers of the quarter domain simulation of CRP is given in Fig. 6.19.

Q-contours with values $Q > 3 \cdot 10^3$ were used to represent vorticity in the near-propeller regions (Fig. 6.20). Interestingly, the contours calculated from quarter geometry simulation show minor differences when compared to those of the full geometry simulations (Fig. 6.9). As the differences do not appear to be significant, they are not the result of different interface handling methods and may be attributed the post-processing tool used to calculate the Q-criterion values.

In summary, analysis of the quarter CRP simulation data fields did not yield any significant differences when compared to the full domain simulation. This validates the use of quarter of the CRP computational domain for further numerical simulations of the CRP set. Furthermore, the use of `overlapGgi` and `cyclicGgi` interfaces to facilitate communication between the two rotating quarter-domain regions and with the static far field region, has no apparent effect on the simulation result, other than reducing the simulation runtime.

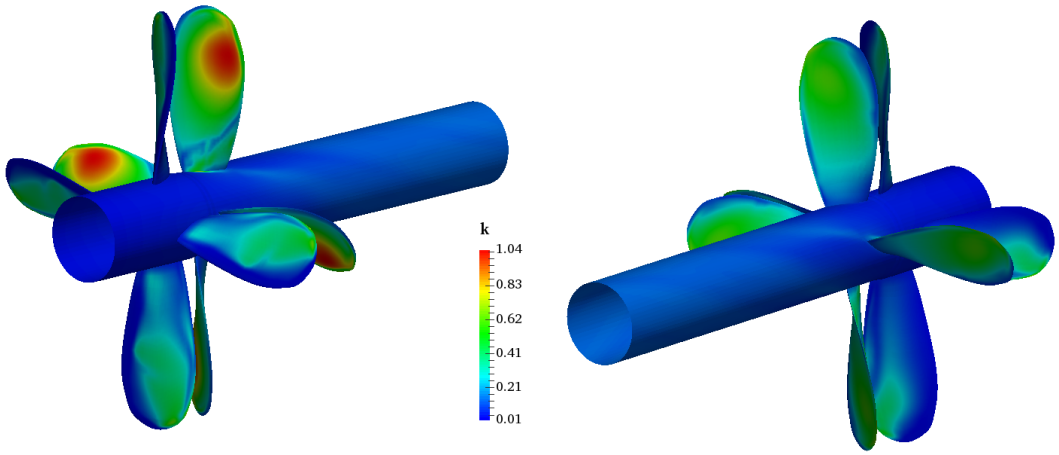

Figure 6.19: Quarter CRP: Distribution of TKE on propeller blades.

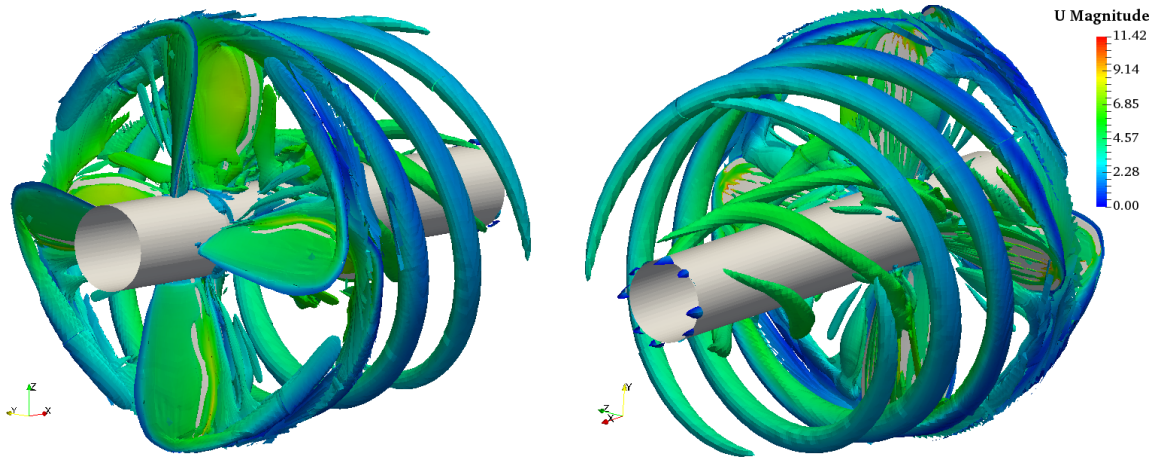

Figure 6.20: Quarter CRP: Vortices matching Q-criterion $Q > 3 \cdot 10^3$

6.3.2. Steady-State Simulation, J = 1.1

With the quarter CRP simulation set-up verified against the full CRP simulation, it may be used to simulate different operating points. $J = 1.1$ was chosen as it represents a CRP operating point with high values of efficiency. Graphical representations of various fields from the quarter CRP simulation with $J = 1.1$ simulation are presented next.

Pressure Field

Figure 6.21 depicts the kinematic pressure field around the CRP set. As expected, lower pressure areas are present on the suction side of the propeller blades and the higher pressure areas may be noticed on the blade pressure side. When compared to the same representation of the pressure field for the quarter CRP case with $J = 0.5$ (Fig. 6.1), lower absolute values of pressure may be seen near the blade surfaces.

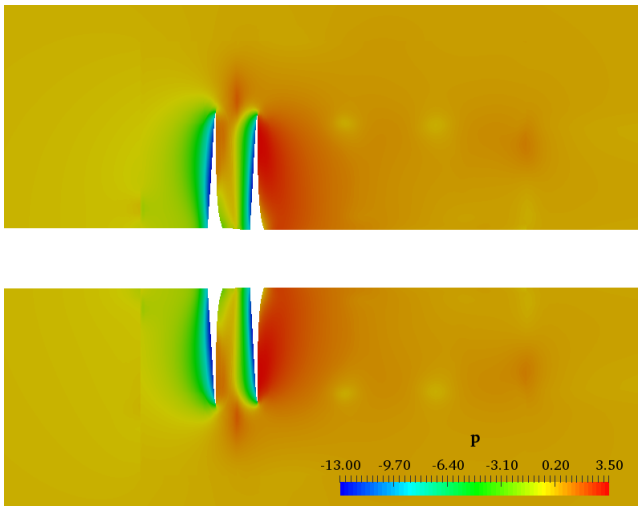

Figure 6.21: Quarter CRP: Pressure field in $z = const.$ plane, $J = 1.1$.

A more detailed representation of the kinematic pressure distribution over the blade surfaces is given in Figures 6.22 and 6.23. The high pressure regions may be found along the leading edge of both the FORE and AFT propeller blades. On the other hand, the lower pressure regions are spread over the blade surface of the suction side. Higher absolute values of pressure on the AFT propeller of the set may be attributed to the wake of the FORE propeller and the resulting interaction.

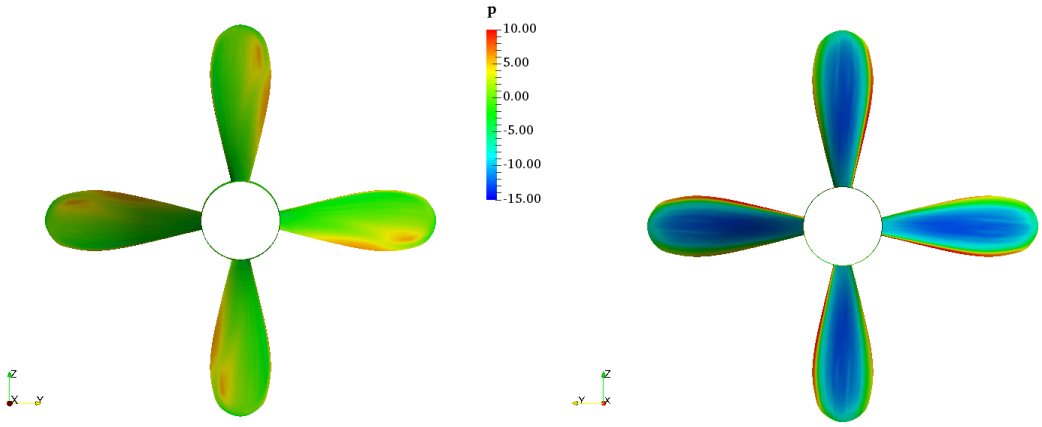

Figure 6.22: Quarter CRP: Pressure (left) and suction (right) side of FORE propeller, $J = 1.1$.

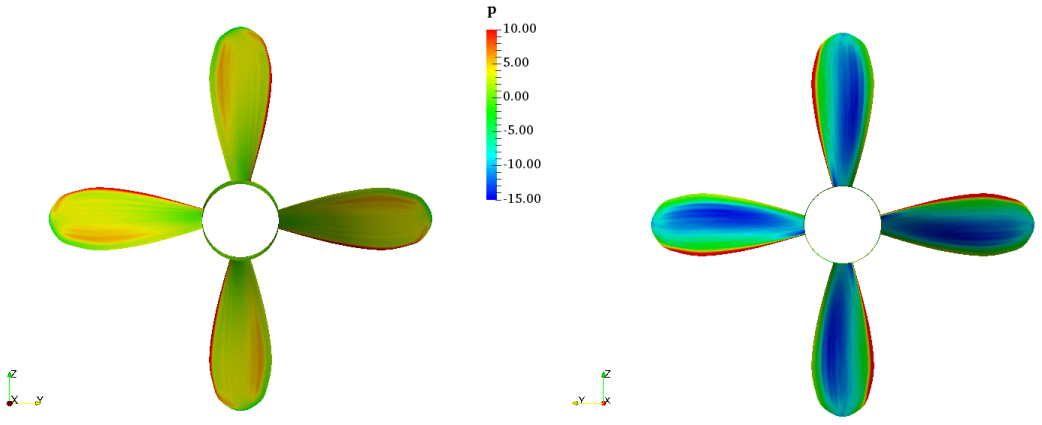

Figure 6.23: Quarter CRP: Pressure (left) and suction (right) side of AFT propeller, $J = 1.1$.

Velocity Field

The velocity field is presented as values of the axial and inlet velocity ratio U_x/U_i. The value of the inlet velocity corresponding to the advance coefficient $J = 1.1$ equals $U_i = 4.0286$. As the values of the inlet velocity of $J = 1.1$ and $J = 0.5$ differ, the two fields may not be compared directly. Fig. 6.24 represents the velocity field in the $z = const.$ plane, with a representation of velocity at two $x = const.$ planes is given in Fig. 6.17. As expected, the axial velocity downstream of the AFT ($x/R = 0.334$) propeller shows higher values than downstream of the FORE propeller ($x/R = 0$).

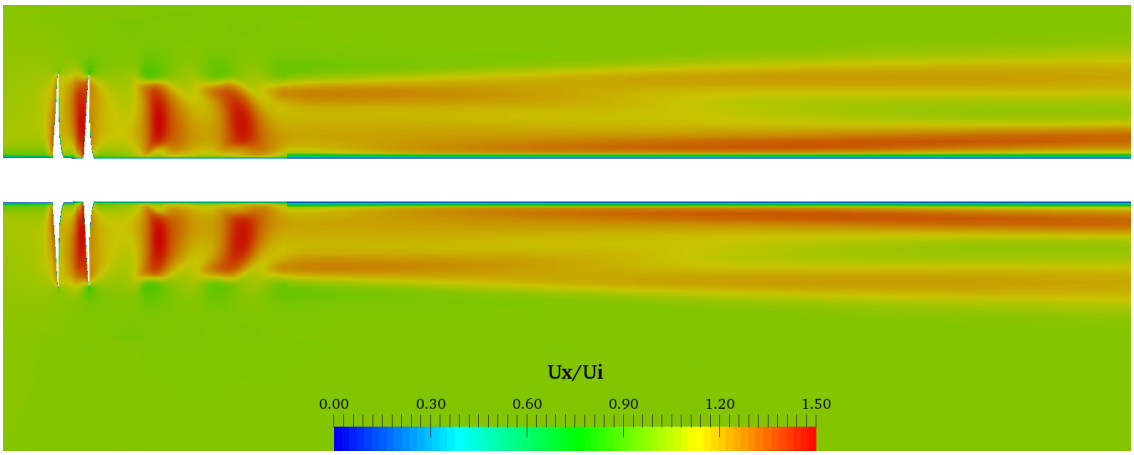

Figure 6.24: Quarter CRP: Velocity field in $z = const.$ plane, $J = 1.1$.

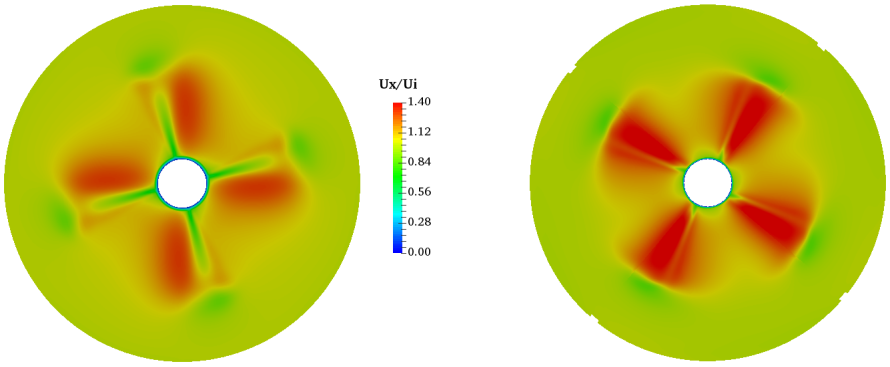

Figure 6.25: Quarter CRP: Velocity field at $x/R = 0$ and $x/R = 0.334$, $J = 1.1$.

Turbulence and Vorticity

The values of TKE, as a chosen measure of turbulence, in the $z = const.$ plane are shown in Figure 6.26 and the surface distribution of TKE over the propeller blades is presented in Fig. 6.27. TKE values in the downstream wake of the CRP set appear to be low with highest values concentrated at the propellers. The distribution of TKE over the blade surfaces shows the highest values to be concentrated near the leading edge of each blade. Moreover, values of TKE appear to be higher at the blade pressure side.

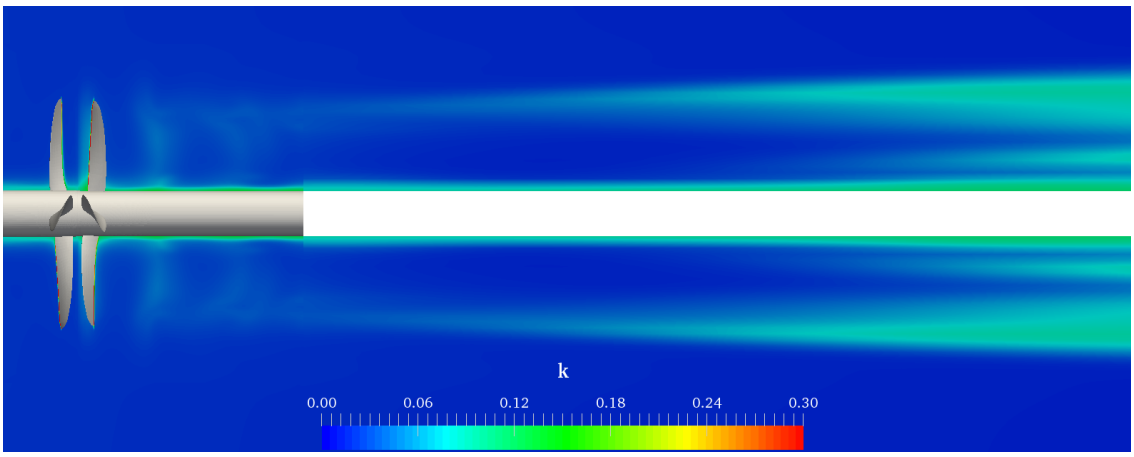

Figure 6.26: QuarterCRP: TKE in $z = const.$ plane, $J = 1.1$.

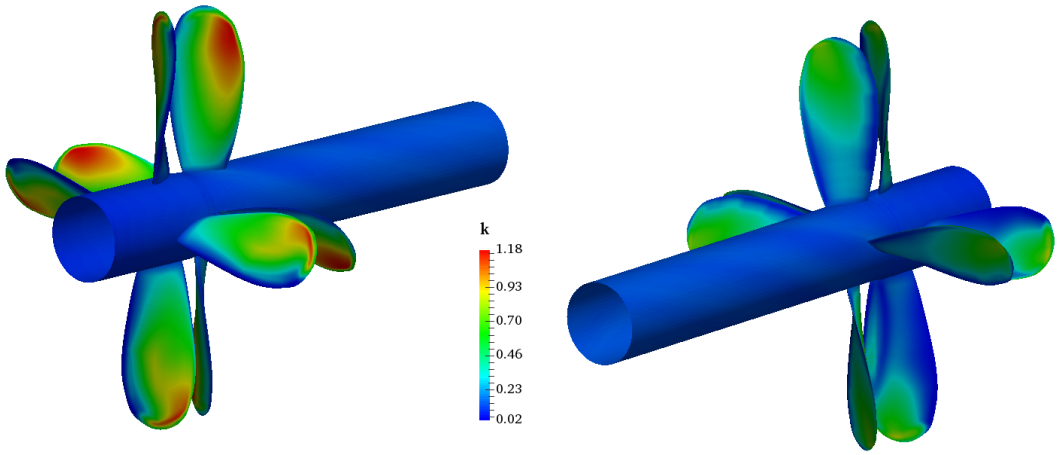

Figure 6.27: Quarter CRP: Distribution of TKE on propeller blades, $J = 1.1$.

Q-contours are used to represent vorticity around the CRP set. A Q-criterion value of $Q > 3 \cdot 10^3$ was chosen as a threshold for the contours presented in Figure 6.28.

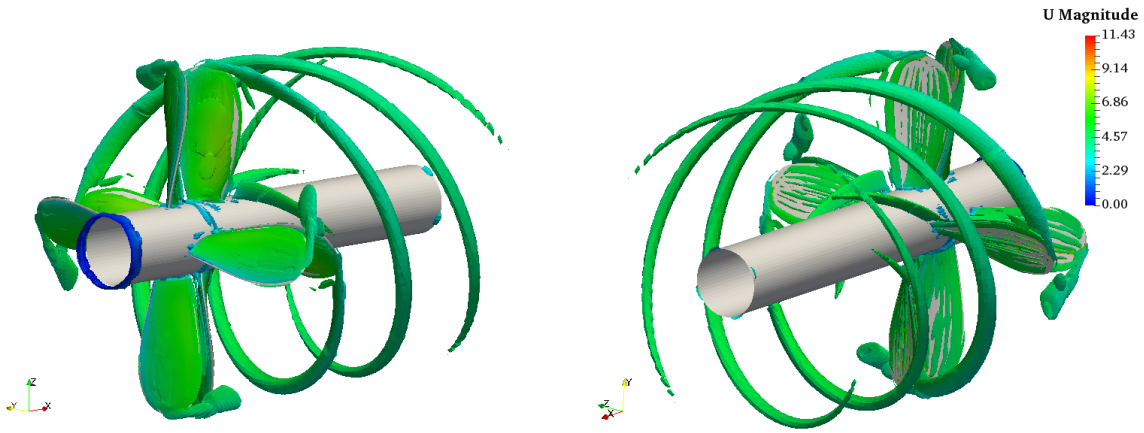

Figure 6.28: Quarter CRP: Vortices matching Q-criterion $Q > 3 \cdot 10^3$, $J = 1.1$.

6.3.3. Hydrodynamic Performance

The hydrodynamic performance coefficients calculated from the results of the quarter CRP numerical simulation are presented in Table 6.2. A separate numerical simulation was performed for each of the data points, i.e. CRP operating point, and the corresponding value of J from the table.

Table 6.2: Quarter CRP: Hydrodynamic performance coefficients.

	FORE			**AFT**			**TOTAL**		
J	K_T	K_Q	η	K_T	K_Q	η	K_T	K_Q	η
1.5	0.0028	0.0061	10.91	0.0068	0.0056	29.42	0.0096	0.0117	19.73
1.4	0.0275	0.0115	53.05	0.0360	0.0144	55.82	0.0635	0.0259	54.59
1.3	0.0561	0.0166	69.74	0.0774	0.0228	70.08	0.1335	0.0395	69.94
1.2	0.0836	0.0214	74.48	0.1173	0.0308	72.67	0.2009	0.0523	73.41
1.1	0.1101	0.0259	74.51	0.1515	0.0375	70.69	0.2616	0.0634	72.25
1	0.1351	0.0298	72.20	0.1855	0.0439	67.20	0.3207	0.0737	69.22
0.9	0.1611	0.0337	68.46	0.2072	0.0477	62.27	0.3682	0.0814	64.84
0.8	0.1812	0.0360	64.06	0.2309	0.0517	56.82	0.4121	0.0878	59.79
0.75	0.1902	0.0370	61.41	0.2413	0.0534	53.91	0.4315	0.0904	56.98
0.7	0.1923	0.0365	58.68	0.2525	0.0553	50.87	0.4448	0.0918	53.98
0.6	0.2114	0.0387	52.22	0.2814	0.0601	44.71	0.4928	0.0988	47.65
0.5	0.2161	0.0380	45.25	0.3168	0.0659	38.25	0.5328	0.1039	40.81
0.4	0.2323	0.0401	36.87	0.3210	0.0662	30.89	0.5533	0.1063	33.15
0.3	0.2318	0.0391	28.28	0.3135	0.0647	23.14	0.5453	0.1038	25.08
0.25	0.2333	0.0391	23.74	0.3186	0.0660	19.22	0.5518	0.1051	20.90
0	0.2417	0.0405	0.00	0.3387	0.0699	0.00	0.5804	0.1104	0.00

Open-water characteristics of the FORE and AFT propeller, shown in Fig. 6.29, are given by curves, fitted to data points acquired from performed steady-state MRF numerical simulations. They represent the K_T and K_Q coefficients, together with propeller efficiency η. Analysis of propeller characteristics shows higher values of thrust and torque for the AFT propeller, which is consistent with the findings of full CRP simulations.Hydrodynamic performance coefficients of the total CRP set and the resulting open-water characteristic of the set are given in Fig. 6.30. The figure shows a comparison of the quarter CRP simulation with comparable experimental results [36, 37]. The same as with the full CRP set, the numerical data shows good agreement with the experiments for higher efficiency regions and stronger disagreement as the values of J descend towards regions with larger influence of transient phenomena.

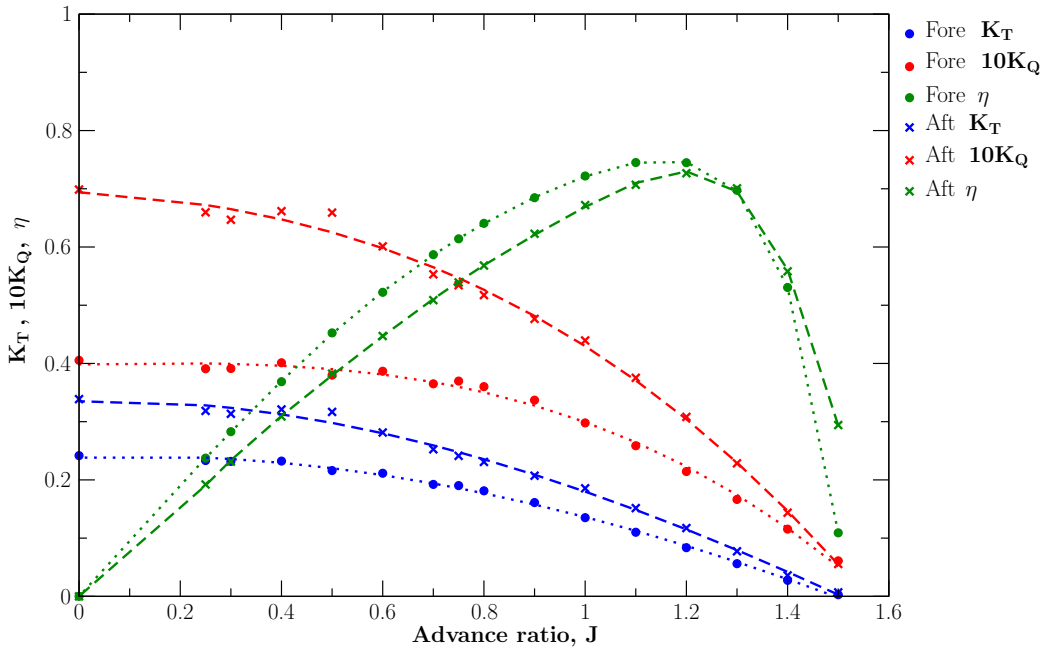

Figure 6.29: Quarter CRP: Fore and aft propeller steady hydrodynamic coefficients.

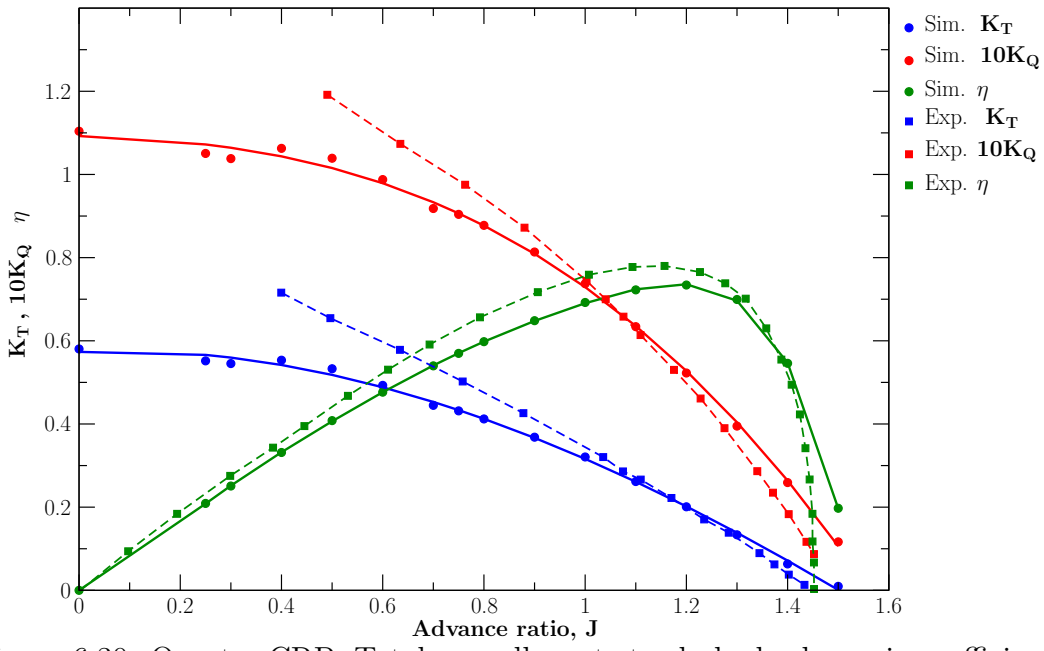

Figure 6.30: Quarter CRP: Total propeller set steady hydrodynamic coefficients.

Hydrodynamic performance coefficients of each propeller and the whole CRP set, for both the $J = 0.5$ and $J = 1.1$ simulations, are compared to experimental in Table 6.3. Furthermore, values of the relative error are included as means assessing the accuracy of each solution when compared to experimental data. Analysis of the data presented in Table 6.3 confirms the previously stated notion that accuracy of steady-state data is dependent on the CRP operating point. Relative error is larger for hydrodynamic coefficients associated with $J = 0.5$ operating point, as it is farther from high efficiency performance points, making the influence of transients more pronounced. This makes the steady-state simulation unable to produce accurate results. On the other hand, data for the $J = 1.1$ operating point shows good agreement for most of the hydrodynamic coefficients, as this operating points resides near the best efficiency point where transient phenomena have little effect.

Table 6.3: Steady hydrodynamic performance coefficients.

	J = 0.5		**J = 1.1**	
	Value	Error [%]	Value	Error [%]
$\mathbf{K_{Tf}}$	0.2161	37.24	0.1101	9.82
$\mathbf{K_{Ta}}$	0.3168	12.80	0.1515	0.76
$\mathbf{K_{T}}$	0.5328	22.71	0.2616	4.57
$\mathbf{K_{Qf}}$	0.0378	52.10	0.0259	25.71
$\mathbf{K_{Qa}}$	0.0659	-6.50	0.0375	-14.23
$\mathbf{K_{Q}}$	0.1389	14.93	0.0634	2.07

6.3.4. Quarter CRP Hydrodynamic Performance Validation

The comparison of field data from quarter CRP and full CRP numerical simulation did not show any significant differences, which validated the use of quarter geometry simulations from the aspect of field data analysis. As the open-water characteristics of CRP are to be studied in further simulations based on the quarter CRP domain, the validity of these characteristics must be examined.

A comparison of the hydrodynamic performance coefficients K_T, K_Q and resulting propeller efficiency calculated from quarter and full domain CRP simulations is given in Fig. 6.31 and 6.32. Data for the FORE propeller is shown in Fig. 6.31 and the data for the AFT propeller is given in Fig. 6.32.

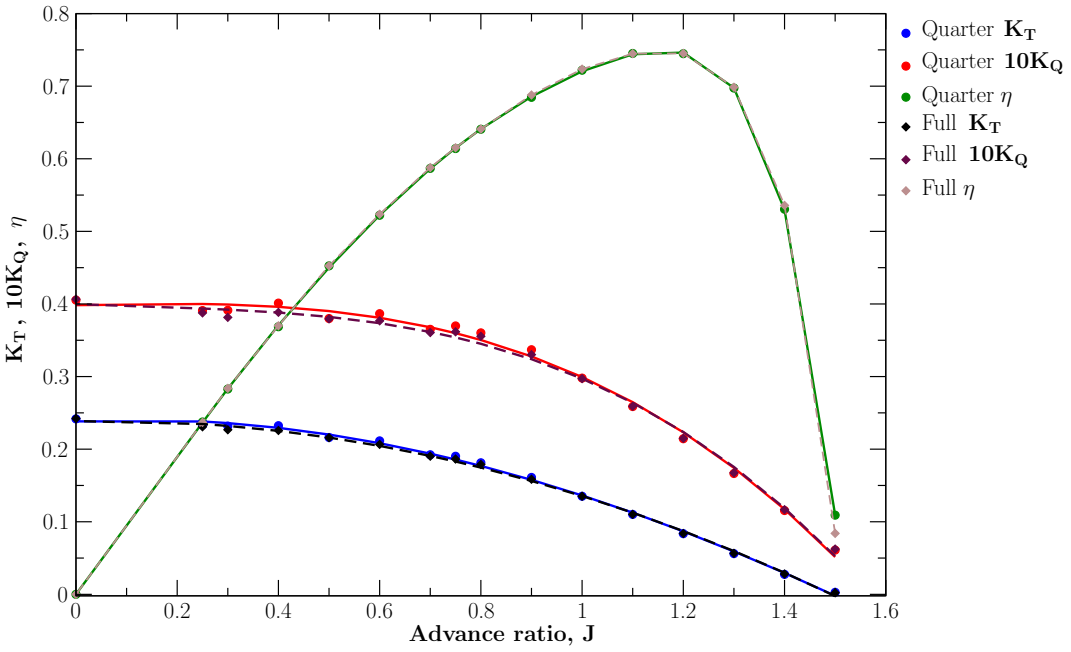

Figure 6.31: FORE prop. hydrodynamic coeff. comparison: quarter vs. full CRP.

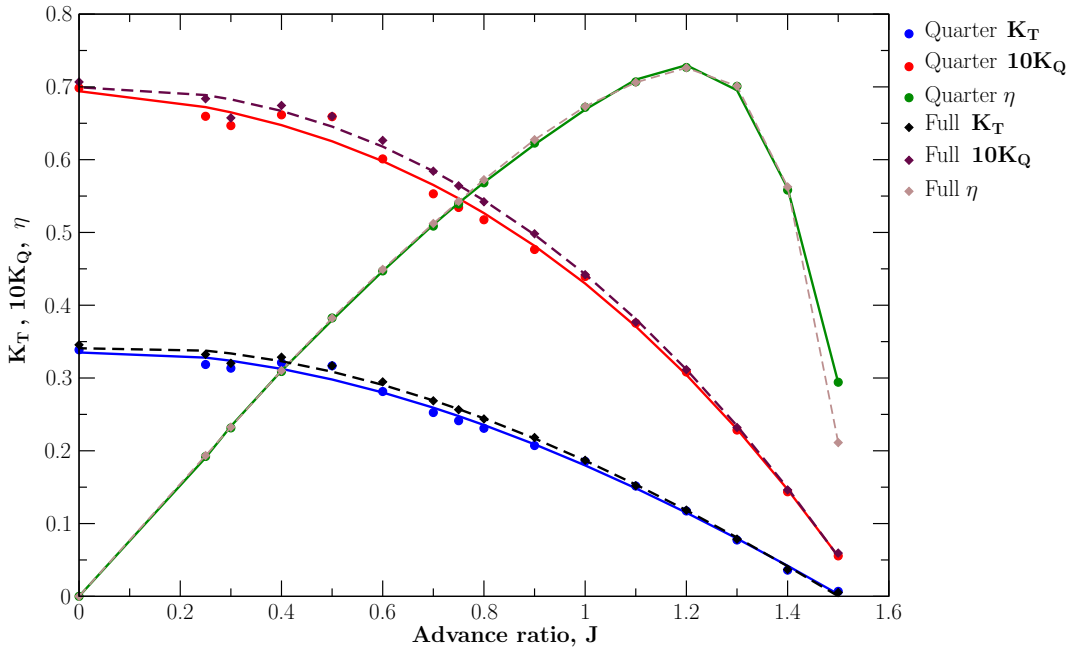

Figure 6.32: AFT prop. hydrodynamic coeff. comparison: quarter vs. full CRP.

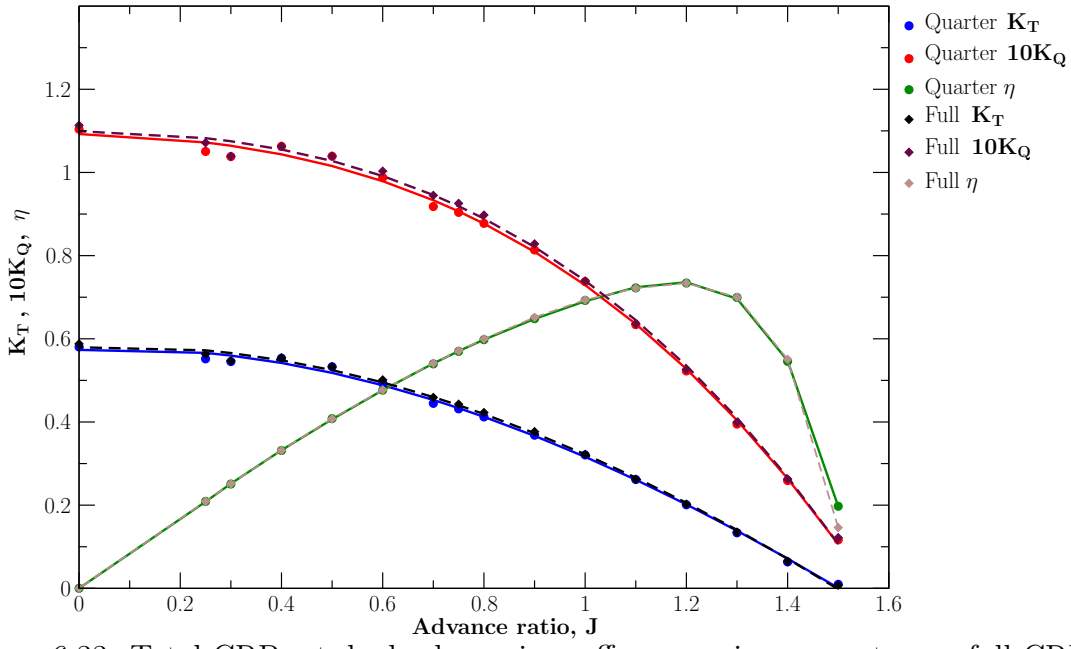

Figure 6.33: Total CRP set. hydrodynamic coeff. comparison: quarter vs. full CRP.

Hydrodynamic performance of FORE propeller shown in Fig. 6.31 shows nearly ideal agreement between quarter and full CRP results. On the other hand, some differences between the full and quarter simulation data for the AFT propeller shown in Fig. 6.32 are present. These minor discrepancies may be considered as having no effect on the total open-water characteristic of CRP.

Comparison of the total CRP hydrodynamic performance coefficients is shown in Fig. 6.33. The full and quarter CRP simulation data shows nearly identical characteristics with some minor disagreement which may be considered negligible. With the results of the two simulated domains showing no major differences in regard to hydrodynamic performance, the quarter domain approach may be considered valid for use in further simulations with the purpose of determining propeller open-water characteristics.

6.4. Effects of Initial Propeller Position

This section investigates the idea that different starting positions of one of the propellers, relative to the other propeller, may affect the results of steady-state simulations.

It is suspected that a transient component of propeller-to-propeller interaction may be significant. For MRF simulations, all relative positions of "frozen rotor" blades should be equally representative. It is suspected that this is not the case and will be further investigated. As a computationally undemanding way of determining the influence of relative blade positions to "frozen rotor" results, the simulation is repeated for various propeller blade positions. For the "frozen rotor" approach to be valid for this case, results for all blade positions should the be the same.

Four new simulations based on the steady-state quarter CRP simulation were conducted. Variations of the quarter propeller geometry presented in Chapter 5. were used with addition of varying propeller displacement. The geometry was varied by keeping the AFT propeller at a fixed starting position and changing the angular displacement of the FORE propeller, as shown in Figure 6.34.

Different values of the relative rotation angle θ were chosen to determine the initial propeller position for the steady-state simulation. The baseline values were determined by the MRF quarter-case with $J = 0.5$ and $\theta = 0$. The same value of the displacement angle $\theta = 0$ was used for all simulations analysed preceding this section. New steady-state simulations were performed with a fixed value of the advance coefficient $J = 0.5$

and with the angle θ varied in value from 15° to 60° by increments of 15°.

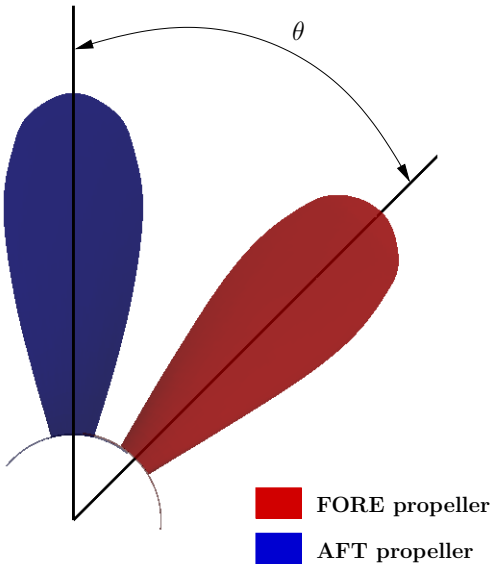

Figure 6.34: Initial propeller placement.

The results were analysed in form of steady hydrodynamic performance coefficients. The values of total CRP set coefficients are compared to available experimental data for $\theta = 0$ and are given in Table 6.4.

Table 6.4: Unsteady hydrodynamic performance coefficients.

	$\mathbf{K_T}$		$\mathbf{K_Q}$		η	
θ	Value	Error [%]	Value	Error [%]	Value	Error [%]
0°	0.5328	22.71	1.0390	14.93	0.4081	6.77
15°	0.5903	10.76	1.1656	2.44	0.4030	8.12
30°	0.6339	3.15	1.2504	-4.50	0.4034	8.01
45°	0.6445	1.44	1.2655	5.64	0.4053	7.50
60°	0.6368	2.68	1.2599	5.22	0.4022	8.33

Analysis of the data given in Table 6.4 reveals how much the initial positioning of propellers in the CRP set affects the final solution. This could be explained by looking at how the unsteady thrust of the propeller set changes during a transient simulation (e.g. Figure 6.57 a)). It may be noted that the thrust changes with the relative position

of the propeller, meaning that if the propeller is "frozen" in a different position, different values of thrust would be measured. In the same way, if steady-state simulations were conducted with the propellers "frozen" in different relative position, different results could be expected, which is supported by data from the Table 6.4.

6.5. Mixing Plane Simulation

With the `overlapGgi` and `cyclicGgi` interfaces used in quarter CRP simulations successfully validated, a quarter domain simulation using the `mixingPlane` interface is conducted. `CyclicGgi` interfaces are used to establish communication with periodically rotating patches with the `mixingPlane` interface facilitating communication between mesh region. Detailed explanation of the geometry, interfaces and domain used was presented in Chapter 5. with examples of interface set-up given in appendix A.

6.5.1. Simulation Results

Results of a steady-state simulation using the `mixingPlane` interface for a propeller operating point with a corresponding value of the advance coefficient of $J = 0.5$ are presented, thus making them comparable to previously presented simulations.

Pressure Field

The kinematic pressure field in the $z = const.$ plane is presented in Fig 6.35. The expected high- and low- pressure areas can be seen near the blades of each propeller. Additional relatively high pressure areas may be seen downstream of the CRP set. These areas occur at the exact position of the interface separating the AFT propeller region from the far field region and may be attributed to the way the `mixingPlane` interface handles communication.

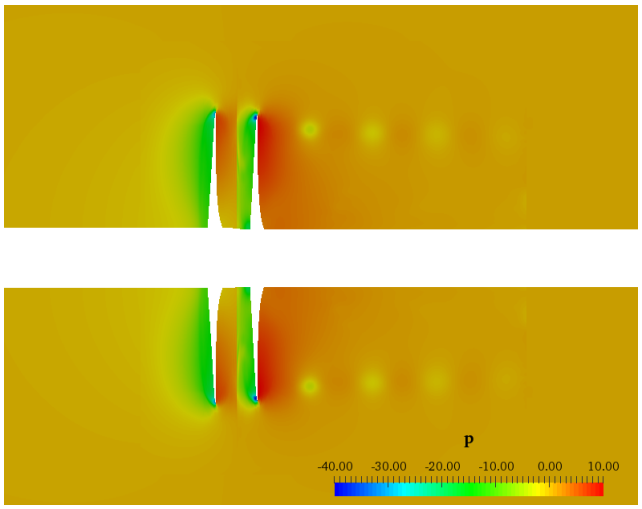

Figure 6.35: `mixingPlane`: Pressure field in $z = const.$ plane.

Mid-propeller slices of the kinematic pressure field are shown in Fig. 6.36. The higher pressure regions at the FORE propeller slice (Fig. 6.36-left), which originate from the blade tips, appear larger than those found in the previous simulation, indicating higher pressure values. On the other hand, both the high and low pressure regions at the AFT propeller (Fig. 6.36-right) appear to be concentrated, showing more consistent values of pressure.

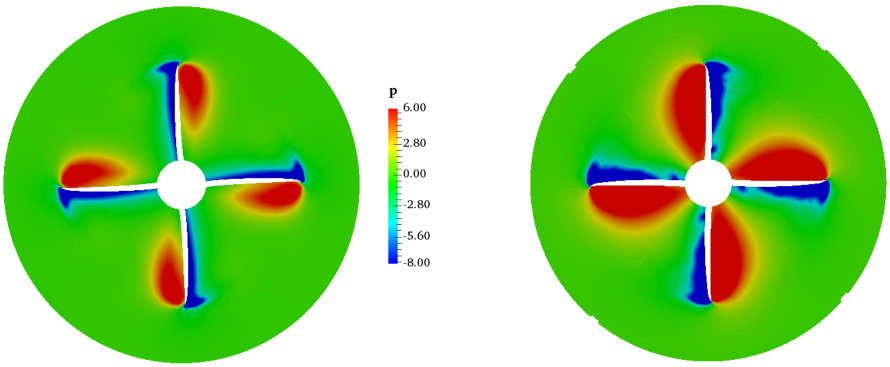

Figure 6.36: `mixingPlane`: Mid-propeller slice.

Figures 6.37 and 6.38 show the pressure distribution along the blades of the FORE and AFT propeller respectively. The most notable difference when compared to the quarter CRP simulation presented in the previous section can be seen on the suction

side of both propellers. Lower values of pressure may be observed on the suction side of the propellers, without the discontinuity of the low pressure region at the leading edge of AFT propeller seen in the previously presented simulations.

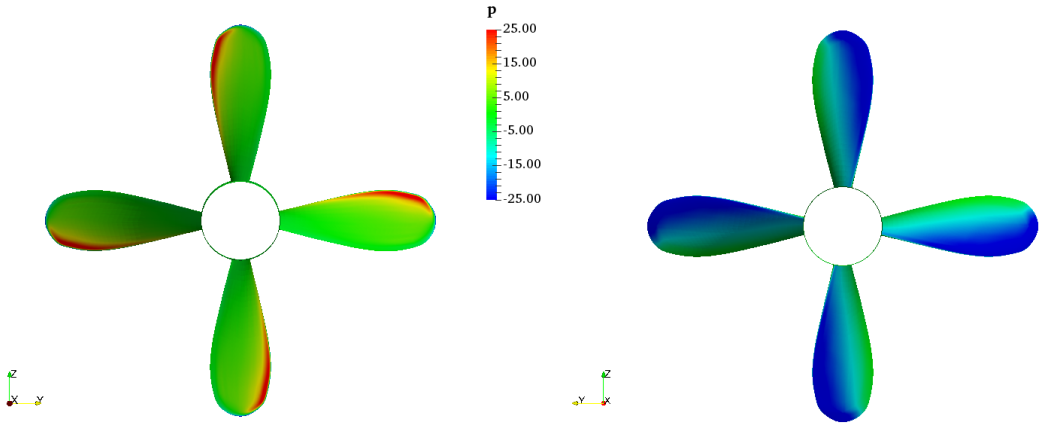

Figure 6.37: `mixingPlane`: Pressure (left) and suction (right) side of FORE propeller.

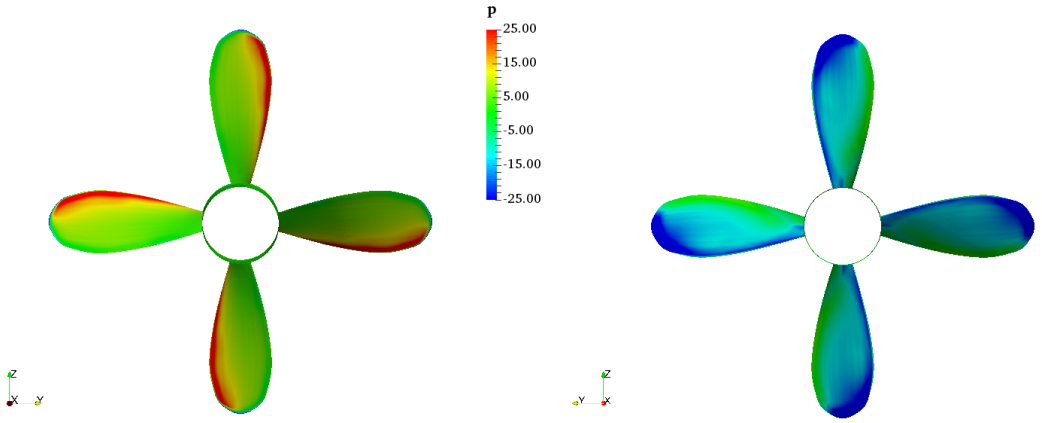

Figure 6.38: `mixingPlane`: Pressure (left) and suction (right) side of AFT propeller.

Velocity Field

The velocity field, represented by the ratio of the axial velocity U_x and the inlet velocity U_i, is shown in Fig. 6.39. The value of the inlet velocity corresponding to the advance coefficient is $U_i = 1.8312$. The velocity field shows an abrupt discontinuity at the `mixingPlane`, which is the result of averaging performed at the interface. After the interface, the flow continues to show consistent values of the axial/inlet velocity ratio.

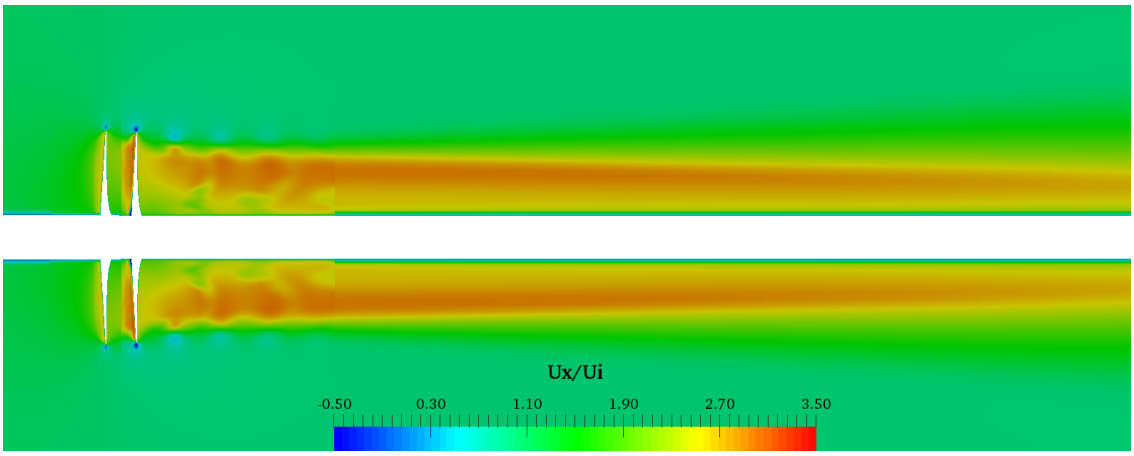

Figure 6.39: `mixingPlane`: Velocity field in $z = const.$ plane.

Figure 6.40 shows the velocity field at two cutting planes positioned behind the FORE ($x/R = 0$) and AFT ($x/R = 0.334$) propeller. By using the same scale and comparing to Fig. 6.17 lower values of axial velocity may be noticed. Moreover, the distribution of velocity over the cutting planes more averaged values, which is an effect of the mixing performed at the interface.

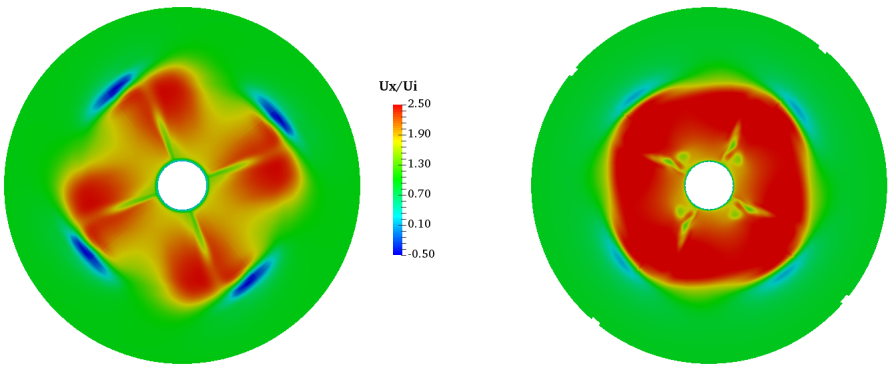

Figure 6.40: `mixingPlane`: Velocity field at $x/R = 0$ and $x/R = 0.334$.

Turbulence and Vorticity

The turbulent kinetic energy over the $z = const.$ plane is presented in Fig. 6.41. As with previous simulations, the highest values of k are concentrated near the blade tips. The only major difference from other simulations is the discontinuity of the k field at the `mixingPlane`. As result of the averaging at the interface the downstream becomes highly regular.

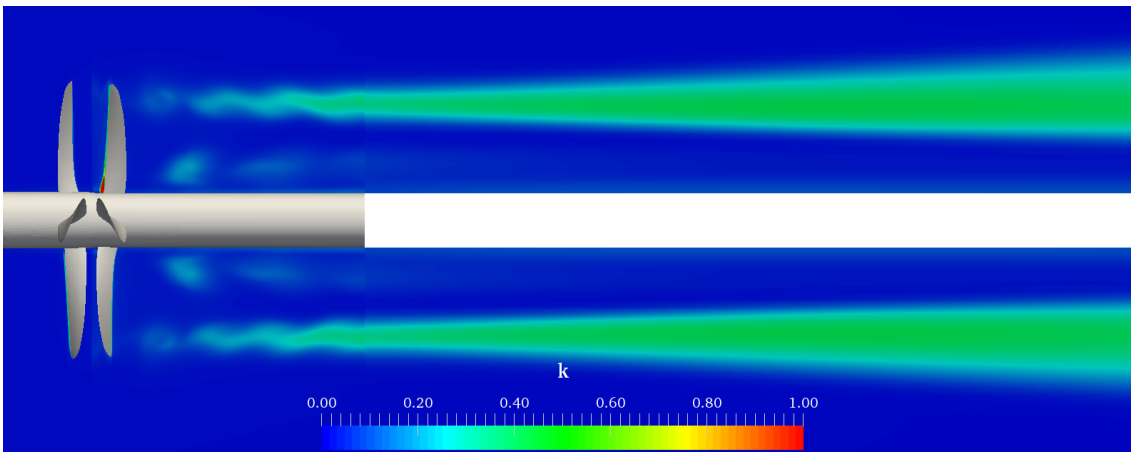

Figure 6.41: `mixingPlane`: TKE in $z = const.$ plane.

Presence of the `mixingPlane` at the interface connecting the AFT propeller mesh region to the far field region affects the TKE distribution over the propeller surfaces. Shown in Fig. 6.42 is the distribution of TKE over the blades of the CRP set. When compared with previous simulations of the CRP, lower values of TKE may be noticed.

The Q-criterion, described in subsection 4.4.2., with an arbitrary value of Q was used as a measure of vorticity, thus defining areas with vortices having an energy rate higher than the value set by Q. Q-contours with $Q > 3 \cdot 10^3$, which are coloured by values of velocity magnitude, are shown in Fig. 6.43. It can be concluded that the Q-contours from the `mixingPlane` simulation show good agreement with the Q-contours of the `overlapGgi` quarter case shown in Fig. 6.20.

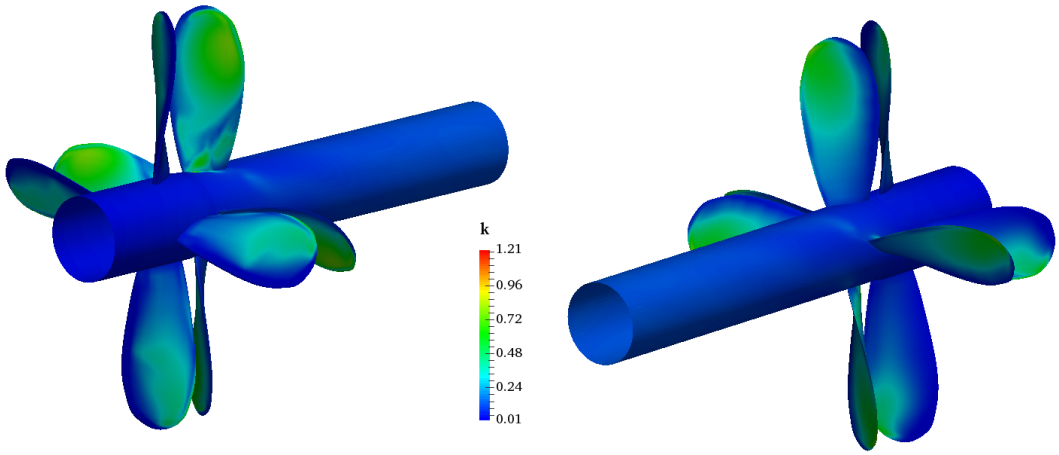

Figure 6.42: `mixingPlane`: Distribution of TKE on propeller blades.

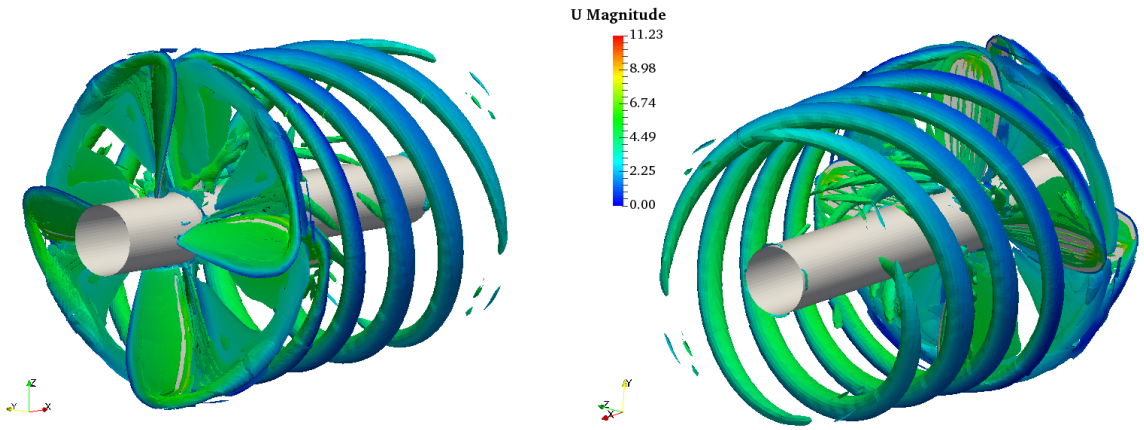

Figure 6.43: `mixingPlane`: Vortices matching Q-criterion $Q > 3 \cdot 10^3$

6.5.2. Hydrodynamic Performance

Hydrodynamic performance coefficients calculated from the results of the quarter CRP simulation which uses the `mixingPlane` are presented in Table 6.5. A separate numerical simulation was performed for each of the data points, i.e. CRP operating point, and the corresponding value of J from the table.

Table 6.5: `mixingPlane`: Hydrodynamic performance coefficients.

	FORE			**AFT**			**TOTAL**		
J	K_T	K_Q	η	K_T	K_Q	η	K_T	K_Q	η
1.5	0.0057	0.0048	28.31	0.0025	0.0063	9.43	0.0082	0.0111	17.62
1.4	0.0249	0.0115	48.07	0.0356	0.0139	57.16	0.0605	0.0254	53.04
1.3	0.0587	0.0178	68.10	0.0727	0.0213	70.63	0.1314	0.0391	69.48
1.2	0.0910	0.0238	72.97	0.1077	0.0280	73.36	0.1988	0.0519	73.18
1.1	0.1205	0.0290	72.72	0.1398	0.0339	72.12	0.2603	0.0630	72.40
1.0	0.1484	0.0336	70.31	0.1661	0.0386	68.55	0.3145	0.0721	69.37
0.9	0.1740	0.0374	66.56	0.1947	0.0435	64.08	0.3687	0.0810	65.23
0.8	0.1975	0.0407	61.77	0.2163	0.0469	58.75	0.4138	0.0876	60.15
0.7	0.2184	0.0433	56.14	0.2354	0.0496	52.82	0.4538	0.0930	54.37
0.6	0.2340	0.0449	49.75	0.2590	0.0536	46.18	0.4930	0.0985	47.81
0.5	0.2516	0.0470	42.62	0.2781	0.0569	38.91	0.5298	0.1039	40.59
0.4	0.2698	0.0494	34.78	0.3064	0.0621	31.42	0.5762	0.1114	32.91
0.3	0.2879	0.0520	26.43	0.3232	0.0657	23.50	0.6111	0.1177	24.79
0.2	0.3046	0.0548	17.69	0.3504	0.0709	15.73	0.6550	0.1257	16.59
0.1	0.3267	0.0591	8.79	0.3608	0.0735	7.81	0.6875	0.1326	8.24
0.0	0.3106	0.0557	0.00	0.3713	0.0741	0.00	0.6819	0.1298	0.00

Separate plots showing the open-water characteristics of each of the two propellers are presented in Figures 6.44 and 6.45 respectively. Each propeller characteristic is accompanied by corresponding experimental data [36, 37]. The same trend seen in previous cases may be in the aforementioned figures, with the numerical data showing good agreement with the experiments for regions of high efficiency and high advance coefficient. The lower-efficiency region correspond to operating points which are influenced by transient phenomena and need to be modelled using transient simulations. The same trend may be noticed for the open-water characteristic of the total CRP set, show in Fig. 6.46, which was to be expected as the total hydrodynamic performance coefficients are derived from the separate propeller characteristics.

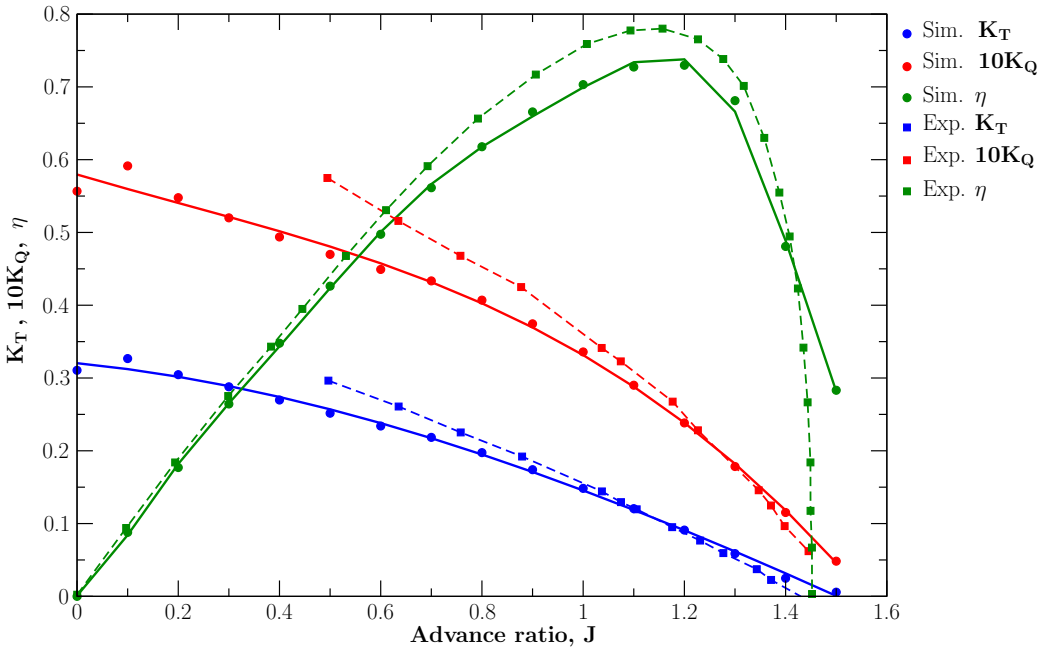

Figure 6.44: `mixingPlane`: Fore propeller steady hydrodynamic coefficients.

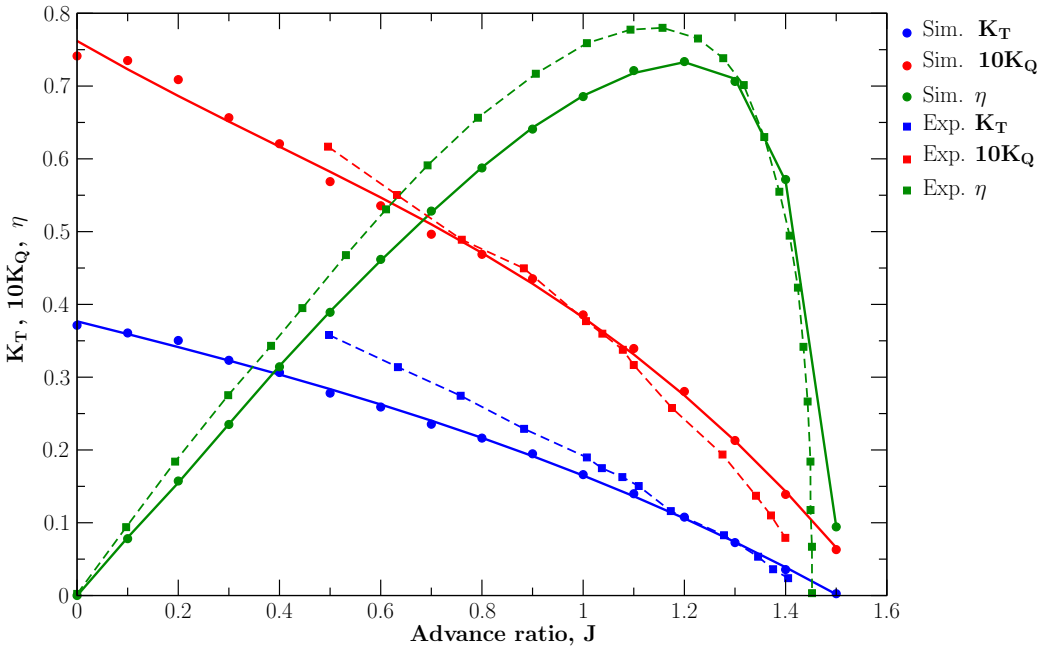

Figure 6.45: `mixingPlane`: Aft propeller steady hydrodynamic coefficients.

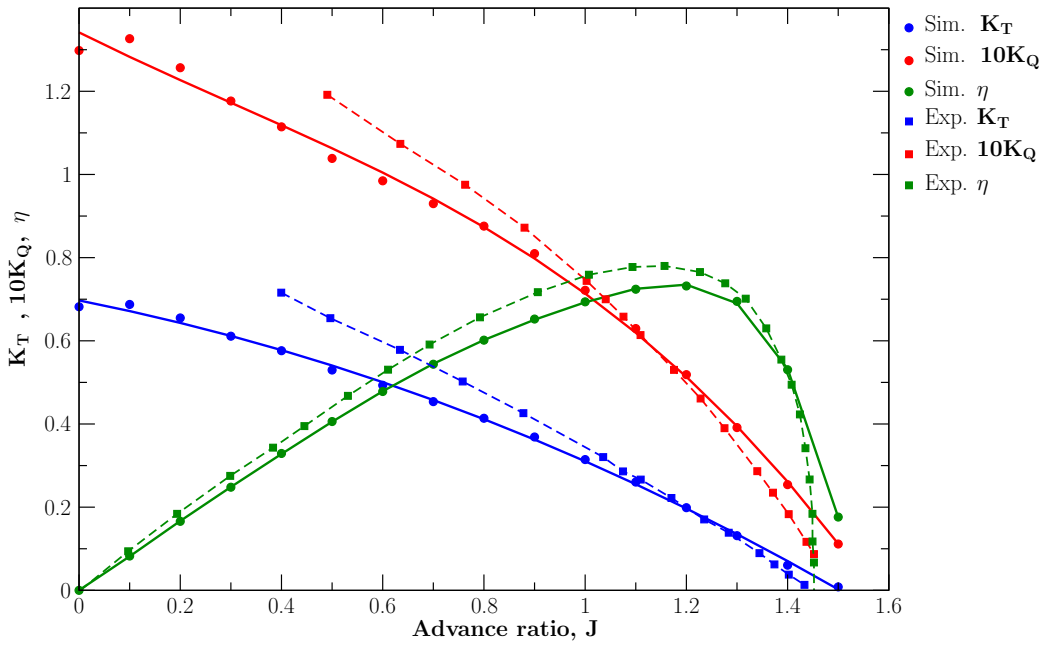

Figure 6.46: `mixingPlane`: Total propeller set steady hydrodynamic coefficients.

Comparison to the `overlapGgi` Interface

A comparison of the hydrodynamic performance coefficients for the same quarter CRP case with the `overlapGgi` and `mixingPlane` interfaces is given next. A plot comparing the two cases with experimental data is given in Figure 6.47. Analysis of the plot reveals that both the `mixingPlane` and the `overlapGgi` cases show good agreement with the experimental data for operating points near the advance coefficient of $J = 1 - 1.2$. For values lower than that, the results of the `mixingPlane` case show better adherence to experimental data. For values of the advance coefficient smaller than 1, the axial velocity diminishes with rising influence of transients on the flow. This is the reason why steady-state numerical data shows poor adherence to experimental values. While both the `mixingPlane` and the `overlapGgi` cases show disagreement with experiments for lower values of J, data from the `mixingPlane` cases follows the trend of the experimental data better.

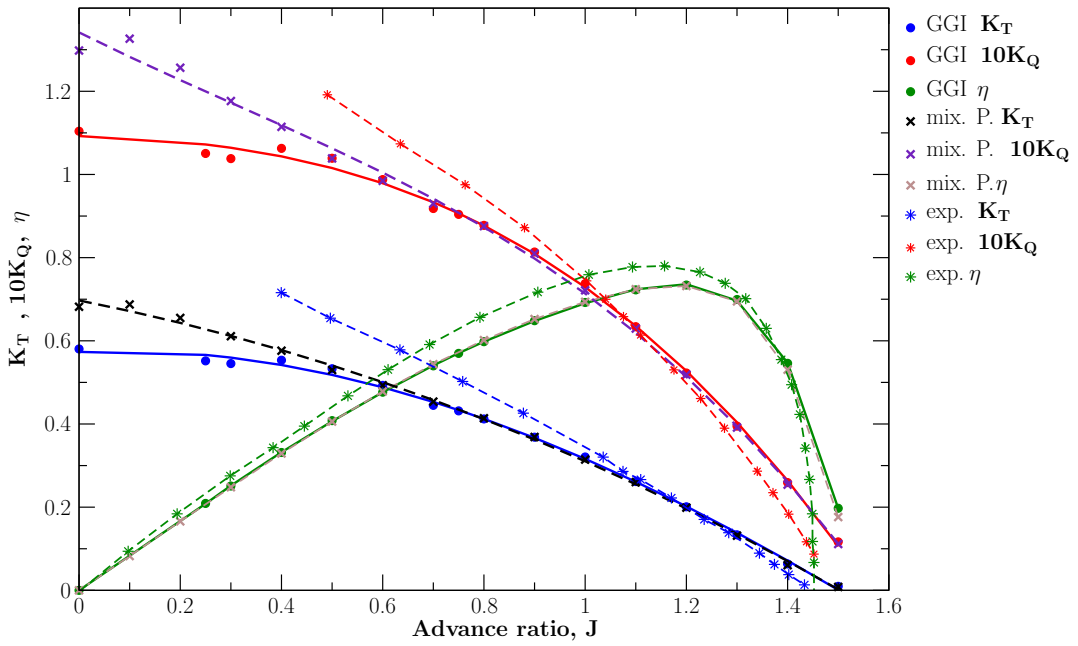

Figure 6.47: `mixingPlane`: Total propeller set steady hydrodynamic coefficients.

6.6. Transient Simulation

The simulations presented in the previous sections handled the CRP domain as a steady-state method. The "frozen rotor" MRF approach is used to specify a rotational zone without actual motion of the mesh. Such results proved satisfactory for higher efficiency operating points residing in regions with weak influence of transient phenomena.

For operating points at lower efficiency, transient phenomena have increasingly pronounced influence on the flow, thus rendering steady-state simulations ineffective, i.e. producing data with increasing deviation from experimental values. This makes it necessary for lower advance coefficient (efficiency) to be modelled using transient simulations.

In this section, data produced from a transient simulation of the CRP set is presented as graphical visualisation of field data and as hydrodynamic performance of the set. As the previous sections, and therein discussed results, validate the use of the quarter CRP domain, thus reducing the computational costs of the simulation. This becomes of great importance for transient simulations, reducing the already high computational time.

The geometry used is the quarter CRP geometry with accompanying domain and necessary boundary conditions, as presented in Chapter 5. Interface are handled by the `cyclicGgi` and `overlapGgi` interfaces. The propeller rotation was modelled by actually rotating the computational mesh in the moving regions. The `DyMesh` dynamic mesh model implemented in `foam-extend` is used. By employment of the aforementioned model rotation is assigned to two mesh regions surrounding the propellers of the CRP set: the FORE propeller region and the AFT propeller region. A constant rotational speed of 12 rps is assigned, taking note that the axis of rotation is aligned with the x-axis of the global coordinate system.

A variant of the `PIMPLE` algorithm, which supports mesh motion (`pimpleDyMFoam`), available in `foam-extend` was used for the transient simulation. A fixed time-step size was chosen and set to a low value to avoid fluctuations of time-varying results which may produce errors in the Fourier Analysis of the numerical data. The chosen time-step $\Delta t = 5e-5$ resulted in high computational time and maximum Courant numbers of $Co \approx 5$. As the `PIMPLE` algorithm allows for larger values of the Co number, the maximum Co values occurring in the simulation were of no concern. It is important to properly resolve transient interaction between propeller blades, that is why approximately 100 time-step per repeating pitch period (one quarter of a full rotation) should be used. Using the chosen time-step size ($\Delta t = 5e-5$) and set rotational speed (12 rps), approximately 1667 time-steps are needed for the transient simulation to complete one full rotation and 417 time-steps for a quarter of a rotation.

Despite the fact that the quarter CRP domain is used, the transient simulation requires considerable computational resources to reach a state of periodic convergence in a reasonable amount of time. For that reason, only one simulation is analysed as a part of this Thesis. The operating point chosen for the transient simulation corresponds to a value of the advance coefficient equal to $J = 0.5$, making the transient results comparable to both the steady-state and the experimental data.

It should be noted that at the time of writing, the transient simulation had run for approximately 0.15 seconds, i.e. 3000 time-steps, with the chosen Δt. As the CRP set rotates at 12 rps, the simulation run-time allowed for only one full rotation of the set which was not enough to reach full periodic convergence. That is why the result presented in continuation, although indicative of the final solution, are susceptible to change as the simulation continues to converge.

6.6.1. Simulation Results

In this section, numerical data from a transient CRP simulation based on the quarter propeller domain is presented. Although the quarter CRP domain was used, the post-processing software enables transformation and copying of the periodically repeating part of the domain, allowing for the full CRP domain to be presented.

The transient simulation spans over a large number of simulated time-steps, making it impossible to present all of the results for each time-step. That is why the results for three distinct time steps are presented, spaced around the point in which the blades of the two propellers pass each other. The first time-step $t = 0.1\,\mathrm{s}$ represents the moment the blades are about to meet, in time-step $t = 0.1025\,\mathrm{s}$ the blade have just met and in time-step $t = 0.1075\,\mathrm{s}$ the propeller blades have already parted.

Pressure Field

Figure 6.48 offers an overview of the kinematic pressure field in the $z = constant.$ plane for three different time-steps. The pressure near the propeller blades shows higher values as the blades move closer (Fig. 6.48 a)) and lower values as the propellers part (Fig. 6.48 b)). As both the higher and the lower pressure areas are situated near the propeller surfaces, a closer look at the pressure distribution on the propeller blades is given in Fig. 6.49. As expected, higher values of pressure over blade surfaces may be seen as the propellers move closer with the average pressure at the blade surfaces dropping after as they separate. Overall, the highest values of pressure are present at the pressure side of the AFT propeller for all time-steps. This is because the AFT propeller suction side suffers most from the wake of the FORE propeller.

Velocity Field

The velocity field is presented as a ratio of axial velocity U_x and the inlet velocity $U_i = 1.8312\,\mathrm{m/s}$. Fig. 6.50 shows the velocity field for the three time-steps, showing consistent values of velocity in the CRP wake and with the only fluctuations happening as blades cut through the $z = const.$ plane used for post-processing. Another analysis of the CRP set wake is offered in form of graphical representation of axial and tangential velocities at $x/R = 0.334$. Distribution of the axial velocity in the wake, presented in Fig. 6.51 shows only small changes throughout the presented time-steps, while more

considerable changes may be noticed for the distribution of tangential velocity. In figures showing axial velocity in the wake, areas of back-flow represented by negative values of the U_x/U_i ratio may be seen. Back-flow may be noticed at blade tips (Fig 6.51) and at the suction side of the AFT propeller (Fig. 6.50).

Turbulence and Vorticity

The distribution of TKE in the CRP wake for the three selected time-steps is shown in figure 6.52. Similarly to the velocity field, the TKE field in the $z = const.$ plane shows only slight temporal variations which are concentrated at the propeller blades, thus requiring examination of TKE distribution over the blade surfaces. Such distribution is offered in Fig. 6.53. The highest values of TKE may be noticed at the leading edges just before and at the moment the propellers meet.

The same as for the steady-state simulations, the Q-criterion is used to visualise vorticity in the region surrounding the propeller set for transient simulations. Q-contours corresponding to the value of $Q > 5 \cdot 10^5$ were used to provide better visibility of propeller interaction. The contours coloured by values of the velocity magnitude are presented in Figure 6.54. Areas of increased vorticity may be noticed in the region between the two propellers just as the propeller move past each other 6.54 b).

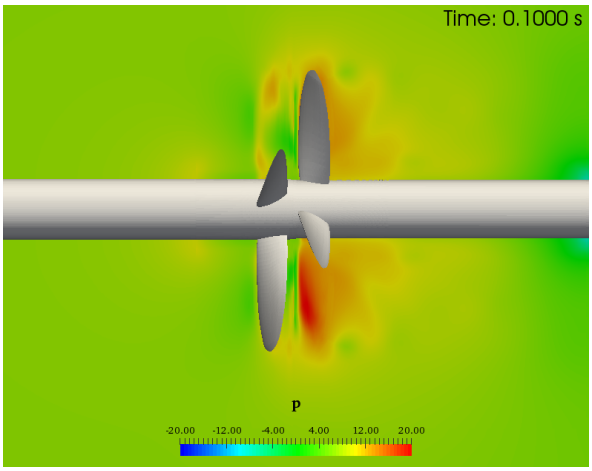

a) Time $t = 0.1\,\mathrm{s}$

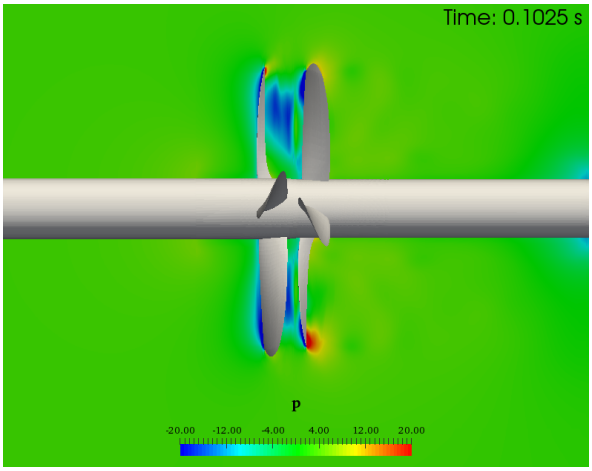

b) Time $t = 0.1025\,\mathrm{s}$

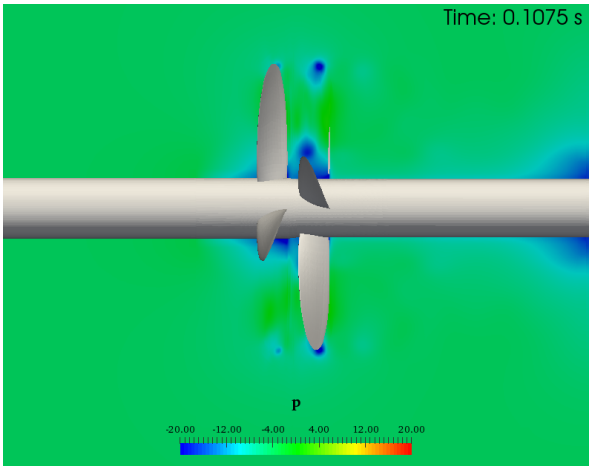

c) Time $t = 0.1075\,\mathrm{s}$

Figure 6.48: Pressure field in $z = const.$ plane for transient simulation of CRP.

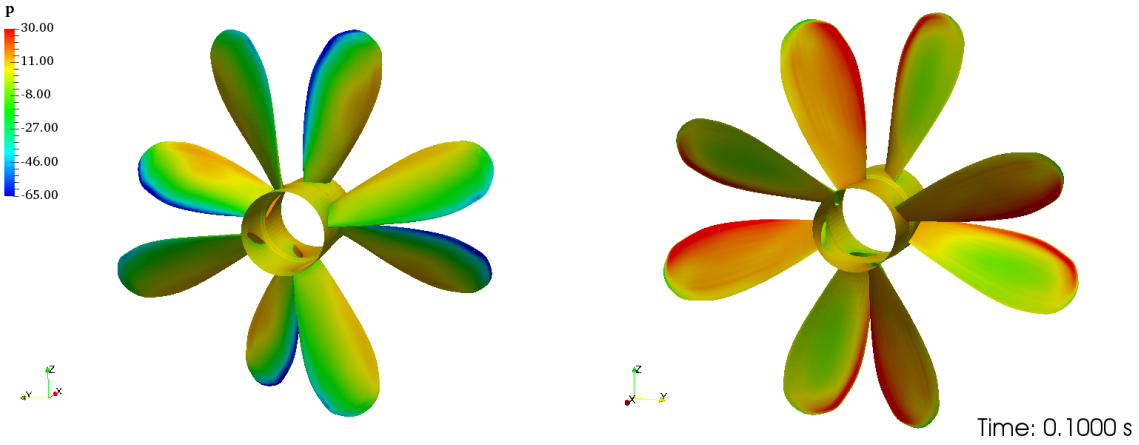

a) Time $t = 0.1\,\mathrm{s}$

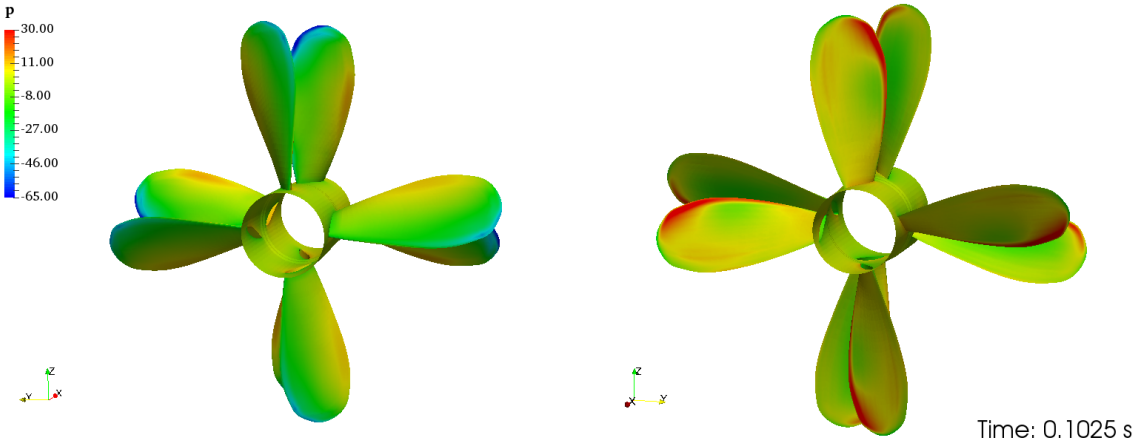

b) Time $t = 0.1025\,\mathrm{s}$

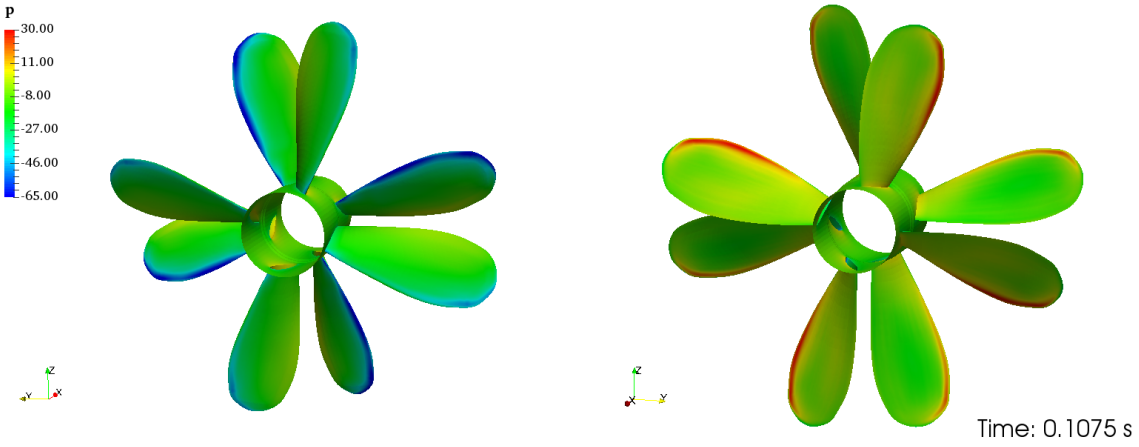

c) Time $t = 0.1075\,\mathrm{s}$

Figure 6.49: Pressure distribution on propeller surfaces for transient simulation of CRP.

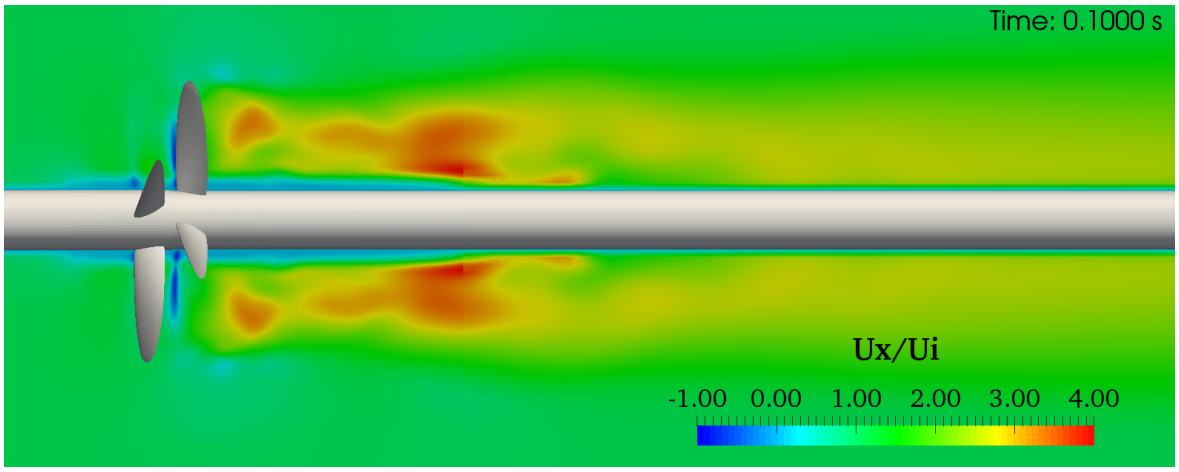

a) Time $t = 0.1\,\mathrm{s}$

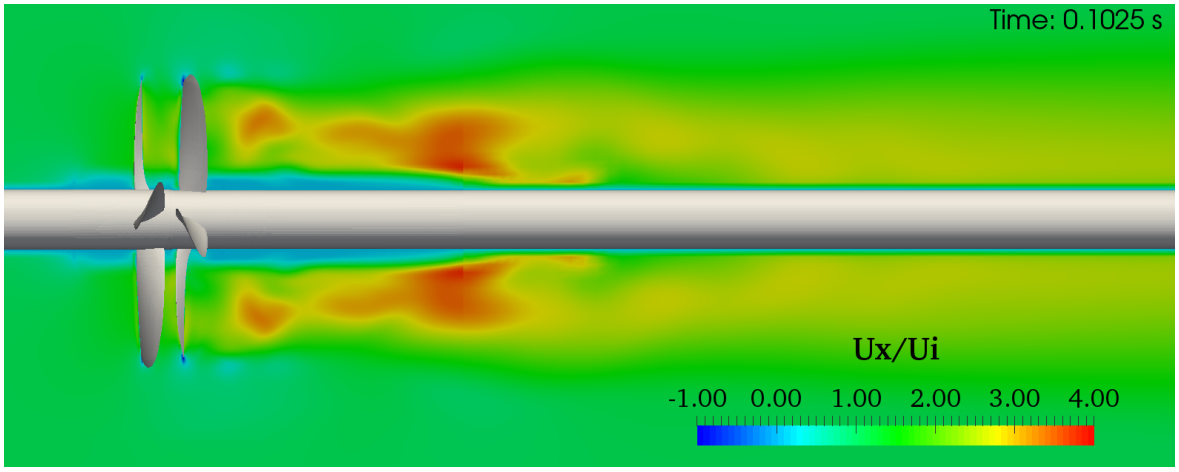

b) Time $t = 0.1025\,\mathrm{s}$

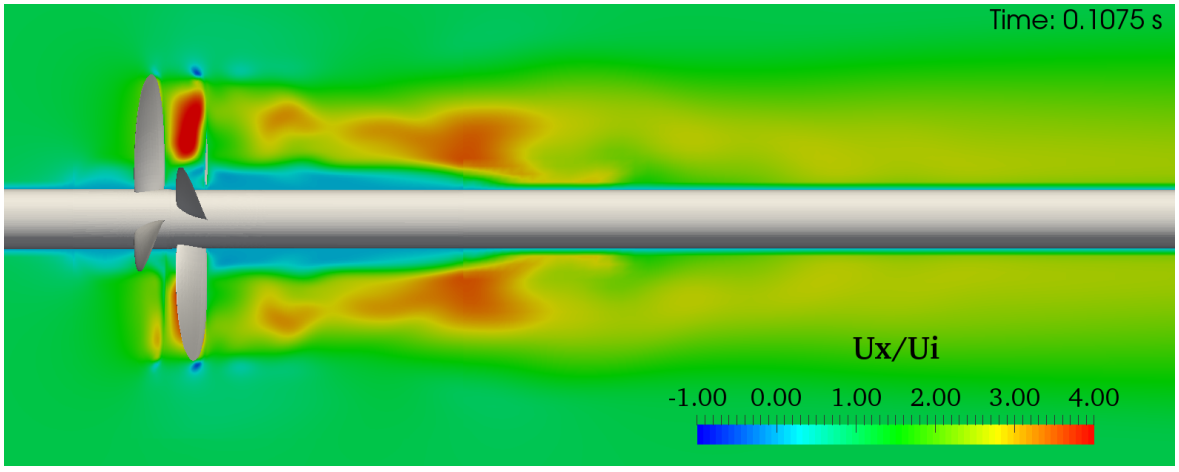

c) Time $t = 0.1075\,\mathrm{s}$

Figure 6.50: Velocity field in $z = const.$ plane for transient simulation of CRP.

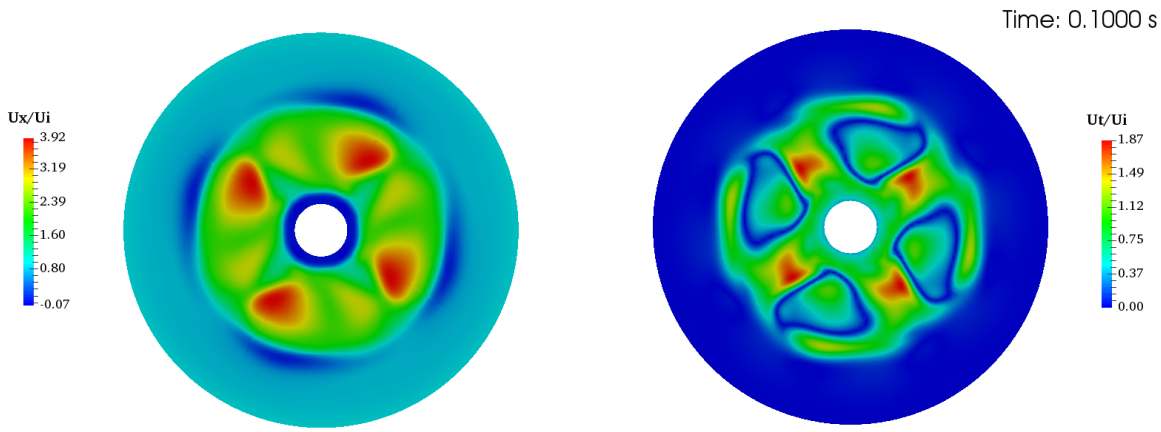

a) Time $t = 0.1\,\mathrm{s}$

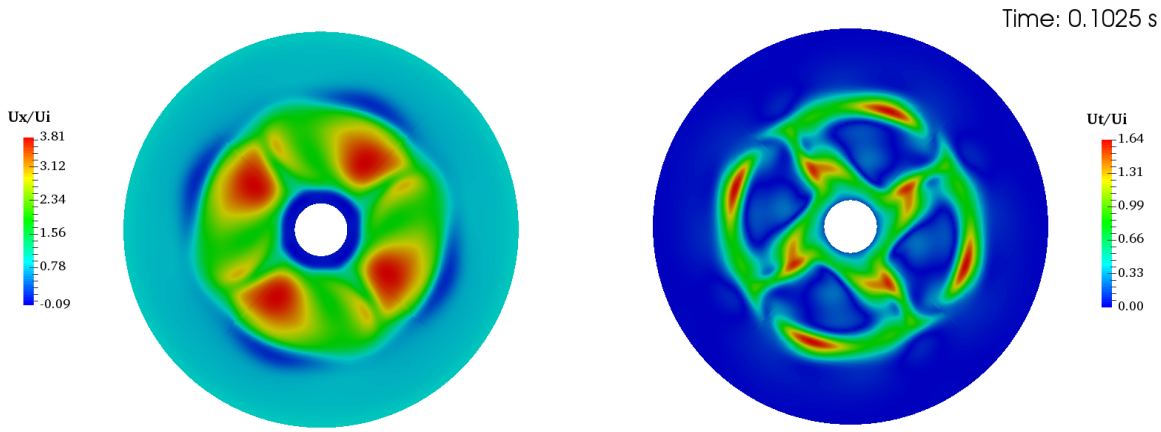

b) Time $t = 0.1025\,\mathrm{s}$

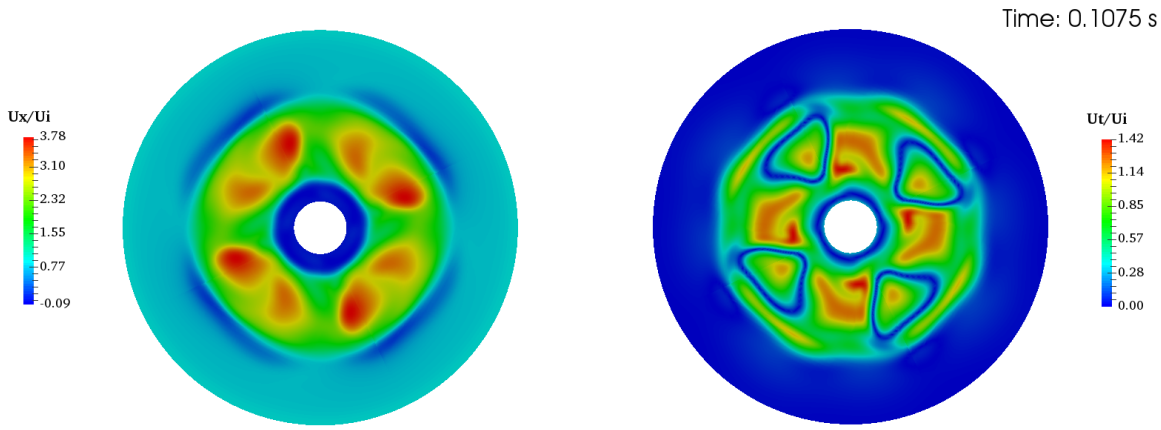

c) Time $t = 0.1075\,\mathrm{s}$

Figure 6.51: Axial and tangential velocity at $x/R = 0.334$ for trans. sim. of CRP.

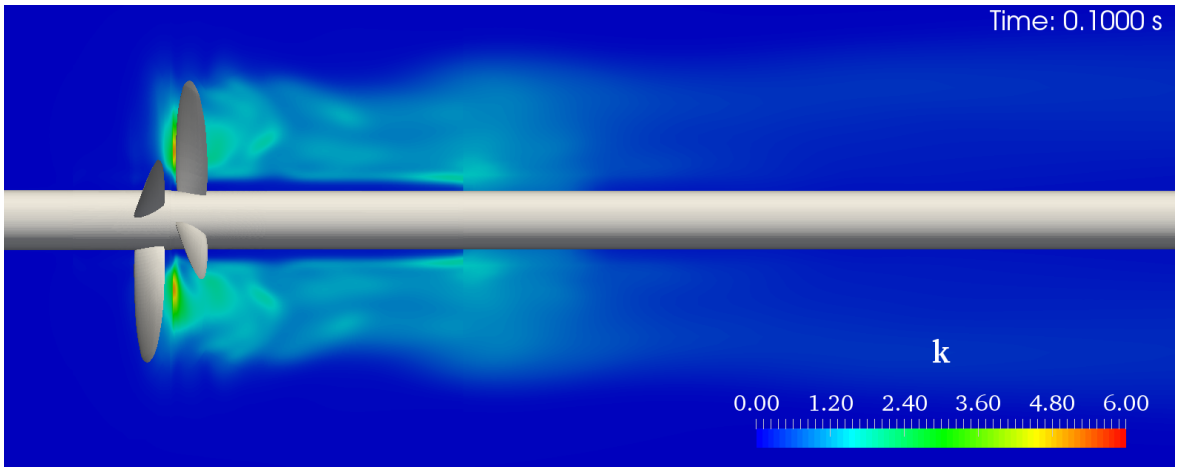

a) Time $t = 0.1\,\mathrm{s}$

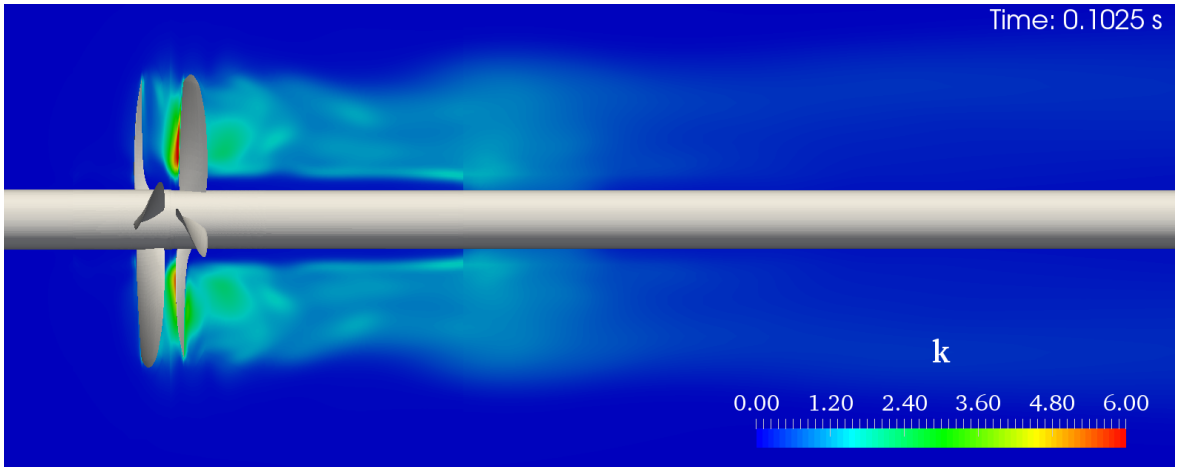

b) Time $t = 0.1025\,\mathrm{s}$

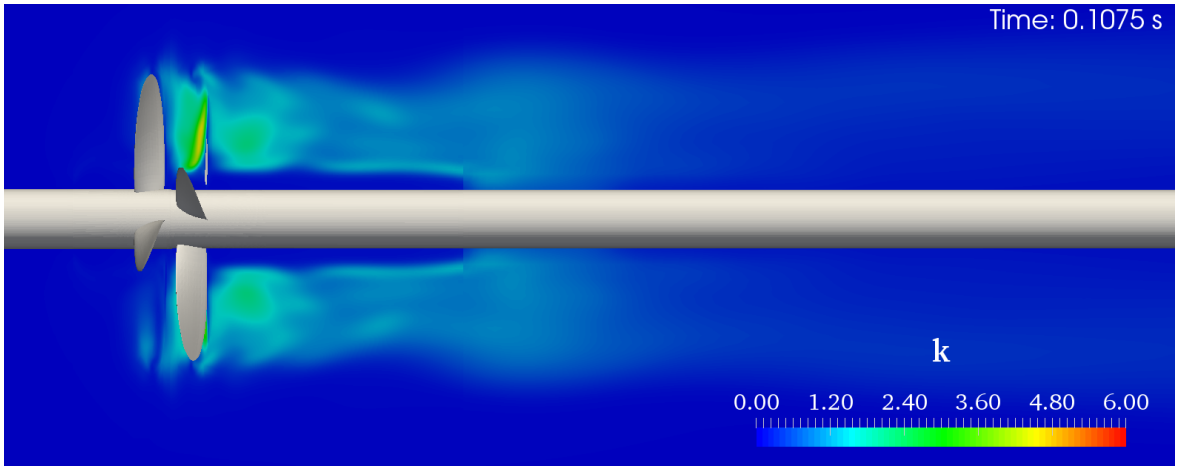

c) Time $t = 0.1075\,\mathrm{s}$

Figure 6.52: TKE in $z = const.$ plane for transient simulation of CRP.

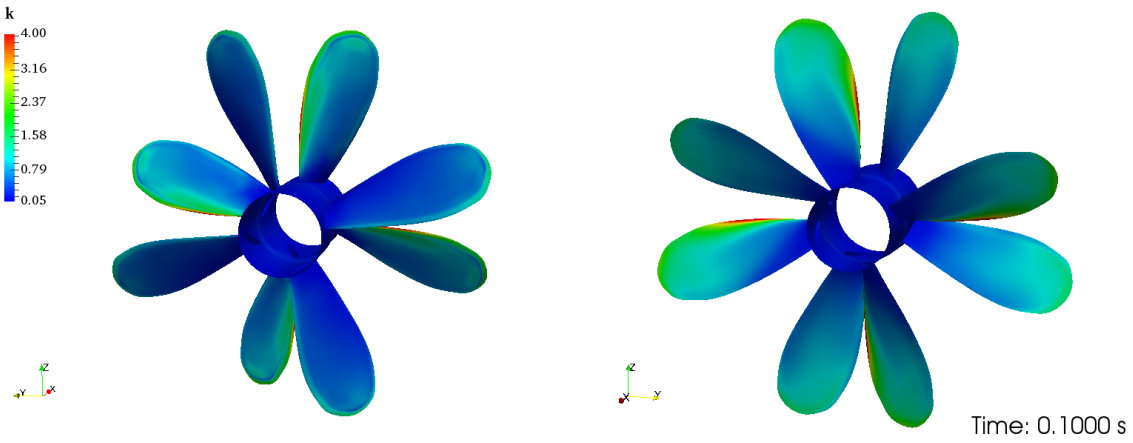

a) Pressure and suction side at time $t = 0.1\,\mathrm{s}$

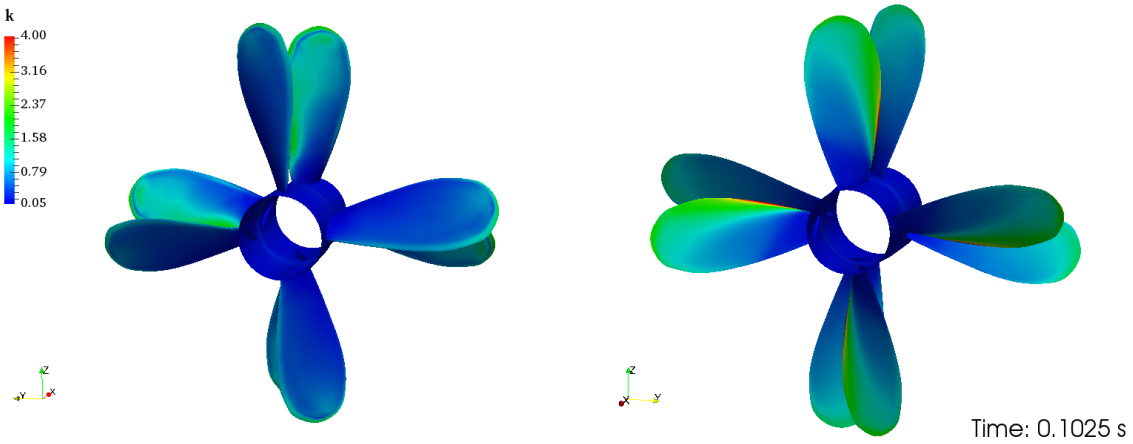

b) Pressure and suction side at time $t = 0.1025\,\mathrm{s}$

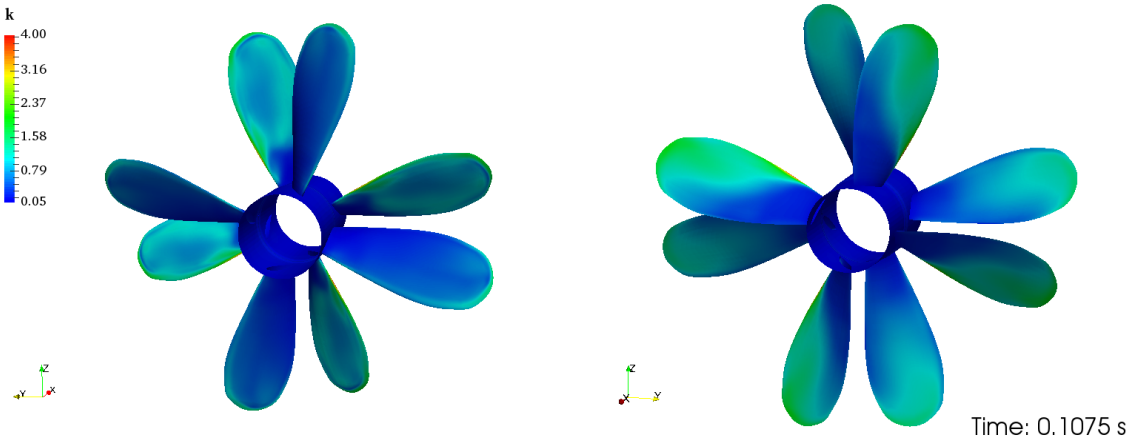

c) Pressure and suction side at time $t = 0.1075\,\mathrm{s}$

Figure 6.53: Distribution of TKE on prop. blades for transient simulation of CRP.

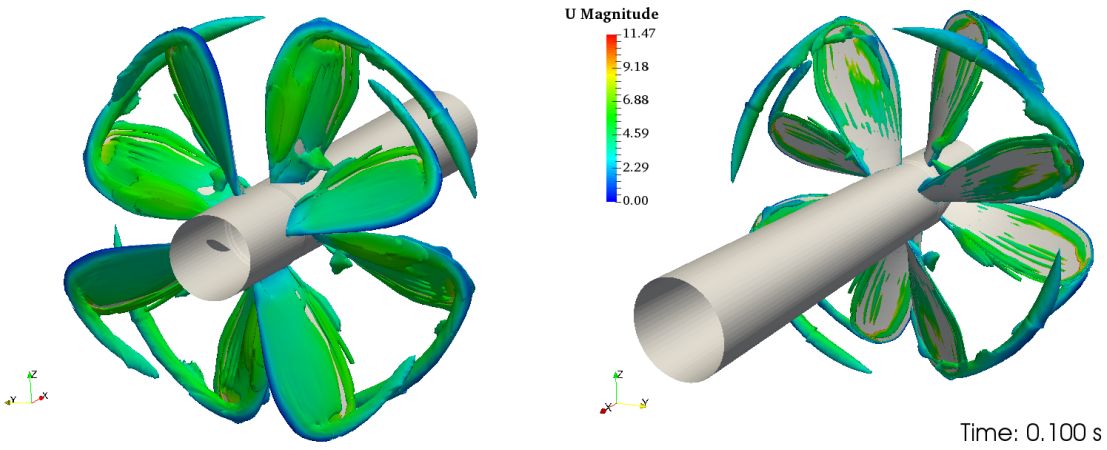

a) Time $t = 0.1\,\mathrm{s}$

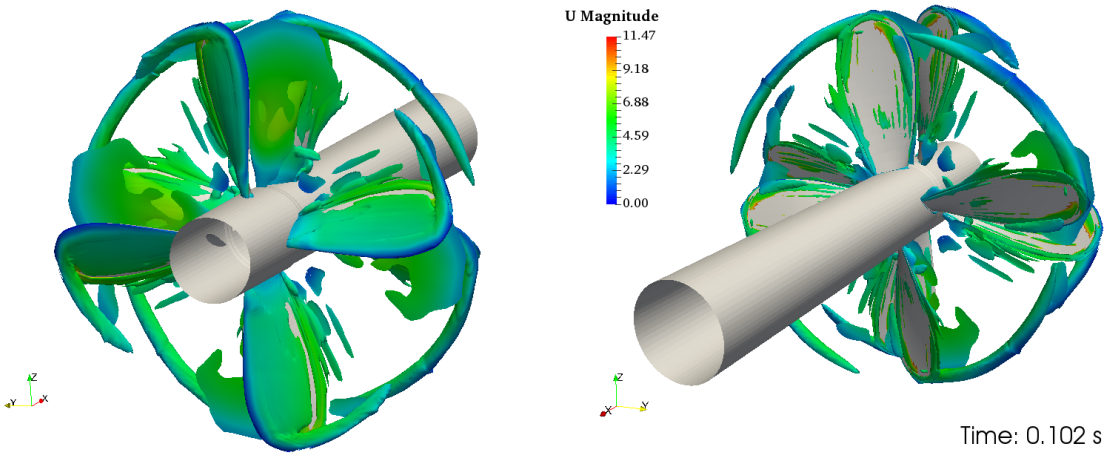

b) Time $t = 0.1025\,\mathrm{s}$

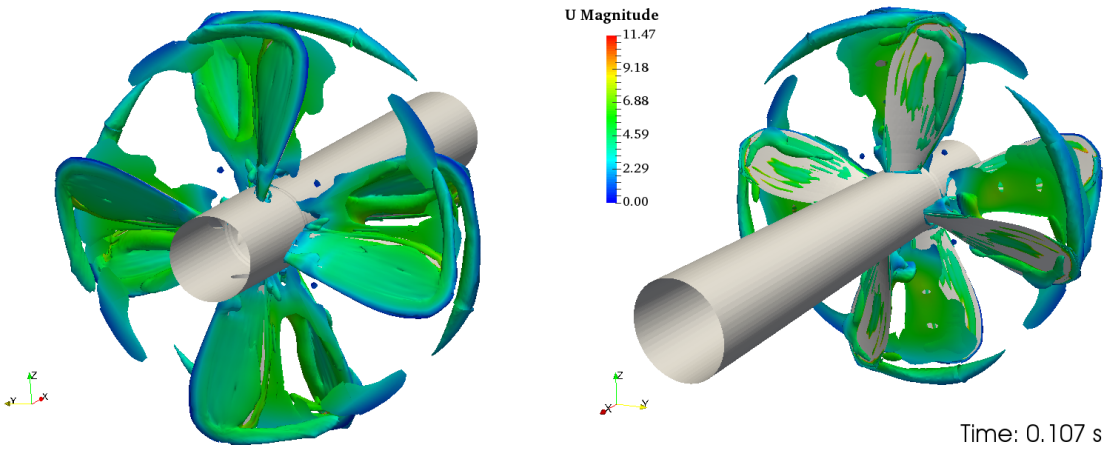

c) Time $t = 0.1075\,\mathrm{s}$

Figure 6.54: Vortices matching Q-criterion $Q > 5 \cdot 10^4$, transient CRP.

6.6.2. Hydrodynamic Performance

Comparison of the hydrodynamic performance data for operating points $J = 0.5$ and $J = 1.1$, presented in Table 6.3, leads to the conclusion that transient simulations are necessary to accurately calculate hydrodynamic performance coefficients for operating points with lower values of the advance coefficients J. As transient simulation are computationally more demanding than steady-state MRF simulation, performance for only one operating point shall be analysed ($J = 0.5$).

The transient solver produces new solutions for each time-step, resulting in time-varying data. The Direct Fourier Transform (DFT) based on equally spaced time intervals was used to analyse time dependent values of force and torque produced by the simulation. Time-varying values of thrust and torque of each propeller and the whole CRP set for one complete rotation, with data transformed by using DFT, are shown in Figures 6.55, 6.56 and 6.57.

By transferring time dependent data to the frequency domain using DFT, values of thrust and torque may be analysed more easily. The base amplitudes in the frequency domain represent mean values of thrust/torque and may be use to calculate steady hydrodynamic coefficients. Such values may be compared results from steady-state simulations. As expected, the appearance of unsteady components of thrust and torque may be seen at eight times shaft frequency ($N = 8$). The frequency at which unsteady components occur is equal to the product of the number of propeller blades, number of propellers in the set and the propeller rotation speed in rps: $4 \cdot 2 \cdot 12 = 96\,Hz$. Values of unsteady thrust and torque may be used with equations presented in Chapter 4. to calculate the unsteady hydrodynamic performance coefficients. Both steady and unsteady coefficients for the whole CRP set are given tabularly:

Table 6.6: Unsteady hydrodynamic performance coefficients.

	Transient		**Transient***		**Experimental**
	Value	Error [%]	Value	Error [%]	**data**
$\mathbf{K_T}$	0.8456	-22.71	0.6891	-5.12	0.6538
$\mathbf{K_Q}$	0.1461	-18.24	0.1170	2.10	0.1194
η	0.4609	-5.46	0.4689	-7.07	0.4357
$\widetilde{\mathbf{K}}_\mathbf{T}$	0.1902	-	0.1655	-	-
$\widetilde{\mathbf{K}}_\mathbf{Q}$	0.0328	-	0.0284	-	-
* Unrevised, near periodic convergence.					

Table 6.6 presents the data for two transient simulations. The first simulation is the final variation with revised setting and boundary conditions showing consistent values for the analysed data fields. The other simulation, which is denoted by the superscript *, showed some inconsistencies in the pressure distribution prompting revision of boundary conditions for pressure at the outlet. The transient simulation with revised boundary conditions shows large errors when compared to experimental data. This is due to the fact that the revised simulation did not achieve periodic convergence because of insufficient runtime, with the simulated CRP set managing to complete only one full rotation. It is believed that as the simulation continues and better convergence is achieved, the relative error will diminish greatly. This is supported by the fact that the unrevised simulation, which was allowed more runtime and managed to achieve several full propeller rotations, shows good agreement with experimental data. The revised simulation is expected to achieve the same or even better agreement with experimental data.

It should also be noted that no error estimation of unsteady thrust and torque coefficients was given in Table 6.6. The reason why the comparison of numerical and experimental values of unsteady coefficients could not be presented is lack of experimental data for these coefficients at $J = 0.5$. It should also be noted that both experimental studies performed by Miller `Miller76, Miller81` suffer from high measuring errors. The author predicts the error to be as high as 20% for total CRP set values and 10% for individual thrust and torque values.

Furthermore, the converged results of the unrevised simulation point to the fact that the transient simulation for $J = 0.5$ produces hydrodynamic coefficients which are closer to the experimental values than those of the steady-state MRF simulation, as they are able to encompass the transient effects influencing the solution.

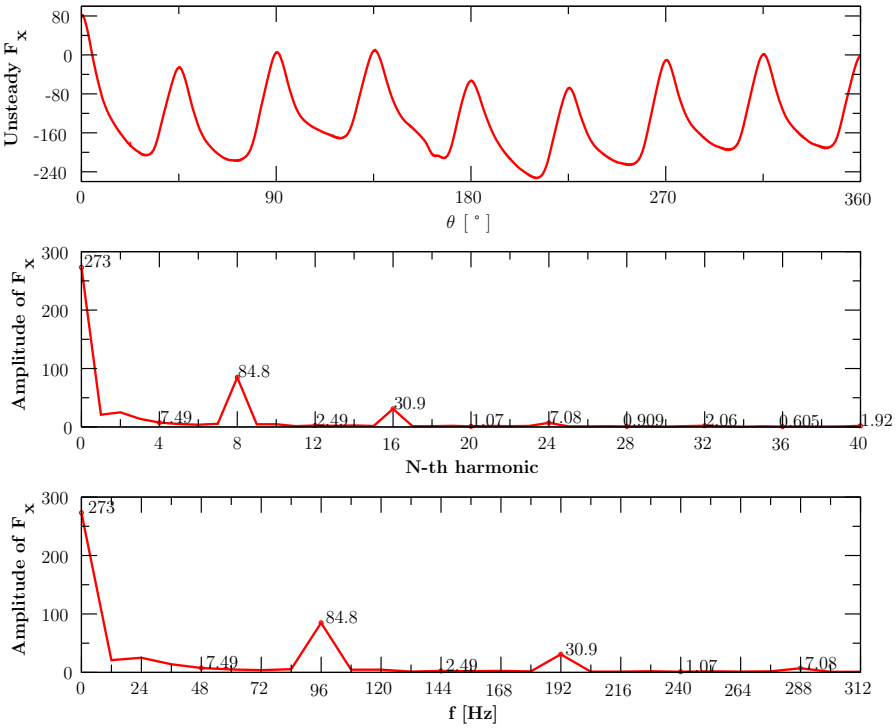

a) Unsteady thrust, $\widetilde{F_x}$

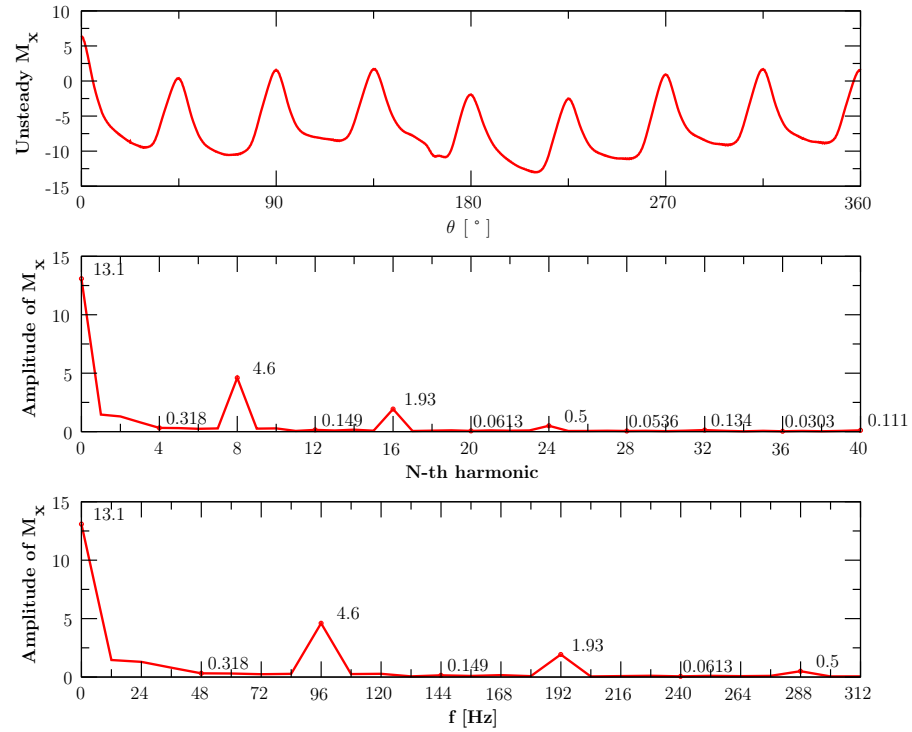

b) Unsteady torque, $\widetilde{M_x}$

Figure 6.55: Fore propeller unsteady hydrodynamic performance for $J = 0.5$

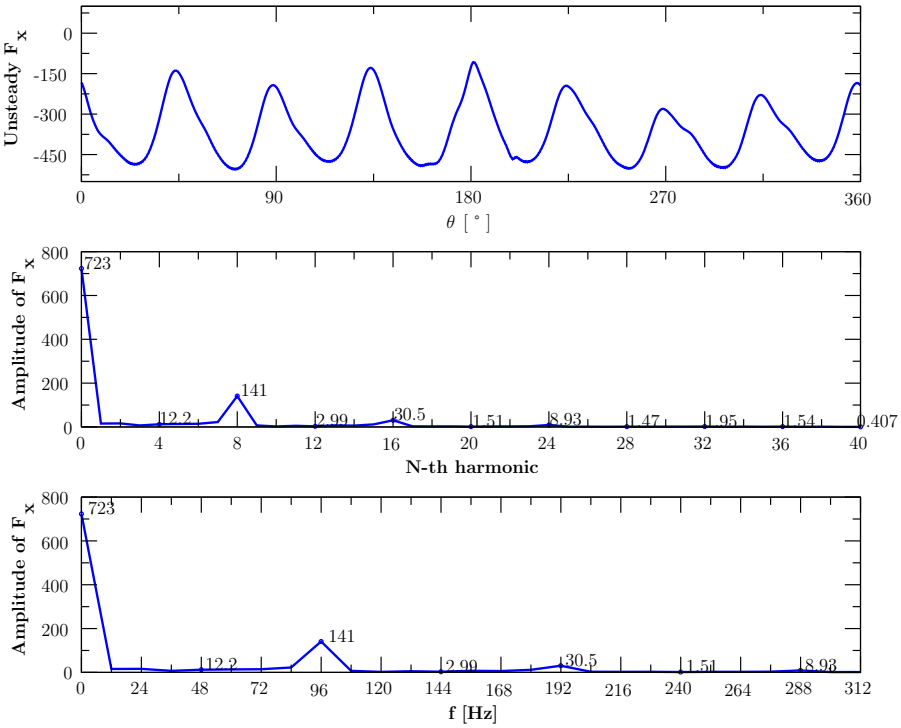

a) Unsteady thrust, $\widetilde{F}_x$

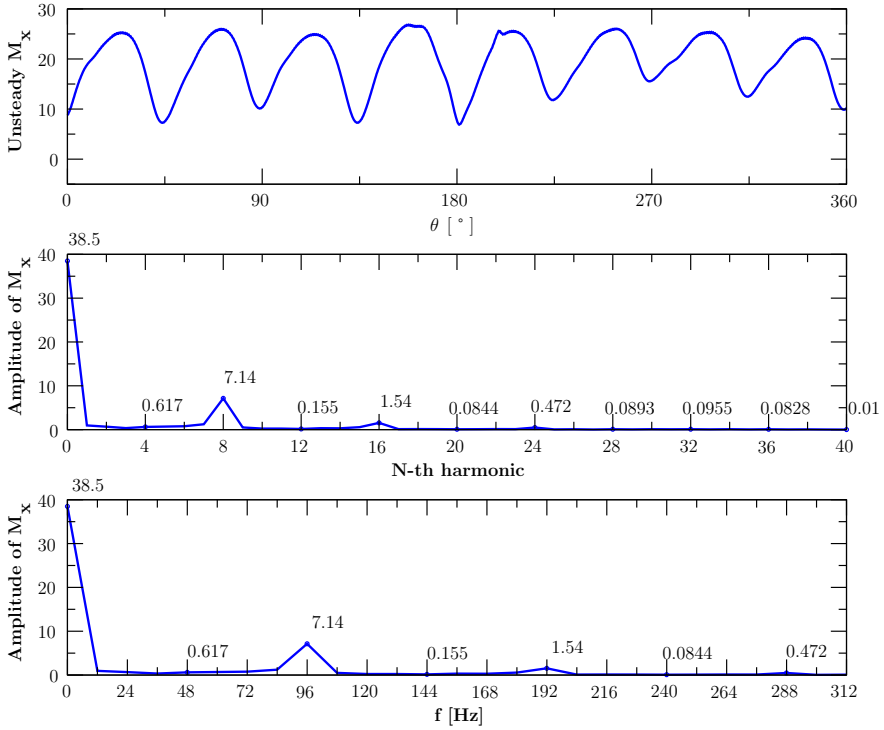

b) Unsteady torque, $\widetilde{M}_x$

Figure 6.56: Aft propeller unsteady hydrodynamic performance for $J = 0.5$

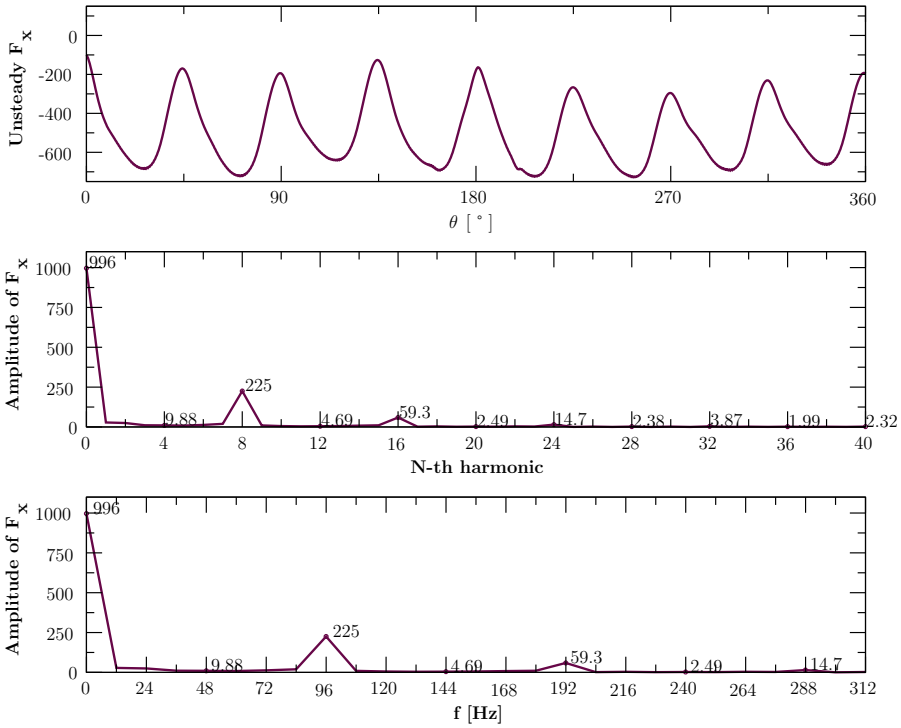

a) Unsteady thrust, $\widetilde{F_x}$

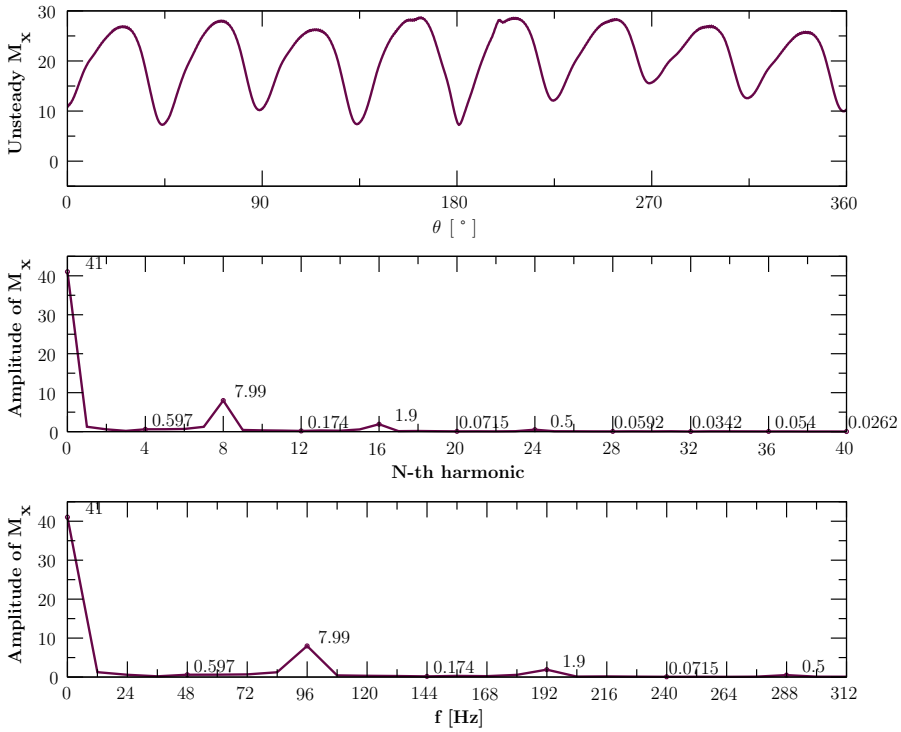

b) Unsteady torque, $\widetilde{M_x}$

Figure 6.57: Total CRP unsteady hydrodynamic performance for $J = 0.5$

6.7. Closure

In this chapter the results of several different simulations of CRP were presented in hope of analysing the different choices in regard to interface and domain handling. First, the results of quarter and full CRP domain simulations were analysed showing no major differences. This validated the `overlapGgi` and `cyclicGgi` interfaces, thus allowing for further use of the smaller quarter CRP case and positively affecting simulation runtime. Secondly, an overview of the differences between the `mixingPlane` and the `overlapGgi` interfaces was investigated and presented both graphically and in term of numerical values. Thirdly, a comparison between transient and steady-state simulation of the CRP set was offered, commenting on the results. Lastly, steady-state simulations were conducted to analyse the influence of different initial propeller positions on steady hydrodynamic coefficients.

The next chapter serves as conclusion of the Thesis, offering an overview of completed task, the resulting findings and possible future work on the subject of CRP.

7 Conclusion

7.1. Conclusion

This Thesis covered an overview of interface handling methods used to establish rotor-stator interaction in CFD simulations. An introduction was given explaining the complexity of various turbomachines, acknowledging the need to simplify their geometry when performing CFD simulations. The `mixingPlane` and `ggi` interfaces were introduced, with additional explanation of two `ggi` variants: the `overlapGgi` and `cyclicGgi` interfaces. The interfaces were established as means of providing communication between partially connected or disconnected mesh regions, thus enabling the use of simplified, partial geometry, computational domains. The theoretical part of the thesis was expanded to include practical examples of these interfaces using numerical simulations of a CRP set, performed in `foam-extend`.

A series of CRP steady-state simulations was performed for an operating point determined by the propeller advance ratio $J = 0.5$. First, baseline results were established using a full CRP geometry with the `Ggi` interface. Secondly, a quarter CRP simulation using a combination of the `cyclicGgi` and `overlapGgi` interfaces was performed, with the results validated against those of the full geometry simulation. Thus, further use of the quarter CRP simulation was made possible, saving on computational runtime needed to reach convergence of results. Several steady-state simulations were performed to study the effects of different initial propeller position on resulting hydrodynamic performance data. Once the quarter simulation was validated, the next series of steady-state simulations, aimed at comparing the use of `mixingPlane` and `overlapGgi` interfaces, was performed. As the `mixingPlane` introduces averaging at the interface,

`overlapGgi` was adopted for ensuing transient simulations, performed for the same operating point $J = 0.5$. The resulting unsteady data was analysed by using DFT and compared to results from previous simulations. The data gathered from both the steady-state and transient simulations was presented graphically and by studying the resulting hydrodynamic performance coefficients, i.e. open-water characteristics of the CRP set.

Conclusions made possible by analysis of numerical data from various simulations performed on the CRP set are presented next. Firstly, the open-water characteristic resulting from the full CRP simulations shows the best efficiency point (BEP) of the set to be around the advance coefficient values of $J = 1.2-1.3$. The data showed higher values of torque and thrust on the AFT propeller of the set, which was expected because the second propeller is influenced by the wake of the FORE propeller. Steady-state hydrodynamic coefficients show good agreement with experimental data for operating points near the BEP, with some disagreement for both lower and higher values of J. The explanation being that, as the CRP operating point moves farther away from the BEP, transient effects become more pronounced making the steady-state approach unable to produce fully accurate data. For accurate results of such operating points, transient simulations should be performed. Nevertheless, steady-state simulations provide accurate data for higher efficiency operating points, which are generally used for propeller design.

The second series of simulations focused on verifying the validity of quarter geometry CRP simulations. Both the data field analysis and hydrodynamic performance coefficients showed no major deviations when compared to full CRP simulation results. This lead to the conclusion that the `overlapGGi` and `cyclicGgi` interfaces, used in the quarter simulation, function as expected and described in the theoretical part of the Thesis. This fact has a highly positive impact on simulation runtime and computational demands, allowing for a smaller number of cells in the computational domain by replacing the full propeller domains with quarter domains. Cases based on the quarter domain and the `mixingPlane` interface produce hydrodynamic performance data with similar behaviour in the higher and lower efficiency regions as the simulations based on the `overlapGgi` and `Ggi` interfaces, with some differences for low values of J. More specifically, the `mixingPlane` cases seem to follow the experimental data curve slightly better, but no difference high enough to justify further use of the `mixingPlane` interface over `ggi` was noticed. As the `mixingPlane` performs averaging of data at the interface,

which can be seen in graphical representations of various data fields, it is not suitable for use in transient simulations, as it would average out the unsteady data affecting the validity of the simulations. The other two interfaces may be used for both steady-state and transient simulations.

Transient simulation of the CRP set offered several insights into propeller behaviour. Analysis of resulting transient data fields and unsteady values of force and thrust showed the values to be time-dependant and influenced by propeller interaction. Considering the values of unsteady thrust, changes in thrust may be noticed as the propeller rotates and the blades pass each other. Furthermore, the appearance of unsteady component of thrust and torque was noticed at eight times shaft frequency ($N = 8$). As the propellers rotate synchronous to each other and have the same number of blades, the unsteady components may be attributed to propeller interaction. Fourier transformation of transient data allowed for calculation of steady and unsteady hydrodynamic performance coefficients, which were compared to both steady-state simulation results and experimental data. The previously postulated theory explaining how the steady-state results disagree with experimental data for lower values of J because of the inability of steady simulations to capture transient phenomena, was validated by transient data. The data showed very good agreement with the experiments even for a lower efficiency operating point $J = 0.5$, when enough time is allowed for the transient simulation to reach a periodic steady state.

Finally, it is concluded that steady state simulations provide sufficiently accurate results for high efficiency operating points. If low efficiency regions are to be modelled, transient simulations should be performed. A major issue regarding transient simulations is high turnaround time in combination with high computational costs. This makes transient simulations of little use for practical application when modelling CRP sets, even with quarter domain simulations, and makes steady-state methods such as MRF viable alternative for certain operating points.

All things considered, turbomachines prove to be complex machines which require various simplifications for practically usable CFD simulations. These simplifications may be offered in form of different interface and domain handling methods which depend on the problem and the geometry that is to be analysed. A contra-rotating propeller set proved a good example of a turbomacine on which various approaches to interface and domain handling could be studied.

7.2. Future Work

A possible continuation of the work in this Thesis would consist of running more transient simulations on both lower and higher efficiency operating points and repeating the analysis of the existing transient simulation after a satisfactory periodic steady state had been achieved.

Furthermore, a study of the effects of different axial spacing of propellers forming the CRP set would provide interesting data from both steady-state and transient simulations. The data would be comparable to experimental values, as the required experimental data already exists for the same CRP set as the one used in this Thesis. Similar research could be conducted on CRP sets with different rotational speed and/or different number of blades for each propeller in the set.

Lastly, the insights on propeller interaction, case set-up and data analysis gathered while working on simulations of a maritime CRP set could be used to further the research to include CRP used in aviation.

Appendices

A Interface Set-up Examples

Appendix A offers several examples of boundary file entries for different interface types. All entries are based on set-up files used in working CRP simulations and with existing patches described in Ch. 5.

A.1. ggi

An example of the code used to define an `Ggi` patch in the `boundary` file found in `case_dir/constant/polymesh`, with accompanying explanation.

```
AFT_interface_back
  {
      type            ggi;
      nFaces          3712;
      startFace       6401114;
      shadowPatch     MAIN_interface_back;
      zone            AFT_back_zone;
      bridgeOverlap   true;
  }
```

- `type` - Defines type of boundary patch.
- `nFaces, startFace` - Internally defined with mesh.
- `shadowPatch` - GGI patch pair should be defined.
- `zone` - Name of the faceZone analogous to the GGI patch being defined.
- `bridgeOverlap` - If set to `false` completely and partially uncovered faces are disallowed. When set to `true` for cases with non-overlapping cases, a slip boundary condition is defined (preferably use `overlapGgi`).

A.2. overlapGgi

An example of the code used to define an `overlapGgi` patch in the `boundary` file found in `case_dir/constant/polymesh`, with accompanying explanation.

```
FORE_interface_front
    {
        type            overlapGgi;
        nFaces          2320;
        startFace       6358544;
        shadowPatch     FT_interface_front;
        zone            FORE_front_zone;
        bridgeOverlap   false;
        rotationAxis    (1 0 0);
        nCopies 4;
    }
```

- `type` - Defines type of boundary patch.
- `nFaces, startFace` - Internally defined with mesh.
- `shadowPatch` - GGI patch pair should be defined.
- `zone` - Name of the faceZone analogous to the GGI patch being defined.
- `bridgeOverlap` - Should be set to `false` for `overlapGgi`.
- `rotationAxis` - Defines the axis of rotation.
- `nCopies` - Set exact number of patch copies needed for defining a full geometry (360°) .

A.3. cyclicGgi

An example of the code used to define an `cyclicGgi` patch in the `boundary` file found in `case_dir/constant/polymesh`, with accompanying explanation.

```
FORE_cyclic
  {
      type            cyclicGgi;
      nFaces          5064;
      startFace       6369274;
      shadowPatch     FORE_cyclic_shadow;
      zone            FORE_cyclic_zone;
      bridgeOverlap   false;
      rotationAxis    (1 0 0);
      rotationAngle   90;
      separationOffset (0 0 0);
  }
```

- `type` - Defines type of boundary patch.
- `nFaces, startFace` - Internally defined with mesh.
- `shadowPatch` - GGI patch pair should be defined.
- `zone` - Name of the faceZone analogous to the GGI patch being defined.
- `bridgeOverlap` - Should be set to `false` for `cyclicGgi`.
- `rotationAxis` - Defines the axis of rotation.
- `rotationAngle` - Sets the rotation angle, i.e. degrees of rotation around the `rotationAxis` need to match with the corresponding `shadowPatch`.
- `separationOffset` - Used for cyclic patches with transitions.

A.4. mixingPlane

An example of the code used to define `mixingPlane` patches in the `boundary` file found in `case_dir/constant/polymesh`, with accompanying explanation.

```
FORE_interface_side
  {
      type            mixingPlane;
      nFaces          6090;
      startFace       6363184;
      shadowPatch     MAIN_interface_side1;
      zone            FORE_side1_zone;
      coordinateSystem
      {
            type            cylindrical;
            name            mixingCS;
            origin          (0 0 0);
            axis            (1 0 0);
            direction       (0 1 0);
            inDegrees       false; //radians
      }
      ribbonPatch
      {
            sweepAxis       Theta;
            stackAxis       Z;
            discretisation  bothPatches;
      }
  }
```

- `type` - Defines type of boundary patch.
- `nFaces, startFace` - Internally defined with mesh.
- `shadowPatch` - mixingPlane patch pair should be defined.
- `zone` - Name of the faceZone analogous to the mixingPlane patch being defined.

coordinateSystem

- `type` - Defines the coordinate system used for defining mixingPlane ribbon patches. Available types are: `cylindrical, ellipticCylindrical, parabolicCylindrical, spherical` and `toroidal`.
- `name` - Defines the name of the coordinate system.
- `origin` - Defines the origin of the mixingPlane coordinate system in relation to global coordinates.
- `axis` - Set the axis of rotation used.
- `direction` - Sets the direction in which the averaging will be performed.
- `inDegrees` - Set to `true` for degrees or to `false` for radians.

ribbonPatch

- `sweepAxis` - Defines the sweeping axis for averaging in chosen the mixingPlane coordinate system. In the example above, `Theta` is used as the sweep axis in the cylindrical coordinate system.
- `stackAxis` - Defines the stacking axis in the chosen mixingPlane coordinate system. This example uses `Z` as the stack axis and for defining the manner in which the ribbon patches of the mixingPlane interface are stacked. If, for example, the `FORE_interface_front` patch is used, the stack axis should be set to `R`. Examples of different stack axes are given in Fig. A.1 and A.2.
- `discretisation` - Defines the type of discretisation used. Availabe options are: `bothPatches, uniform, slavePatch, masterPatch` and `userDefined`.

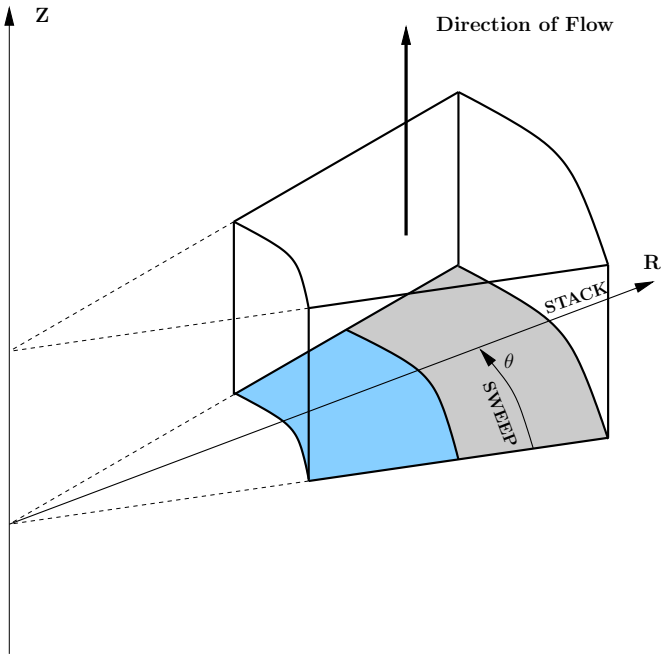

Figure A.1: Use of `mixingPlane` with θ as sweep axis and R as stack axis.

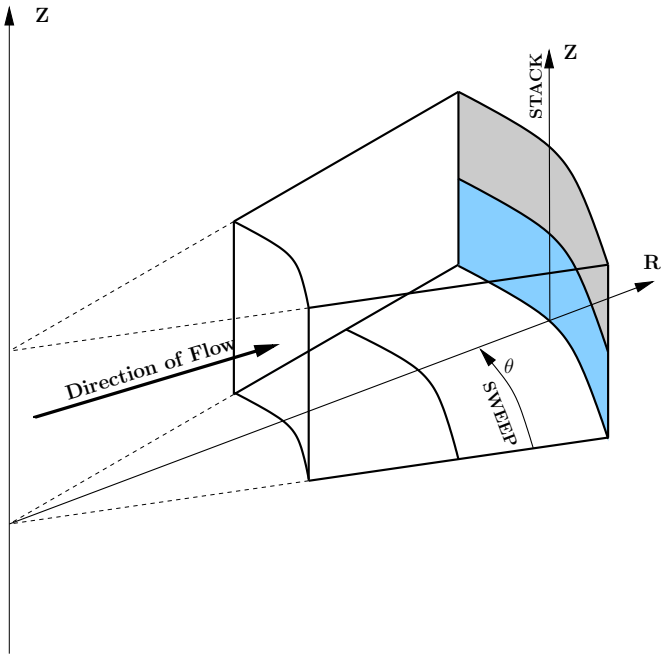

Figure A.2: Use of `mixingPlane` with θ as sweep axis and Z as stack axis.

Bibliography

[1] NauticEXPO. Ship pod drive. `http://www.nauticexpo.com/prod/abb-marine/product-30709-461731.html`. [Online; accessed March 10, 2019].

[2] Volvo Penta. Multiple ways to create different types of propeller solutions. `http://nordicblog.volvopenta.com`. [Online; accessed March 10, 2019].

[3] A. T. Sayers. *Hydraulic and compressible flow turbomachines*. Department of Mechanical Engineering, University of Capetown, 1990.

[4] E. Logan Jr. *Handbook of Turbomachinery*. Marcel Dekker, 2003.

[5] H. Jasak and M. Beaudoin. Openfoam trubo tools: From general purpose cfd to turbomachinery simulations. In *Proceedings of ASME-JSME-KSME Joint Fluids Engineering Conference*, Hamamatsu, Shizuoka, Japan, 2011.

[6] H. Jasak. Course materials for Numerical Methods in Continuum Mechanics Method, February 2018.

[7] S. V. Patankar and D.B. Spalding. A calculation procedure for heat, mass and momentum transfer in three-dimensional parabolic flows. *International Journal of Heat and Mass Transfer*, 15:1787–1806, 1972.

[8] R. I. Issa. Solution of the implicit discretized fluid flow equations by operator splitting. In *Mechanical Engineering Report*, Imperial College, London, UK, 1982.

[9] T. Holzmann. Mathematics, Numerics, Derivations and OpenFOAM, December 2016.

[10] B.E. Launder and D.B. Spalding. The numerical computation of turbulent flows. *Computer Methods in Applied Mechanics and Engineering*, 3:269–289, 1974.

[11] B.E. Launder and B.I. Sharma. Application of the energy-dissipation model of turbulence to the calculation of flow near a spinning disc. *Letters in Heat and Mass Transfer*, 1:131–137, 1974.

[12] David C. Wilcox. *Turbulence Modeling for CFD*. DCW Industries, 1993.

[13] F. Menter and T. Esch. Elements of industrial heat transfer prediction. In *16th Brazilian Congress of Mechanical Engineering (COBEM)*, Uberlandia, Brazil, 2001.

[14] F.R. Menter, M. Kuntz, and R. Langtry. Ten years of industrial experience with the sst turbulence model. *Turbulence, Heat and Mass Transfer*, 4:625–632, 2003.

[15] Nasa turbulence modeling resource. `http://turbmodels.larc.nasa.gov/sst.html`. Accessed: 12-02-2019.

[16] A. Hellsten. Some improvements in menter's k-omega-sst turbulence model. In *29th AIAA Fluid Dynamics Conference*, Albuquerque,NM,USA, 1998.

[17] Gregor Cvijetić. *Steady State Methods for Turbomachinery*. Faculty of Mechanical Engineering and Naval Architecture, University of Zagreb, 2014.

[18] The MRF development. `http://openfoamwiki.net/index.php/See_the_MRF_development`. Accessed: 10-02-2019.

[19] H. Jasak and H. Rusche. Dynamic mesh handling in openfoam. In *Advanced Training at the OpenFOAM Workshop*, Gothenborg, Sweden, 2010.

[20] H. Jasak. Course materials for The Practical Finite Volume Method, February 2018.

[21] H. Jasak and M. Beaudoin. Development of a generalized grid interface for turbomachinery simulations with openfoam. In *Open Source CFD International Conference*, Berlin, Germany, 2008.

[22] H. Jasak. Dynamic mesh handling in OpenFOAM. In *47th AIAA Aerospace Sciences Meeting including The New Horizons Forum and Aerospace Exposition*. American Institute of Aeronautics and Astronautics, jan 2009.

[23] I. E. Sutherland and G. W. Hodgman. Hidden surface removal using polygon area sorting. In *SIGGRAPH '77: Proceedings of the 4th annual conference on Computer graphics and interactive techniques*, New York, USA, 1977.

[24] H. Jasak. General grid interface - theoretical basis and implementation. In *NUMAP-FOAM Summer School*, Zagreb, Croatia, 2009.

[25] M. Beaudoin et al. Evaluation of an improved mixing plane interface for openfoam. *IOP Conference Series: Earth and Environmental Science*, 22:022004, 2014.

[26] H. Jasak and L. Balatinec. CFD Evaluation of Hydrodynamic Performance of Contra-Rotating Propellers (CRP) using OpenFOAM. In press, RINA, 2019.

[27] J. S. Carlton. *Marine Propellers and Propulsion, 3rd ed.* Elsevier, 2012.

[28] P. C. Van Klujiven et. al. *Contra-rotating propellers*. Rotterdam Mainport University of Applied Sciences RMU.

[29] S. Brizzolara et al. Design of contra-rotating propellers for high-speed stern thrusters. *Ships and Offshore Structures*, 2:169–182, 2007.

[30] H. Ghassemi and M. Taherinasab. Numerical calculations of the hydrodynamic performance of the contrarotating propeller (crp) for high speed vehicle. *Polish Maritime Research*, 20:13–20, 2013.

[31] Borna Šeb. Numerical characterisation of a ship propellers. Master's thesis, University of Zagreb, 2017.

[32] H. Jasak, V. Vukčević, I. Gatin, and I. Lalović. CFD validation and grid sensitivity studies of full scale ship self propulsion. *International Journal of Naval Architecture and Ocean Engineering*, 11(1):33–43, 2019.

[33] I. Gatin, V. Vukčević, H. Jasak, and I. Lalović. Manoeuvring simulations using the overset grid technology in foam-extend. In *32nd Symposium on Naval Hydrodynamics*, 2018.

[34] J. D. Van Manen and M. W. C. Oostervald. *Model Tests On Contra-Rotating Propellers*. NSMB Wageningen, Netherlands, 1969.

[35] R. Hecker and N. A. McDonald. *The Effect of Axial Spacing and Diameter on The Powering Performance of Counterrotating Propellers*. David W. Taylor Naval Ship R & D Center, Bethesda Md., 1960.

[36] M. L. Miller. *Experimental Determination of Unsteady Forces on Contrarotating Propellers in Uniform Flow*. David W. Taylor Naval Ship R & D Center, Bethesda Md., 1976.

[37] M. L. Miller. *Experimental Determination of Unsteady Forces on Contrarotating Propellers for Application to Torpedoes*. David W. Taylor Naval Ship R & D Center, Bethesda Md., 1981.

[38] T. Hoshino. *Experimental and Theoretical analysis of propeller shaft forces of contra-rotating propellers and correction with full scale data*. Propeller/Shafting'94 Symposium, Society of Naval Architects and Marine Engineers, Virginia Beach, 1994.

[39] S. Tsakonas, W.R. Jacobs, and P. Liao. Prediction of steady and unsteady loads and hydrodynamic forces on counterrotating propellers. *Journal of Ship Research*, 27:197–214, 09 1983.

[40] C. J. Yang et al. *Prediction of the steady performance of contra-rotating propellers by lifting surface theory*. Transactions of the West-Japan Society of Naval Architects No. 82, 1991.

[41] Z. Wang and Y. Xiong. Effect of time step size and turbulence model on the open water hydrodynamic performance prediction of contra-rotating propellers. *China Ocean Engineering*, 27, 2013.

[42] N. M. Nouri, S. Mohammadi, and M. Zarezadeh. Optimization of a marine contra-rotating propellers set. *Ocean Engineering*, 167:397–404, 2018.

[43] J. C. R. Hunt, A. A. Wray, and P. Moin. Eddies, streams, and convergence zones in turbulent flows. *Studying Turbulence Using Numerical Simulation Databases*, -1:193–208, 11 1988.

[44] G. HALLER. An objective definition of a vortex. *Journal of Fluid Mechanics*, 525:1–26, feb 2005.